Modelling Protein Aggregation Lubrication in Prosthetic Joints

Lee Nissim

Supervised by Dr. Robert Hewson and Dr. Connor Myant

A thesis submitted for the degree of

Doctor of Philosophy

Centre for Doctoral Training in

Fluid Dynamics Across Scales

Department of Aeronautics

Imperial College London

London SW7 2AZ

United Kingdom

March 2021





Modelling Protein Aggregation Lubrication in Prosthetic Joints

Lee Nissim

Abstract

Protein aggregation lubrication is the term given to the experimentally observed accumulation of protein matter at the inlet region of protein-rich, fluid-lubricated contacts. This lubrication mechanism causes larger than predicted fluid film thickness when compared to classical elasto-hydrodynamic lubrication theory and also exhibits the behaviour of decreasing film thickness with increasing sliding speed between the contact surfaces, again in contrast to theory. In the last decade, experiments have been carried out to capture the transient development of inlet aggregates in pin-on-flat tribometers. Understanding the lubrication mechanisms present in such lubricated contacts is vital for the continued development of prosthetic joint implant design and success.

In this study, a computational protein aggregation lubrication model has been created by using classical elasto-hydrodynamic lubrication theory coupled with a protein-dependent constitutive equation for fluid viscosity. The transport of protein matter in the thin film lubricated contact has been subject to an advection-diffusion model using geometry-based attenuation of flow rates, resulting in protein concentration aggregation at the inlet of the contact zone. The model parameters have been calibrated and the resulting transient protein aggregation lubrication simulation agrees well with previous experimentally observed transient film thickness behaviour when a cobalt–chromium–molybdenum alloy femoral head implant is tested in a pin-on-flat tribometer using diluted bovine calf serum as a synovial fluid analogue.

The model developed in this study requires the calibration of two separate parameters that relate to the shape of an approximate protein particle size distribution and to the nature of the exponential dependency of viscosity on protein concentration. Prior knowledge of the particle size distribution and rheological testing of experimental fluid would allow for these parameters to be fixed without calibration, however a parameter search method has been proposed for situations where these values are

unknown. The calibration overhead is significant even at the current level of model complexity and further refinement of computational efficiency is needed before it can be viably applied to a wide range of test cases.

Modelling prosthesis lubrication in this way provides a simple method to incorporate the effect of protein aggregation into simulations that can be used to provide greater insight into the conditions in the contact zone of joint prostheses including pressure, film height, and protein concentration which can in turn be used to derive friction coefficients and aid the study of surface wear.

Dedication

This thesis is dedicated to Sophia, Amelia-Rose and Poppy, whom we welcomed to the world during the course of this project and in memory of Grandad and Alex, whom we sadly lost.

Acknowledgements

I would like to express my sincere gratitude to my supervisors Dr. Robert Hewson and Dr. Connor Myant for their invaluable advice, expertise and patience. I would also like to thank Dr. Leiming Gao and Hamza Butt for their exceptional support during this study.

I extend my thanks to everyone involved in the Centre for Doctoral Training programme in Fluid Dynamics Across Scales and to the EPSRC, for the opportunity to pursue this Ph.D., especially to Clodagh Li, without whom the CDT would not have been the success it is.

For making these years unforgettable, I would like to thank Sarab Sethi, Nick Hooton, Paul Mannix, Rishabh Gvalani, Jan Rose and Rob Sullivan.

Finally, I would like to thank my incredible extended family for all of the encouragement and belief they have offered. In particular, I thank my parents for their immeasurable guidance, my Nan for her unwavering optimism and I thank my partner, Colette, for nothing short of everything.

Declaration

The work contained in this thesis is the author's own work unless otherwise stated.

Copyright

The copyright of this thesis rests with the author. Unless otherwise indicated, its contents are licensed under a Creative Commons Attribution-NonCommercial 4.0 International Licence (CC BY-NC).

Under this licence, you may copy and redistribute the material in any medium or format. You may also create and distribute modified versions of the work. This is on the condition that: you credit the author and do not use it, or any derivative works, for a commercial purpose.

When reusing or sharing this work, ensure you make the licence terms clear to others by naming the licence and linking to the licence text. Where a work has been adapted, you should indicate that the work has been changed and describe those changes.

Please seek permission from the copyright holder for uses of this work that are not included in this licence or permitted under UK Copyright Law.

Contents

1 Introduction **1**

1.1 Motivation . . . 2
1.2 Lubrication . . . 3
1.2.1 Elasto-hydrodynamic lubrication . . . 3
1.2.2 Boundary lubrication . . . 5
1.2.3 Mixed lubrication . . . 6
1.3 Bio-tribology . . . 9
1.3.1 Synovial fluid . . . 11
1.3.2 Modelling . . . 12
1.3.3 Experiments . . . 14
1.4 Protein aggregation lubrication . . . 17
1.5 Aims and objectives . . . 21

2 Elasto-hydrodynamic Lubrication **25**

2.1 Introduction . . . 26
2.2 Elasto-hydrodynamic lubrication theory . . . 27
2.2.1 The Reynolds equation . . . 27
2.2.2 Cavitation . . . 28
2.2.3 Elastic deformation . . . 29
2.2.4 Force balance . . . 30
2.3 Non-dimensionalisation . . . 31
2.4 Numerical methods . . . 34
2.4.1 Discretisation . . . 34
2.4.2 Solution method . . . 35
2.5 Validation . . . 37
2.6 Mesh dependency . . . 40
2.7 Reynolds equation super-solver . . . 42

2.7.1 Residuals . . . 42
2.7.2 Super-solver . . . 44
2.8 Fluid flow rates . . . 47
2.9 Summary . . . 51

3 Transport Modelling **53**
3.1 Introduction . . . 54
3.2 Advection-diffusion . . . 55
3.3 Non-dimensionalisation . . . 57
3.4 Discretisation . . . 58
3.4.1 Spatial discretisation . . . 58
3.4.2 Temporal discretisation . . . 61
3.5 Scheme testing . . . 63
3.5.1 Gaussian pulse . . . 63
3.5.2 High gradients . . . 66
3.6 Conservation terms . . . 69
3.6.1 Squeeze term . . . 69
3.7 Unknown value problem . . . 71
3.8 Summary . . . 72

4 Protein Aggregation and Rheology **73**
4.1 Introduction . . . 74
4.2 Protein movement attenuation . . . 75
4.3 Proposed scaling factor . . . 77
4.4 Scalar transport with attenuated flow rates . . . 80
4.5 Diffusion . . . 83
4.6 Constitutive equation . . . 85
4.7 Summary . . . 86

5 Transient Protein Aggregation Lubrication Model **87**
5.1 Introduction . . . 88
5.2 Parameter search . . . 89
5.2.1 Initial parameter search results . . . 90
5.2.2 Plateau height . . . 91
5.2.3 Curve similarity . . . 93
5.2.4 Péclet number . . . 96
5.2.5 Flow attenuation function . . . 96

5.3 Numerical accuracy and model refinement . . . 98
5.4 Results . . . 99
5.4.1 Concentration and viscosity . . . 99
5.4.2 Film height and inlet length . . . 102
5.4.3 Pressure . . . 105
5.5 Varying velocity conditions . . . 107

6 Conclusions **109**
6.1 Summary . . . 110
6.2 Recommendations for future work . . . 112

A Derivations **125**
A.1 Derivation of the Reynolds equation . . . 126

B Non-Dimensionalisation **131**
B.1 Hertzian method . . . 132
B.2 Dowson and Higginson method . . . 133
B.3 Moes method . . . 134
B.4 Relation between schemes . . . 135

C Numerical accuracy and model refinement details **137**
C.1 Time-step size . . . 138
C.2 Tolerance values . . . 139
C.3 Mesh density . . . 140

List of Figures

1.1 Reynolds pressure . . . 3
1.2 Ertel and Petrusevich geometries . . . 4
1.3 Boundary model . . . 6
1.4 Stribeck curve and lubricating regimes . . . 7
1.5 Synovial joint . . . 9
1.6 Prosthetic joint . . . 10
1.7 Equivalent geometry . . . 13
1.8 Experimental schematic . . . 15
1.9 Interferometry schematic . . . 16
1.10 Typical interferometry result . . . 16
1.11 Contact zone interferogram . . . 17
1.12 Experimental film thickness vs. velocity . . . 18
1.13 Inlet disruption results . . . 19
1.14 Inlet aggregate build up . . . 20
1.15 Contact geometry . . . 22
1.16 Solution schematic . . . 23

2.1 EHL schematic . . . 26
2.2 Lubrication geometry . . . 27
2.3 Effect of cavitation on pressure solution . . . 28
2.4 Deformation notation . . . 29
2.5 Point loading . . . 30
2.6 Hertzian dry contact . . . 31
2.7 Grid numbering . . . 34
2.8 Study of M values . . . 37
2.9 Mesh independence study for conventional convergence criteria . . . 40
2.10 Steady EHL Solution . . . 41

2.11 Solution residuals . . . 43
2.12 Super-solver solution comparison . . . 46
2.13 Flow velocity comparison . . . 48
2.14 Mass continuity . . . 50

3.1 Transport schematic . . . 54
3.2 Pulse simulations at Pe = 100 . . . 64
3.3 Pulse simulations at Pe = 1000 . . . 65
3.4 Downward step function . . . 67
3.5 Upward step function . . . 68
3.6 Squeeze term concentration . . . 70
3.7 Known variables of the transport problem . . . 71

4.1 Aggregation and rheology schematic . . . 74
4.2 Probability distribution functions . . . 79
4.3 Proposed scaling factor function . . . 79
4.4 Gradient levels . . . 80
4.5 Varying gradient parameter . . . 82
4.6 Varying Péclet number . . . 84

5.1 Transient PAL schematic . . . 88
5.2 Transport grid . . . 90
5.3 Parameter search film thickness results . . . 90
5.4 Plateau simulation selection . . . 91
5.5 Final film height response surface . . . 92
5.6 Sum of squared residuals . . . 93
5.7 Simulation length . . . 94
5.8 Sum of squared residual results . . . 95
5.9 Optimal parameter simulation . . . 95
5.10 Péclet number comparison . . . 96
5.11 Flow attenuation function review . . . 97
5.12 Concentration development results . . . 100
5.13 Regime map . . . 101
5.14 Height contour comparison with experiment . . . 102
5.15 Height profile comparison with experiment . . . 103
5.16 Inlet aggregate comparison with experiment . . . 104
5.17 Inlet length comparison with experiment . . . 105

5.18 Transient pressure results 106
5.19 Varying velocity 107

A.1 Thin film geometry 126

C.1 Time-step comparison 138
C.2 Height convergence comparison 139
C.3 RESS convergence comparison 139
C.4 Mesh density comparison 140
C.5 Onset of spurious oscillations 141
C.6 Third order scheme central film thickness comparison 142
C.7 Third order scheme concentration comparison 143
C.8 Small domain central film thickness comparison 144
C.9 Small domain concentration comparison 145

List of Tables

1.1 Protein concentration of synovial fluid and synovial fluid analogues . 11
1.2 Experimental parameters 22

2.1 Effect of pressure convergence tolerance 44
2.2 Effect of height convergence tolerance 45

5.1 Dimensionless parameter search range 89
5.2 Response surface coefficients 92

Nomenclature

Key and reccuring variables only are listed here. All variables (listed or otherwise) are defined on first use.

Dimensional

α	Pressure-viscosity coefficient $[Pa^{-1}]$
η	Fluid viscosity $[Pa.s]$
η_0	Reference viscosity $[Pa.s]$
η_{pf}	Protein-free fluid viscosity $[Pa.s]$
ρ	Fluid density $[kg.m^{-3}]$
ρ_0	Reference density $[kg.m^{-3}]$
a_h	Hertzian contact radius $[m]$
c	Potein concentration $[g.l^{-1}]$
c_0	Reference concentration $[g.l^{-1}]$
D	Diffusion constant $[m^2.s^{-1}]$
E	Young's modulus $[Pa]$
E'	Effective modulus $[Pa]$
h	Film thickness $[m]$
h_0	Contact surface separation $[m]$
h_h	Maximum Hertzian deformation $[m]$
p	Pressure $[Pa]$
p_h	Maximum Hertzian pressure $[Pa]$
q	Flow rate $[m^2.s^{-1}]$
R	Contact radius $[m]$
R'	Effective radius $[m]$
R_a	Average surface roughness $[m]$
R_{comp}	Composite surface roughness $[m]$
s	Inlet length $[m]$
t	Time $[s]$
u, v, w	Fluid velocities $[m.s^{-1}]$
u_e	Entrainment velocity $[m.s^{-1}]$
u_s	Sliding velocity $[m.s^{-1}]$
v	Deformation $[m]$
w	Load $[N]$
x	Location in sliding direction $[m]$
y	Location perpendicular to sliding $[m]$

Dimensionless

β	Concentration-viscosity coefficient
ϵ	Computation parameter $\epsilon = \tilde{\rho}H/\tilde{\eta}\lambda$
$\tilde{\eta}$	Dimensionless viscosity
$\hat{\eta}$	Dimensionless protein-free viscosity
λ	Chap. 1: Roughness parameter
λ	Chap. 2: Computation parameter $\lambda = 6u_s\eta_0R^2/a_h^3p_h$
ν	Poisson's ratio
$\tilde{\rho}$	Dimensionless density
τ	Dimensionless time $\tau = t/(a_h/u_s)$
a	Attenuation function gradient
C	Dimensionless concentration $C = c/c_0$
H	Dimensionless film thickness $H = h/h_h$
H_0	Dimensionless separation $H_0 = h_0/h_h$
N	Grid number
P	Dimensionless pressure $P = p/p_h$
Pe	Péclet number $\mathrm{Pe} = u_sa_h/D$
Q	Dimensionless flow rate $Q = q/(u_sh_h)$
T	Dimensionless time $T = t/(2a_h/u_s)$
X	Dimensionless location $X = x/a_h$
Y	Dimensionless location $Y = y/a_h$

Chapter 1

Introduction

1.1 Motivation

Joint replacements have been performed in the UK since the 1960s with the first hip implants. Knee and ankle replacement surgery began in the 1970s and the number of all procedures has increased rapidly ever since. Over 250,000 joint replacements were carried out in the tax year 2018/2019 in the UK, with knee and hip replacements accounting for the vast majority of these numbers [1]. As the number of procedures continues to increase, more and more people will be living with prosthetic joints.

Just over half of all hip replacements survive 25 years [2] and as a result, operations are usually offered to those aged between 60-80. Revision surgery (replacing/correcting the original prosthetic) can be undertaken but is challenging for surgeons due to increased complications, most notably bone loss [3]. This has driven research into increasing the lifespan of prosthetic joints in order to allow people to undergo joint replacement procedures at a younger age – who in the past would delay having a replacement and suffer from some level of discomfort – and also reduce the need for revision surgery.

A major issue affecting implant success is wear of the implant surfaces [4, 5]. Wear debris can build up within the joint and cause tissue inflammation and in turn loosening of the implant. Beyond this, there are many other adverse biological responses to wear debris. Metallic ions have been found in the lymphatic system, blood and urine of joint replacement patients and have been linked to lymphadenopathy and necrosis [6]. For these reasons, an analysis of the lubrication mechanisms that affect wear are central to research into extending the life of joint prostheses.

1.2 Lubrication

The study of fluid film lubrication is widely agreed to have begun with the experimental investigation by Beauchamp Tower in 1883 [7] of the friction coefficient of journal bearings bathed in different oils and run at varying speeds. This quantification of lubricated journal bearing operation provoked Osborne Reynolds to publish *'On the Theory of Lubrication and Its Application to Mr. Beauchamp Tower's Experiments, Including an Experimental Determination of the Viscosity of Olive Oil'* [8] in which was derived the equations that govern hydrodynamic lubrication, including the now eponymously named Reynolds equation. Hydrodynamic lubrication theory shows that pressure in the lubricating fluid can become large enough to support the bearing load when fluid is entrained into a converging gap. Figure 1.1 shows an excerpt from this paper in which the load bearing pressure hill can be seen.

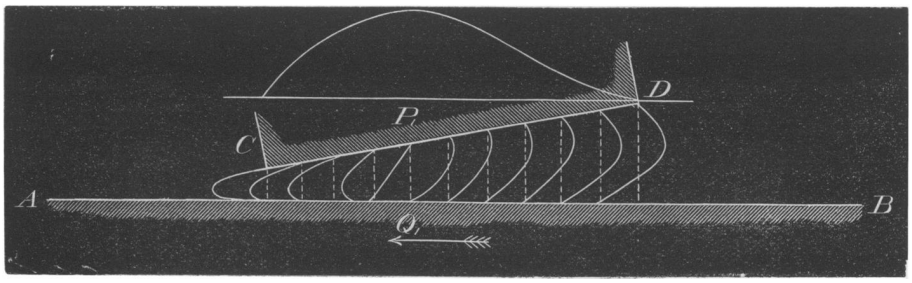


Figure 1.1: *Excerpt from Reynolds' paper outlining the theory of hydrodynamic lubrication whereby a converging wedge above a sliding plate produces a pressure hill that supports the bearing load [8].*

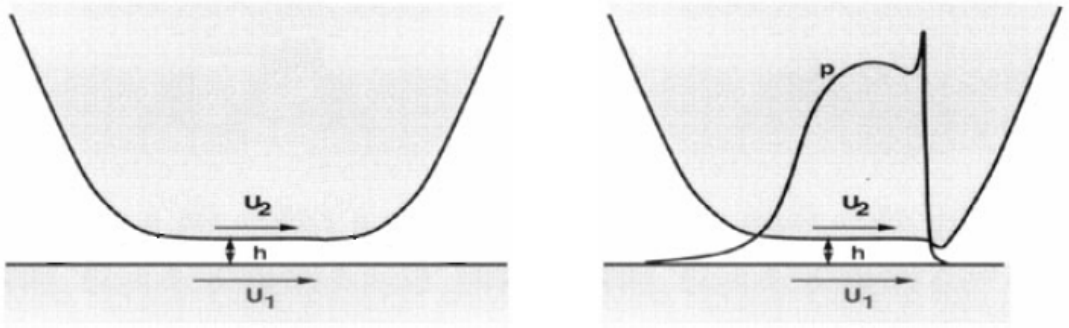
Reynolds offered analytic solutions to special cases of plane and journal bearings of infinite width and it was not until 1905 that A. G .M. Michell [9] offered an analytic solution to finite width plane bearings. This work lead to the invention of the tilting thrust bearing by Michell in 1905 [10] and independently by Kingsbury in 1910 [11]. The use of tilting thrust bearings enabled dramatic increase in load carrying capability and reduction in friction coefficient to the extent that the British Government saved roughly £0.5 Million on the cost of coal by replacing the bearings on naval vessels in 1918 [12].

1.2.1 Elasto-hydrodynamic lubrication

The success of hydrodynamic theory for analysing and designing lubricated contacts led Martin [13] and Gümbel [14] to investigate the lubrication mechanism at play between highly loaded gear teeth. Solving the Reynolds equation for this geometry

resulted in predicted fluid film thickness between the gear surfaces that was smaller than the surface roughness. It was observed that machining marks were still visible after long service times showing that a fluid film was indeed present and limiting the surface wear of highly loaded gears [12]. These conflicting findings led to the conclusion that hydrodynamic lubrication theory was not sufficient to explain the lubricating mechanism for such contacts.

This disparity between experiment and theory remained for decades until Ertel [15] and Grubin [16] published their works including the elastic deformation of the lubricated surfaces and a pressure-viscosity relationship in 1939 and 1949 respectively (although Ertel's groundbreaking contribution did not come to the attention of the wider community until much later, due to his defection from the USSR to West Germany and assumption of an alias [17]). In the absence of any advanced computing power these early studies were heavily simplified, focusing on the line contact problem with contacts of infinite width and using the analytically derived deformation solution of a dry contact from Hertzian theory [18] as the deformed surface shape rather than calculating the deformation of the surfaces from fluid pressure, as shown in Figure 1.2a. Despite these assumptions, the results were remarkably useful to approximate film thickness in heavily loaded or largely elastic lubrication regimes.



(a) (b)

Figure 1.2: *Schematics showing the geometry considered by (a) Ertel, implementing Hertzian deformation and (b) Petrusevich, implementing pressure deformation. The variables U_1 and U_2 denote the velocities of the surfaces, h, the film height and p, the pressure profile. Schematic (b) is an excerpt from Dowson and Ehret [19] and schematic (a) has been created from this same excerpt.*

Petrusevich developed these ideas in 1951 [20] and produced results for the line contact problem that satisfied the Reynolds equation, the local deformation due to

pressure and the same pressure-viscosity relation as Ertel and Grubin, derived by Barus [21]. Petrusevich's results gave the first great insight into the behaviour of what is now called *'Elasto-Hydrodynamic Lubrication'* (EHL). Most notably the dip in film height at the outlet of the contact zone and the coinciding pressure spike which had been predicted to exist, but not shown to, by Ertel, both shown in Figure 1.2b. This is often referred to as the *'Petrusevich spike'* [22].

Dowson and Higginson published a series of numerical solutions to the EHL problem over a wide range of velocities, loading conditions, and material properties throughout the late 1950s and early 1960s along with more advanced curve-fitted formulae for predicting film thickness [23–25], laying the basis for full coupled numerical solution methods to calculate EHL films thicknesses and pressure for a wide range of operating conditions, and also showing that the Petrusevich spike is only present under certain conditions. These contributions culminated in the landmark textbook on the subject titled, *'Elasto-Hydrodynamic Lubrication'* [26], widely considered the seminal text of the field.

The first point contact (sphere-on-plane) solutions were calculated by Ranger in 1975 [27] and Hamrock and Dowson in 1976 and 1977 [28–31] allowing the assumption of infinitely wide geometry to be dropped and EHL theory to be applied to an even wider collection of problems. More assumptions were revisited and thermal effects were also included for line contact problems by Cheng and Sternlicht [32], and Dowson and Whittaker [33], and later for point contact problems by Zhu and Wen [34]. The impact of starvation effects – the effects of an inadequate volume of lubricating fluid – were analysed by Weveden et al. [35] and Hamrock and Dowson [31] for line and point contacts respectively.

1.2.2 Boundary lubrication

In cases where the load is sufficiently high or the velocity sufficiently low, a fluid lubricant film does not separate the contact, and neither hydrodynamic theory nor EHL theory can predict the friction or wear of the surfaces. Hardy and Doubleday in 1922 [36] noticed that there was not only *'complete lubrication'* (i.e hydrodynamic) but also *'greasy lubication'* whereby a fluid film is not achieved but the lubricant still affects the coefficient of friction. This mechanism was coined *'Boundary Lubrication'* and it was proposed that perceived reduction in friction stems from the chemical nature of the lubricant and boundary solids, not from the viscous properties of the

fluid.

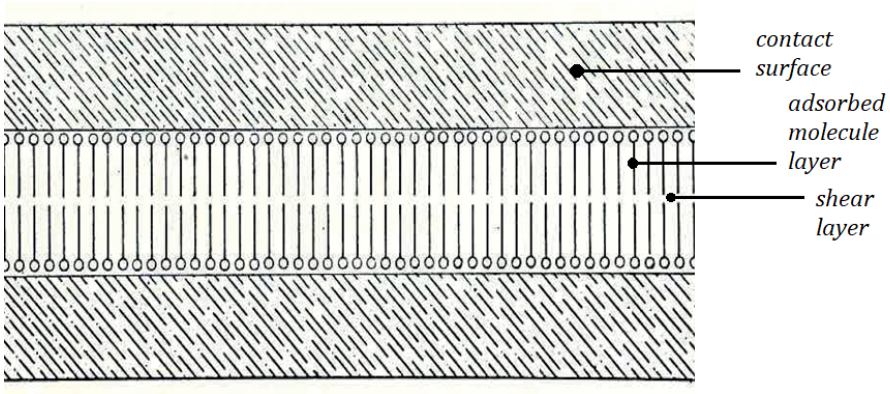


Figure 1.3: *Hardy's boundary lubrication model whereby an adsorbed film of polarised molecules forms on each surface, separating the contact and protecting the surfaces from excessive wear. Figure adapted from Dowson [12].*

Hardy and Doubleday's theory suggests that when a surface is coated with a lubricant film, the molecules close to the surface become ordered given their polarity and the attraction of the surface. There may exist one or several ordered layers of molecules depending on the specific nature of the surface and of the lubricant. The remaining molecules far from the surface remain randomly oriented and fluid. If the surfaces are close enough during operation the boundary layers of each will be adjacent and there will be no free moving fluid in-between. Because of the ordered nature of these layers, the friction experienced as they shear each other is less than than of two unlubricated dry surfaces. Figure 1.3 shows a schematic of a single boundary layer on each contact surface.

1.2.3 Mixed lubrication

The mechanisms that govern fluid film and boundary lubrication are very different, and most engineering bearings are designed to encourage fluid film lubrication as the ideal with the addition of additives to the lubricant that encouraged effective boundary lubrication in the case of severe operating conditions [12].

Experimental studies of journal bearings over a wide range of operating conditions by Stribeck [37] quantified the coefficient of friction in both fluid film and boundary lubrication and it was found that the coefficient in the boundary lubrication regime was unaffected by load, velocity and viscosity. Later work by Gümbel found that by plotting the coefficient of friction against the combined dimensionless parameter,

$\eta\omega/w$ – where η is the fluid bulk viscosity, ω, the rotational velocity of a journal bearing and w, the load – Stribeck's results could be plotted as a single curve that indicates the behaviour of each regime [38]. These became known as Stribeck curves and the parameter known varyingly as the Gümbel number or Stribeck number.

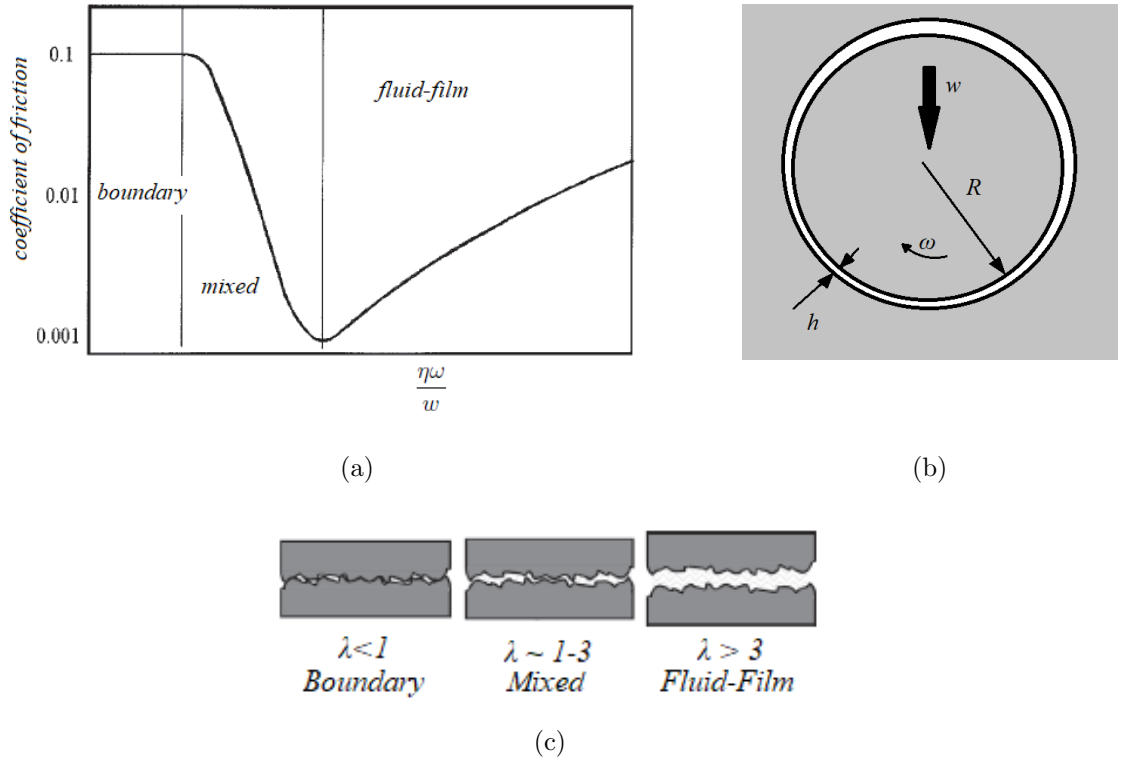


Figure 1.4: *(a) Idealised Stribeck curve indicating modes of lubrication. Figure adapted from Smith et al., [6]. (b) Simplified schematic of a journal bearing showing key parameters for the Stribeck diagram. (c) Visualisation of lubrication regimes in the contact zone for boundary, mixed and full fluid lubrication. Figure adapted from Myant and Cann, [39].*

The Stribeck curve in Figure 1.4a, shows the typical friction behaviour as a function of the Gümbel number, the variables of which can be seen in Figure 1.4b. Stribeck's experiments showed that in addition to pure boundary lubrication and pure fluid-film lubrication there was a sizeable transition regime whereby both mechanisms were important, now called *'Mixed Lubrication'*. When the Gümbel number is small, so too is the film thickness, h, and boundary lubrication dominates, resulting in relatively high friction and wear (albeit lower than that of dry contacts). As this parameter increases, the two surfaces become further separated, reducing contact between them and in turn reducing friction. At some Gümbel number this friction coefficient reaches a minimum and the increasing film thickness only adds to the overall friction in the system due to the fluid shear contribution. Figure 1.4c shows

a visualisation of each regime. A parameter, λ, can be used to define the separation of different lubrication modes, defining

$$\lambda = \frac{h_{min}}{R_{comp}}, \tag{1.2.1}$$

where h_{min} is the minimum film thickness and R_{comp} is the composite roughness of the two surfaces.

In 1978, Patir and Cheng [40, 41] showed that for fluid-lubricated EHL contacts where the film height becomes comparable to the roughness of the surfaces, film heights deviate from those predicted by Dowson and Higginson. By using an averaged Reynolds equation, it was shown that this stochastic approach predicted smaller film thicknesses where longitudinal roughness was present and increased film thickness in the presence of transverse roughness. With the development of more robust and stable multilevel methods by Lubrecht and Venner in the late 1980s and early 1990s [42–44] for solving the coupled equations of EHL, Venner was able to model deterministic roughness included in the height profile [43]. Further deterministic studies of roughness by Ren et. al. in 2009 [45] show that qualitatively, the effects are the same as predicted by the stochastic approach of Patir and Cheng, however the effect is smaller than previously thought.

1.3 Bio-tribology

Synovial joints have been known to be akin to lubricated bearings for over 250 years. The surgeon William Hunter wrote in 1743 [46] of the nature of human synovial joints,

> *"Where-ever the Motion of one Bone upon another is requisite, there we find an excellent Apparatus for rendering that Motion safe and free: We see, for instance the Extremity of one Bone moulded into an orbicular Cavity, to receive the Head of another, in order to afford it an extensive Play. Both are covered with a smooth elastic Crust, to prevent mutual Abrasion; connected with strong Ligaments, to prevent Dislocation; and inclosed in a Bag that contains a proper Fluid deposited there, for lubricating the Two contiguous Surfaces."*

Indeed on closer inspection of synovial joints, the similarity to conforming surface bearings such as the journal bearing in Figure 1.4b is evident.

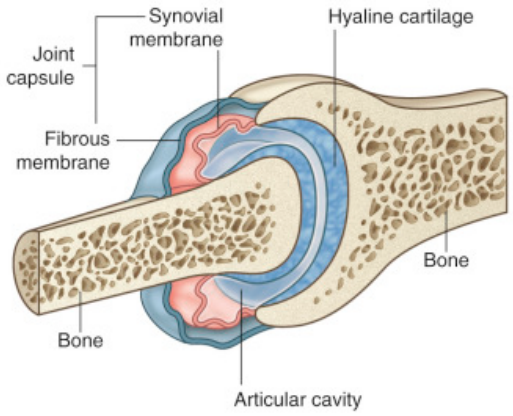


Figure 1.5: *Anatomy of a synovial joint, figure from Gray's Anatomy for Students [47]*

Figure 1.5 shows the anatomy of a synovial joint including those features discussed by Hunter. The synovial membrane is the *'bag'* that holds synovial fluid around the contact surfaces, which are the conforming *'orbicular cavity'* and *'head'* of two bones coated with an *'elastic crust'* of cartilage.

The presence of cartilage in the synovial joint allows for additional lubrication mechanisms including *'weeping lubrication'* proposed by McCutchen [48], whereby fluid contained within the porous cartilage becomes pressurised under load and the joint

acts like a self-pressurised hydrostatic bearing. A summary of the study of the modes of lubrication in natural joints has been published by Dowson [49].

When synovial joints are replaced, the cartilage and bone surfaces are removed. The joint is either replaced completely, known as Total Joint Arthroplasty (TJA), or the bones are resurfaced. In either case, the joint capsule is repaired such that the new joint can benefit from synovial fluid lubrication. Figure 1.6 shows the two replacement techniques for prosthetic hips.

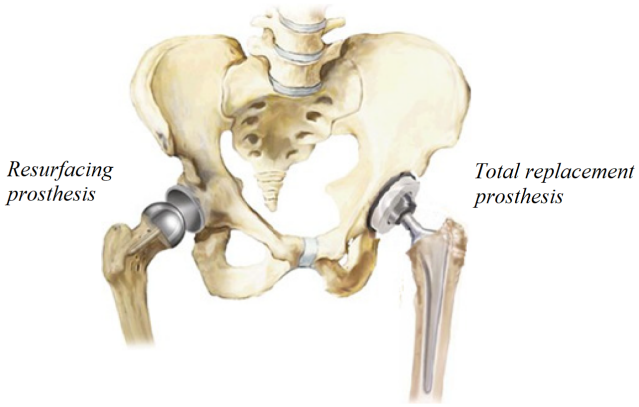


Figure 1.6: *Two techniques for replacing hip joints: resurfacing and total replacement, adapted from Mattei et al. [4]*

The majority of hip replacements use a wear resistant ultra-high-molecular-weight polyethylene (UHMWPE) cup and a cobalt–chromium–molybdenum alloy (CoCrMo) femoral head, know as a metal-on-polyethylene (MoP) implant [12]. Other materials such as ceramics have been used and implants are generally divided into *'hard-on-soft'*: MoP, ceramic-on-polyethylene (CoP), and *'hard-on-hard'*: metal-on-metal (MoM), ceramic-on-ceramic (CoC).

Hard-on-soft MoP implants were developed in the 1960s to combat the high friction of existing hard-on-hard MoM prostheses. Although successful, and still the most popular implant to this day, the relatively higher wear rates of UHMWPE have caused MoM implants to be revisited utilising more advanced manufacturing techniques. The introduction of ceramics was due to the ability to achieve a smoother surface finish, promoting fluid-film lubrication, and the harder surface material, leading to less wear. Studies into the benefits and drawbacks of each are ongoing [50, 51].

1.3.1 Synovial fluid

The lubricating fluid for healthy joints is synovial fluid, which is a complex water-based mixture of proteins, glycoproteins, hyaluronan, phospholipids and cholesterol and patient specific studies have shown that the concentration of macromolecules in synovial fluid can vary significantly [52, 53]. Once replacement surgery has been performed, the fluid that occupies the joint – periprosthetic synovial fluid – has differing concentrations of these components and is more akin to diseased synovial fluid as found in patients with arthritis. Periprosthetic synovial fluid has an increased concentration of proteins, higher pH level and decreased bulk viscosity when compared to that of healthy patients [39]. In experiments, diluted bovine calf serum is frequently used as a substitute for synovial fluid and has its own protein concentration profile. A summary of each fluid composition can be found in Table 1.1.

Lubricant	**Total protein [g/l]**	**Albumin [g/l]**	**Globulin [g/l]**
Healthy SF†	18 – 20	11.3–12.6	6.7–7.4
Osteoarthritic SF†	30.6 – 31.8	17.7–18.1	13.1–14.5
Rheumatoid SF†	34.6 – 45	20.1–20.3	14.5–24.8
Periprosthetic SF‡	24.6 – 54.2	20–39	4.6–15.4
Bovine calf serum†	72	28.8	43.2

Table 1.1: *Protein concentrations of bovine calf serum and synovial fluid (SF), data from* † *Wang et al. [53] and* ‡*Kitano et al. [52]*

Synovial fluid shows clear shear thinning behaviour in experiments [54]. While healthy, rheumatoid and osteoarthritic synovial fluid shows decreasing viscosity at shear rates of 10^3 s^{-1}, periprosthetic synovial fluid shows the beginnings of a high shear plateau at these magnitudes. Cases in which high shear rate is encountered are often treated as Newtonian [4, 39, 55]. Further studies by Castellanos et. al. [56] show that for bovine calf serum, most often used in experiments, the high shear rate plateau occurs at even lower shear rates of around 10^2 s^{-1}.

The concentration of protein content plays an important role in the rheological properties of synovial fluid. Studies by Coleman et. al. [57] show that at constant shear rate, the increased content of hyaluronan in a saline solution induces exponentially increasing viscosity. Castellanos et. al. [56] show rheometry results for varying concentrations of bovine serum albumin over a range of shear rates from 10^{-2} – 10^4 s^{-1} showing the effect of protein concentration on the full shear thinning behaviour of

the fluid. Results show the onset of a high-shear plateau at shear rates of 10^2 s^{-1} and also that the high-shear viscosity of bovine serum albumin increases exponentially with increasing protein concentration.

Protein matter also contributes to the visco-elastic nature of synovial fluid, whereby the reciprocating nature of human movement acts to entangle and disentangle the chains of protein molecules, storing energy much like an elastic solid. Studies by Balazs [58] show that the visco-elastic behaviour of synovial fluid under oscillating conditions changes over the lifetime of an individual.

Thixotropic and rheopectic effects have also been observed in synovial fluid due to the protein content. Thixotropy is defined as the tendency for viscosity to decrease over time at steady shear rate and rheopecticity as the tendency for viscosity to increase under the same conditions (sometimes called anti-thixotropy). Studies have shown thixotropic behaviour at high shear rates [59] but also rheopectic behaviour at relatively low shear rates as protein molecules aggregate. Oates showed that this rheopectic effect was prominent in solutions containing hyaluronan and milder when using bovine serum albumin [60].

Piezoviscosity is the effect of high pressure influencing the viscosity of lubricating fluid. The Barus equation introduced to the solution of elasto-hydrodynamic contact problems by Ertel is a common way to account for this effect in machine parts lubricated by hydrocarbon oils, where both elastic deformation and pressure-dependent viscosity must be considered, known as the *'piezoviscous-elastic'* regime. The Barus equation has the form

$$\eta(p) = \eta_0 e^{\alpha p} \tag{1.3.1}$$

where η is the viscosity, η_0 is the viscosity at ambient pressure, p the pressure, and α is a pressure-viscosity coefficient. For biological joints, peak pressures are of the order of tens of MPa [39] and it has been argued that this pressure is high enough to cause deformation without significantly affecting the synovial fluid viscosity or density [4, 55], i.e. the *'isoviscous-elastic'* regime.

1.3.2 Modelling

To model conforming contacts that occur in synovial joints, it is possible to map the geometry and material properties to an equivalent sphere-on-plane model. This is the same approach that is used to model the conforming surfaces of journal bearings and gear teeth.

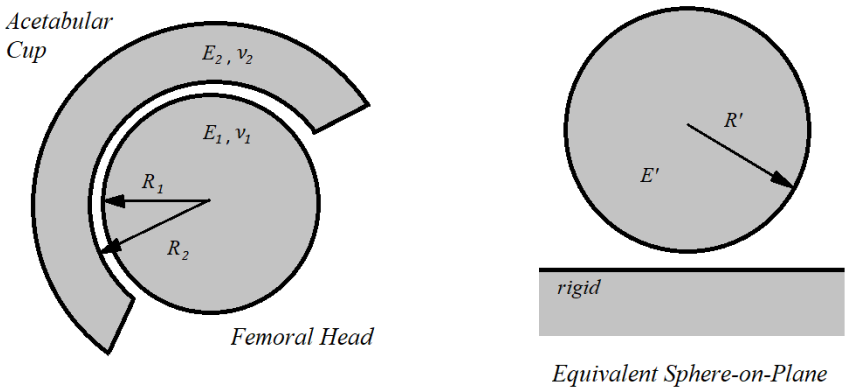


Figure 1.7: *Equivalent geometry and material mapping of conforming hip prosthesis surfaces to a sphere-on-plane model.*

The prosthetic geometry and material properties can be mapped onto the theoretical problem of a sphere of radius R' on a rigid plane with only one deforming surface of Young's modulus E' as shown for hip implants in Figure 1.7. The relations for mapping these parameters as described by Dowson and Higginson [26] are as follows,

$$\frac{1}{R'} = \frac{1}{R_1} - \frac{1}{R_2} \tag{1.3.2}$$

$$\frac{1}{E'} = \frac{1}{2}\left(\frac{1-{\nu_1}^2}{E_1} + \frac{1-{\nu_2}^2}{E_2}\right) \tag{1.3.3}$$

where E is the Young's modulus of each material and ν is the Poisson's ratio.

Numerical studies using this equivalent geometry were carried out in the late 1990s and early 2000s by Jin et al. [55, 61, 62] for line and point contact problems and it was concluded that unlike natural synovial joints, which likely operate in the boundary, mixed and fluid-film lubrication regimes, hip replacements are likely to operate in the mixed and fluid-film regimes only [55].

Some computational studies have solved the Reynolds and surface deformation equations using spherical coordinates to preserve the true prosthetic geometry. This is particularly useful when modelling walking gate cycles that have transient loads in multiple directions as implemented by Gao et al. [63, 64]. Studies by Wang et al. showed that results of the equivalent model were in agreement to results derived from a full spherical model of the acetabular cup [65] however Jin et al. [66] showed

that care should be taken when large deformations occur at the edges of the acetabular cup in which case the ball-on-plane model does not accurately predict the behaviour. More recently full geometry models of prosthetic knee joints have also been developed and elasto-hydrodynamic lubrication theory applied [67].

The non-Newtonian nature of synovial fluid has also been studied using Cross [64, 65] and Carreau models [68] for shear thinning fluids. Wang et al. [65] concluded that the inclusion of non-Newtonian shear thinning models resulted in only minor differences to the resulting geometry and pressure field due to the contact zone experiencing shear rates above the high rate plateau of synovial fluid. Gao et al. [64] and Mongkolwongrojn et al. [68] used reciprocating walking gate cycles on full spherical geometry and showed that shear thinning behaviour does have an effect on the thickness of the lubricating film during *'squeeze-film'* lubrication which occurs as the sliding velocity changes direction.

1.3.3 Experiments

With fluid conditions in implants being markedly different to those of hydrocarbon lubricated machine parts, experimental results are key to understanding the nature of the lubricating mechanisms that govern biological joints. Studies into the surface wear of prosthetics often use hip or knee simulators, whereby the prosthetic is loaded into a sealed and temperature-controlled bag containing bovine calf serum. The joint can then be subject to loading conditions similar to that of human walking, running or stair climbing. The wear of the surfaces can be analysed by weighing the implant after the simulation and by comparative microscopy of the simulator surfaces and retrieved implants.

Joint simulators of this type, however, give little indication of the underlying lubrication mechanism. For this, a sphere-on-plane – often called Pin-on-Flat (PoF) – tribometer can be used. This apparatus allows for the plane surface to be made of glass and cameras are able to view the contact zone as the experiment is taking place.

Figure 1.8 shows a typical tribometer setup with the femoral head of a prosthetic hip as used in studies by Myant, Cann et al. [69–74] and Nečas, Vrbka et al. [75–80]. A flat glass disc is spun by the drive system such that it slides over the *'pin'* – in this case the spherical femoral head implant. The entire experiment is situated in a lubricant bath such that the contact is never starved of fluid, although in other

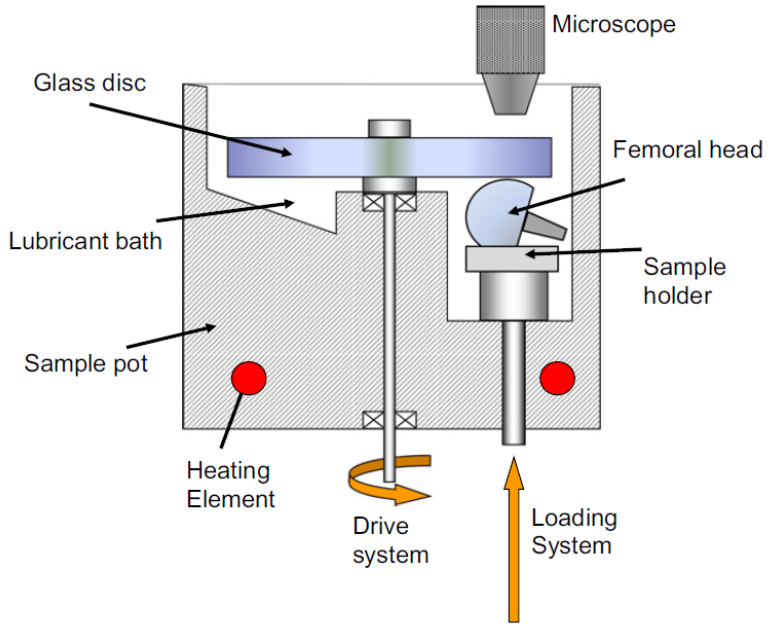


Figure 1.8: *Pin-on-Flat optical interferometric tribometer experiment setup schematic, from Myant and Cann [69].*

experiments, the lubricant is injected directly into the contact zone. More recently, conforming glass tribometers have been developed that allow the contact zone to be viewed during experiments with true ball-in-socket geometry of prosthetic hips [81].

In addition to viewing the contact zone via camera, glass tribometers allow the use of optical interferometry recordings. Interferometry allows the height profile of the contact zone to be measured by analysing the interference pattern of reflected light. If the sliding glass surface is coated with a semi-reflective layer of chromium, a beam of light shone upon the contact zone can be split, being partially reflected and partially allowed to travel through the contact zone. Once this light reflects off the second lubricating surface, the two reflections are measured by a spectrometer and the resulting interference pattern contains information of the distance between the two lubricating surfaces. Figure 1.9 shows a schematic representation of this process.

Interferometry techniques have been used to analyse EHL contacts since the 1960s but it wasn't until the early 1990s that ultra thin film methods allowed for analysing films in the order of nanometres [83]. A typical interferometer result for an isoviscous oil lubricated point contact can be seen in Figure 1.10. The height profile dip can be seen to form a horseshoe shape around the outlet of the contact zone, with the

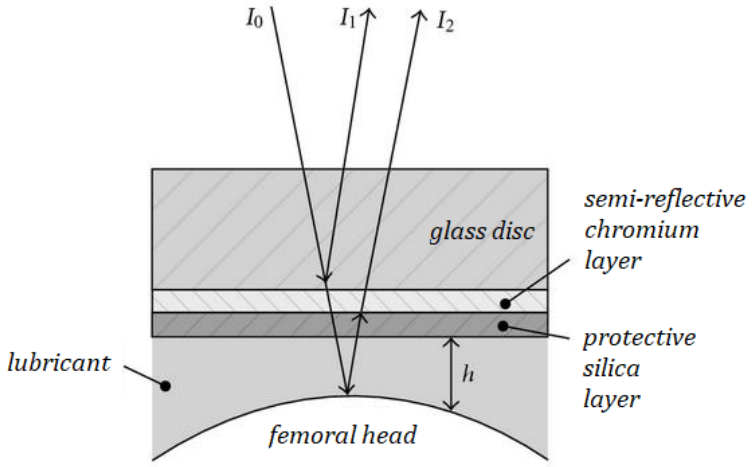


Figure 1.9: *Principles of optical interferometry, whereby emitted light, I_0, is semi-reflected by a chromium layer. The two reflections, I_1 and I_2 cause an interference pattern picked up by a spectrometer. Figure adapted from Ciulli et al. [82].*

minimum film thickness occurring in the side lobes.

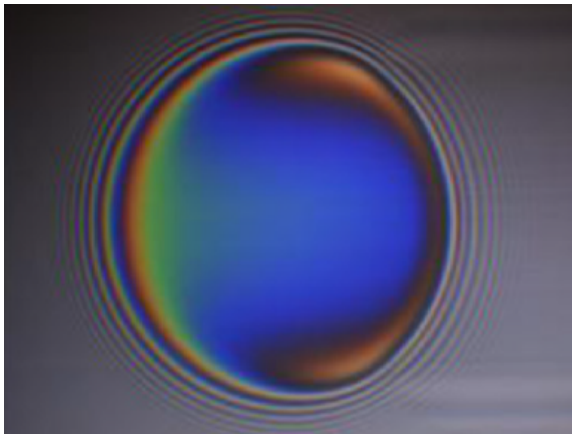


Figure 1.10: *Typical interferometry result for an oil lubricated elasto-hydrodynamic contact, sliding speed and fluid motion is from left to right. Figure from Marx et al. [84].*

1.4 Protein aggregation lubrication

When the experimental techniques described in § 1.3.3 are employed using diluted bovine calf serum as a synovial fluid analogue, interferometer images show a different lubrication mechanism is at work when compared to classical isoviscous elasto-hydrodynamic contacts.

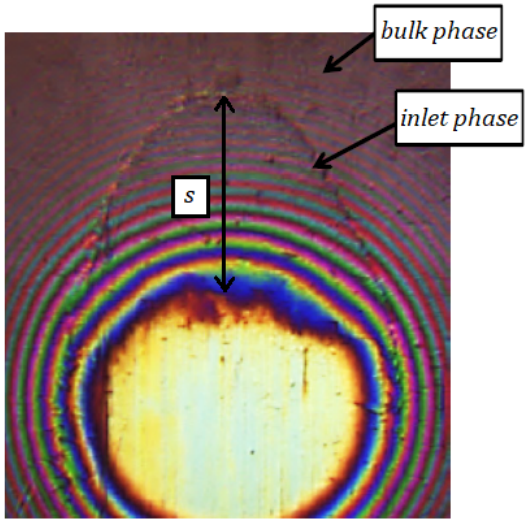
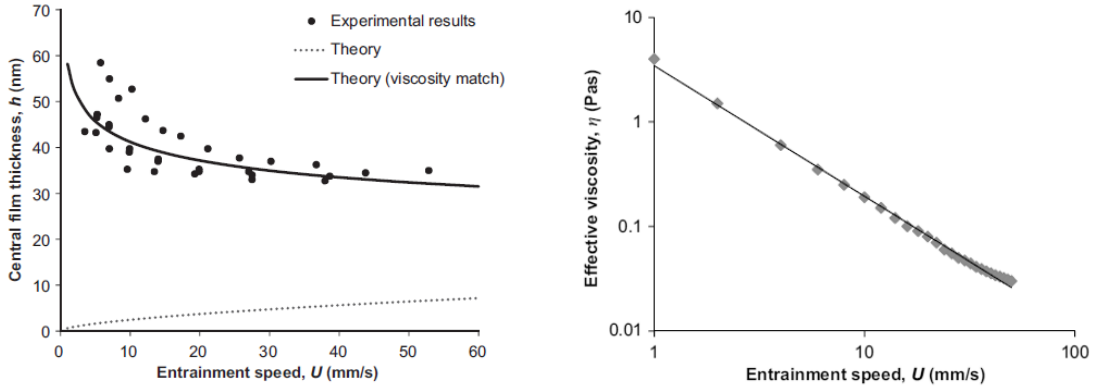


Figure 1.11: *Interferogram of contact zone during constant load and sliding speed experiment. Flow direction is from top to bottom and a clear distinction between bulk fluid and fluid in the inlet region can be seen. The length of the inlet region, s, is also shown. Figure adapted from Myant and Cann [69].*

Studies by Myant, Cann et al. [69–74], show that when using diluted bovine calf serum, which contains macromolecules of albumin and globulin, interferogram images show a distinct inlet region. Figure 1.11 shows an example of such an image as obtained by the experiments in 2012 [69]. The inlet region appears prominently on the interferogram image because the refraction properties of the fluid are noticeably altered by an increase in protein content in this area.

Another interesting phenomenon noted in the same study is that film thickness is much higher than would be predicted by classical EHL analysis and moreover shows counter-intuitive behaviour as the velocity of the sliding plate is varied. Figure 1.12 shows data from experiments by Myant and Cann [69], showing significant differences between experimental measurement of film thickness and those predicted by EHL theory.

The theoretical central film thickness calculations were taken from Hooke [85] for



(a) (b)

Figure 1.12: *Demonstration of differing behaviour in experiment and EHL theory. Figure (a) shows central film thicknesses as measured and predicted by theory (points and dotted line, respectively) with the addition of a modified theory (solid line) that artificially modifies viscosity to best fit experimental data. Figure (b) shows modified viscosity used for this solid line. Figures taken from Myant and Cann [69].*

isoviscous-elastic contacts in which the central film thickness formula is given as

$$h_{cen} = 4.18 \frac{(u_e \eta)^{0.6} R'^{0.67}}{w^{0.13} E'^{0.47}} \tag{1.4.1}$$

where R' and E' refer to the effective radius and Young's modulus of the contact, u_e, the entrainment speed (defined as the average speed of the two surfaces) and w, the applied load. The data does not only show significantly larger recorded film thicknesses but also shows that film thickness decreases as entraining velocity is increased. This is contrary to all conventional, isoviscous EHL predictions that show larger velocities induce larger fluid films. Also shown in Figure 1.12 is an adapted theoretical central film thickness line. This line has been created to best match the recorded data by artificially adjusting the fluid viscosity. Figure 1.12b shows these effective viscosities and suggests that the synovial fluid may be undergoing rheological changes during film formation. This study assumed the bulk viscosity of the diluted bovine calf serum to be 0.0025 Pa s [69] and thus these results suggest that locally in the contact zone viscosities could be up to 1000 times higher than expected.

This lubrication method has been named *'Protein Aggregation Lubrication'* (PAL) and as the name suggests is based on the hypothesis that proteins present in synovial

fluid collect in the inlet to the contact zone. This protein aggregate sits at the inlet and drastically alters the local viscosity allowing much thicker fluid films to form. This aggregate can break down and build back up again giving transient film thickness even under steady conditions and will break down more readily if the entrainment speed increases, causing the phenomenon of decreasing fluid film with increasing speed.

In subsequent experiments also by Myant and Cann in 2014 [71], the transient nature of the protein aggregate region was examined using an inlet disruption test. For this test, the sliding glass was held at a constant velocity and the inlet aggregate allowed to form. The protein matter was then stripped from the contact zone by a passing scratch on the glass surface.

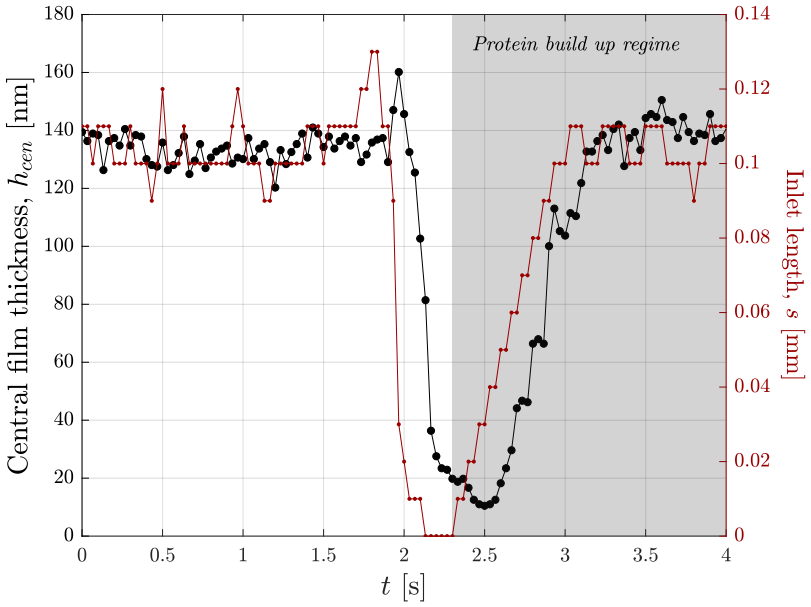


Figure 1.13: *Results of the inlet disruption test by Myant and Cann [71] showing transient behaviour of the central film thickness, h_{cen}, (black) and inlet aggregate length, s, (red) as a scratch removes the protein matter at the inlet to the contact zone. The subsequent regime whereby the inlet aggregate is reformed is highlighted.*

Figure 1.13 shows the central film thickness and inlet length (as defined in Figure 1.11) results of this inlet disruption test. The data shows a steady film thickness that is disturbed by the scratch placed on the glass sliding surface. This removes the protein aggregate from the contact zone and causes the central film thickness to drop to a level within the range predicted by Hooke's equation (7–28 nm). After the scratch has passed, the protein aggregate starts to rebuild and much higher film

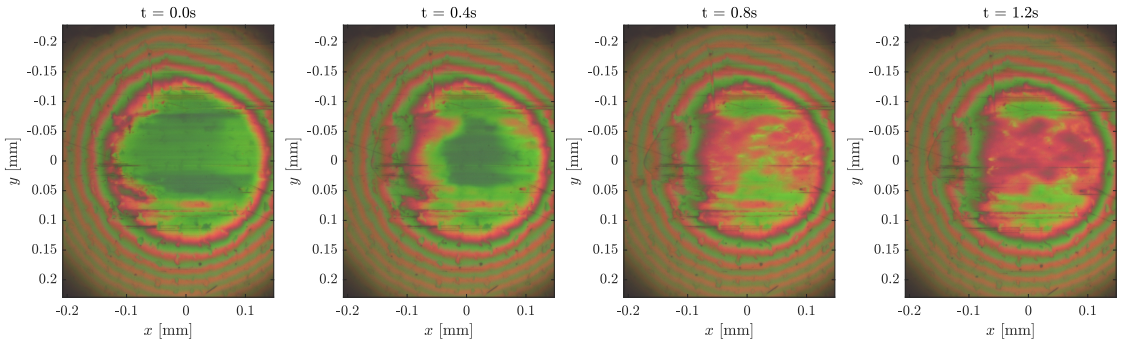


Figure 1.14: *Interferometer images of experiment by Myant and Cann [71] at select time-steps after the beginning of the protein build up regime.*

thickness is restored.

Figure 1.14 shows interferogram images from this experiment that demonstrate the inlet aggregate growth over time up to a steady inlet length. The time indicated is zero at the point that the protein begins to aggregate as indicated by the grey region of Figure 1.13.

1.5 Aims and objectives

The aim of this study is to create a computational model that captures the behaviour of protein aggregation lubrication, namely larger than predicted film thickness and the presence of protein aggregation at the inlet of the contact zone. Stokesian dynamics and force coupling methods [86, 87] have been used to successfully model the multiphase flows of particulates suspended in fluids. These methods are computationally intensive and require a great deal of knowledge of the initial state of the suspension. It has been shown that biological fluids including blood and synovial fluid [88] can be treated as a homogeneous fluid whose properties change based on a concentration of particulates that obey an advection-diffusion-reaction or advection-diffusion equation.

A model for simulating concentration-dependent shear thinning fluid has been proposed by Hron et. al. [89]. The concentration of protein content is simulated using an advection-diffusion model over a simple 2D wall-bounded domain. The fundamental phenomenon of protein aggregation lubrication however is that the thin film nature of lubricated contacts causes physical blockages to the free flowing protein macromolecules – an effect that has not yet been considered. No such model has been used to simulate this concentration-dependent behaviour in lubricated joint contacts, in which the geometry of the domain is also transient. This study couples elasto-hydrodynamic lubrication theory with a rheological model of concentration-dependent viscosity, based on the transport of protein matter in the contact zone of biological joints.

To do so, the inlet disruption experiment by Myant and Cann [71] – discussed in § 1.4 is used as the benchmark for the computational model developed in this study. The benefit of this experiment is that the sliding speed is constant and there are no transient start-up effects.

Figure 1.15 shows a schematic of the plane-on-sphere geometry of the experiment, including key parameters. Table 1.2 gives values for these key parameters, however the exact bulk viscosity of the lubricating fluid is unknown. The fluid used in the experiments was bovine calf serum diluted by water in a ratio of one part serum to three parts water by weight. This gives the resulting solution a protein content of 18 g/l. The surface roughness of CoCrMo femoral heads is cited frequently as $R_{a,fh} = 0.01$ μm [39, 53, 55] and the roughness of the silica-coated glass disc of this tribometer is given as $R_{a,gd} = 0.015$ μm [74], resulting in a combined equivalent

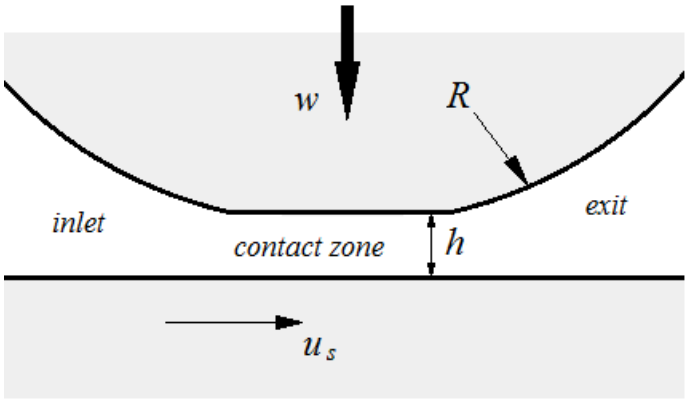


Figure 1.15: *Geometry of a sphere-on-plane lubrication problem in which the lower surface has a velocity, u_s, the sphere has an undeformed radius, R, and applied load, w. The film has height $h = h(x, y, t)$ in the z-direction.*

Variable	Symbol	Value
Sliding speed	u_s	20 mm/s
Effective modulus	E'	107 GPa
Effective Radius	$R = R'$	19 mm
Load	w	2 N
Bovine calf serum bulk viscosity	η	10 – 100 mPa.s

Table 1.2: *Experimental parameters for the inlet disruption study by Myant and Cann [71] on pure sliding contact of a stationary femoral head on 20 mm/s sliding glass.*

roughness of $R_{comp} = \sqrt{R_{a,fh}^2 + R_{a,gd}^2} = 0.018$ μm. For a brief period where the film height is at a minimum directly after the protein has been stripped, this likely means that the contact is operating in the mixed lubrication regime, however, as the inlet aggregate builds, the film height rapidly increases to bring the contact into the full fluid-film regime. For this reason, surface roughness effects have been ignored for this study. The values of Table 1.2 result in a mean Hertzian dry contact pressure of approximately 90 MPa and as such is considered low enough that piezoviscous effects are also ignored [55]. The model will therefore use isoviscous elasto-hydrodynamic theory to solve for the geometry and pressure of the contact zone.

For experiments involving film heights in the range of 100 nm and sliding velocities of the order of 10 mm.s^{-1}, shear rates are expected in the order of 10^5 s^{-1}, in excess of any expected high shear rate plateau of bovine calf serum of around 10^2 s^{-1} [56] – as discussed in § 1.3.1. Shear thinning effects are therefore assumed negligible in

this study.

In a study by Lu et al. [81], the unique behaviour of protein aggregation lubrication whereby larger sliding velocities result in decreased central film thickness was modelled by using an entrainment speed-dependent shear thinning Cross model that affects the viscosity of the fluid globally. The model however does not include any such modelling of the transport and accumulation of protein matter at the inlet of the contact zone or concentration-dependent rheological changes. This thesis aims instead to model the underlying geometry-dependent aggregation behaviour of experiments to explore whether such phenomena arise.

The remainder of the thesis outlines the individual blocks that form the full transient protein aggregation lubrication model, including the elasto-hydrodynamic theory and solver, the protein transport model and the geometry-dependent aggregation and rheology. Figure 1.16 shows a diagrammatic overview of how these blocks form the full transient solver and the chapters which discuss each individual component.

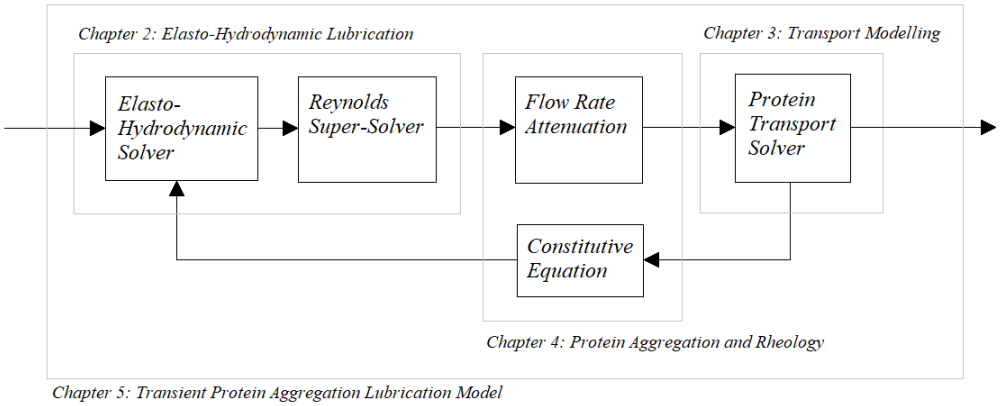


Figure 1.16: *Overview of transient PAL model and chapter organisation of this thesis.*

For each time-step during the PAL simulation, the contact geometry and pressure field are solved using the *'Elasto-Hydrodynamic Solver'* and the *'Reynolds Equation Super-Solver'*, the flow rate of the protein matter is then calculated from the flow rate of the lubricating fluid via a geometry-dependent attenuation function and the transport of the protein is simulated using an advection-diffusion equation. The resulting protein concentration field determines the local viscosity using a concentration-dependent constitutive equation and this viscosity field is used for the next time-step.

Chapter 2

Elasto-hydrodynamic Lubrication

2.1 Introduction

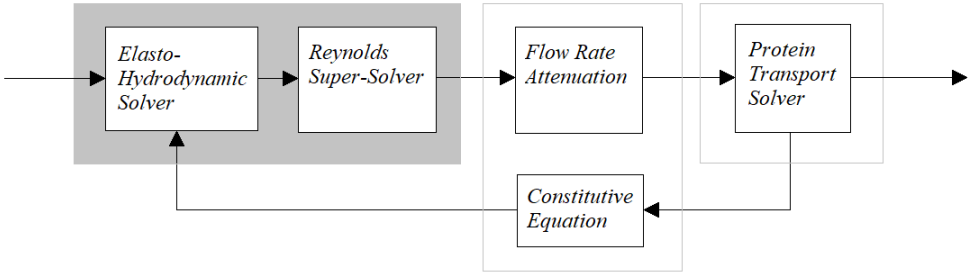


Figure 2.1: *Flow diagram showing overall PAL model schematic and the placement of the elasto-hydrodynamic solver and Reynolds equation super-solver block within it. The block receives the viscosity field from the constitutive equation and outputs film heights and volumetric flow rates.*

This chapter focusses on the implementation of elasto-hydrodynamic lubrication theory to the solution of thin film lubrication problems. This allows the calculation of lubricating film height and fluid pressure at each time-step of the overall protein aggregation lubrication model and from these results are derived the volumetric fluid flow rate. The location of this block within the larger PAL model is shown in Figure 2.1.

2.2 Elasto-hydrodynamic lubrication theory

The basis of most synovial joint modelling is classical EHL theory. The equations of which take into account hydrodynamic lubrication using the Reynolds and load balance equations, and elastic deformation of the contact surfaces but can also take into account the effects of high pressures in the fluid film. This typically includes pressure-dependent viscosity and density relationships, but for biological joints it has been argued that the pressure is high enough to cause deformation without significantly affecting the fluid viscosity or density, and it is also argued that synovial fluid can be treated as Newtonian without significant loss in accuracy [4, 55].

2.2.1 The Reynolds equation

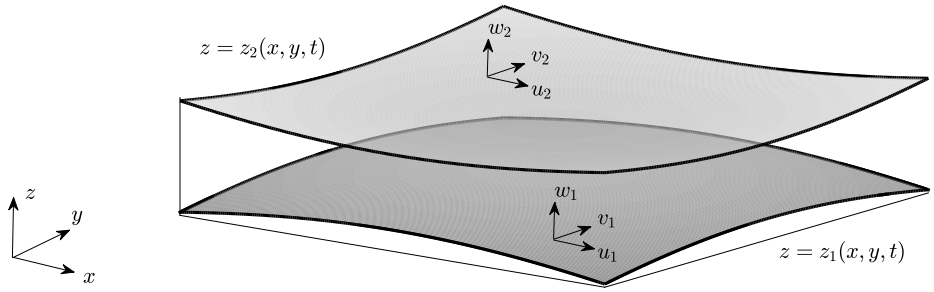


Figure 2.2: *Geometry of a typical lubrication film problem in which the two surfaces – labelled 1 and 2 – are shown with their respective velocities. The film has height* $h = h(x, y, t)$ *in the* z*-direction.*

The governing equation used for lubrication calculations is the Reynolds equation. This is an approximation of the full Navier-Stokes equations and is used in the case of thin lubricating films. It is derived by simple scaling arguments and a number of approximations which can be found in Appendix A.

$$\frac{\partial}{\partial x}\left(\frac{h^3}{\eta}\frac{\partial p}{\partial x}\right) + \frac{\partial}{\partial y}\left(\frac{h^3}{\eta}\frac{\partial p}{\partial y}\right) = 6\left\{u_s\frac{\partial h}{\partial x} + v_s\frac{\partial h}{\partial y}\right\} + 12\frac{\partial h}{\partial t} \tag{2.2.1}$$

Here, h is the film thickness (i.e. the separation of the surfaces in the z-direction), η is the viscosity of the fluid, and all other variables are shown in Figure 2.2, noting that $u_s = u_1 + u_2$ and $v_s = v_1 + v_2$. In this work, the surface velocities are limited to

a single direction and if the domain is chosen such that the x-axis aligns with this movement, v_s becomes zero and the Reynolds equation becomes:

$$\frac{\partial}{\partial x}\left(\frac{h^3}{\eta}\frac{\partial p}{\partial x}\right)+\frac{\partial}{\partial y}\left(\frac{h^3}{\eta}\frac{\partial p}{\partial y}\right)=6u_s\frac{\partial h}{\partial x}+12\frac{\partial h}{\partial t} \tag{2.2.2}$$

2.2.2 Cavitation

With pressure at the boundaries set to zero, i.e. solving for gauge pressure inside the contact, the Reynolds equation allows solutions with negative pressures. For an air bearing or other gas lubricated gap, this solution would provide an accurate picture of the physical behaviour, however with a liquid lubricant, pressures much below the vapour point cannot exist in the fluid film. Compared to the pressures that can form inside the contact, the vapour pressure of synovial fluid is close to zero and thus the vapour point can be treated as zero.

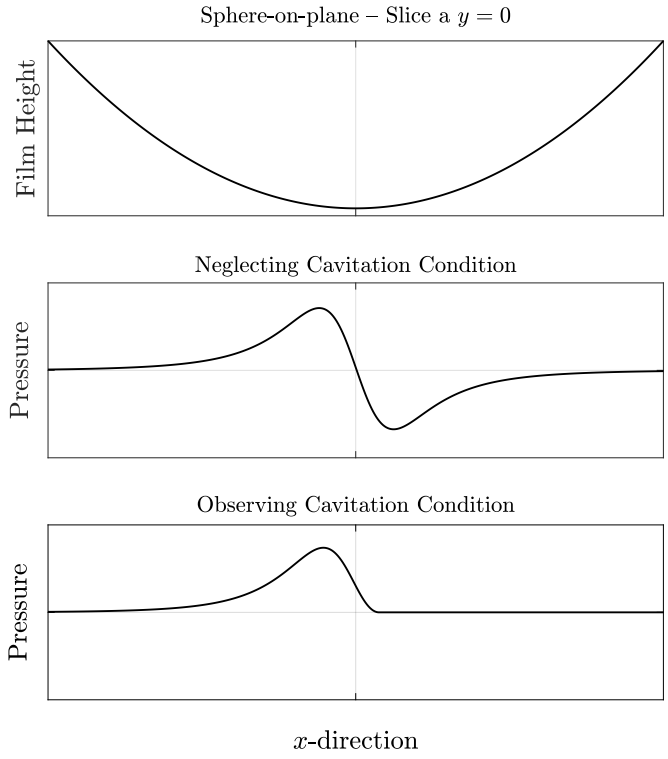


Figure 2.3: *Pressure profiles along the line $y = 0$ for a sphere on a plane. The upper pressure profile shows solution of the Reynolds equation without the cavitation condition limiting negative pressures – the full Sommerfeld solution. The lower pressure profile shows the resulting solution when cavitation is taken into consideration.*

Solving the Reynolds equation without considering the cavitation condition results in the full Sommerfeld solution, which can be seen in Fig. 2.3. This solution contains negative pressures and for a symmetric geometry, such as the sphere on a plane, results in an anti-symmetric pressure profile. Simply setting negative pressures to zero results in the half Sommerfeld solution however this solution violates continuity by allowing a discontinuity in pressure gradient. Instead, the pressure must smoothly reach zero. To implement this, the Reynolds equation must be solved iteratively, setting negative pressures to zero at each iteration. The resulting pressure profile can be seen in Fig. 2.3 and is seen to remain positive beyond the midpoint before reaching zero in a smooth manner. In the one-dimensional line contact problem this condition is simply stated as $dp/dx = p = 0$ at the cavitation point and is also called the Reynolds condition or the Swift-Stieber condition [90, 91].

2.2.3 Elastic deformation

When modelling the simplified ball-on-plane, the plane is modelled as rigid while the sphere deforms elastically with the effective Young's modulus, E'.

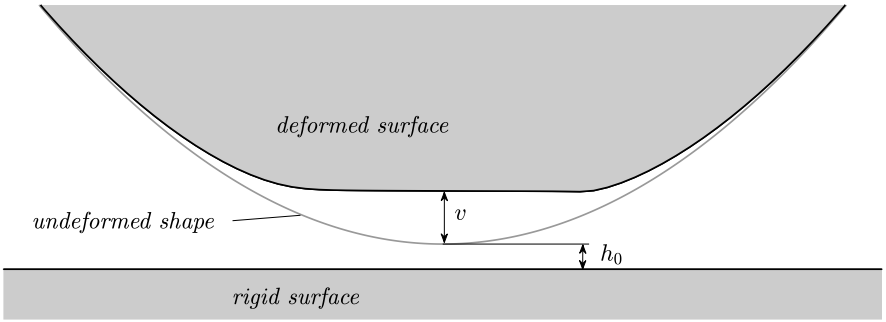


Figure 2.4: *Schematic illustrating notation for defining film height and shape. Here, h_0, denotes the separation at the centre-point of the undeformed surfaces and, v, denotes the deformation of the surface from this original shape.*

A parabola can be used to approximate the undeformed sphere, thus the film thickness for a $2D$ point contact is given by:

$$h(x, y) = h_0 + \frac{x^2}{2R} + \frac{y^2}{2R} + v(x, y). \tag{2.2.3}$$

To calculate the deformation, v, due to the entire pressure field it is possible to start with the solution for the deformation due to a point load.

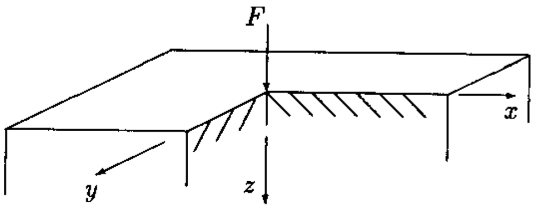


Figure 2.5: *Point loading of a half space with load F. Figure from Venner [43].*

Figure 2.5, shows a point load, F at the origin. For this, the solution to the deformation in the z-direction at any point is given by Love [92].

$$v(x,y) = \frac{1-\nu^2}{\pi E}\frac{F}{\sqrt{(x^2+y^2)}} \tag{2.2.4}$$

For deformation due to a pressure field, the summation of point load effects can be taken as such:

$$v(x,y) = \frac{1-\nu^2}{\pi E}\int_{-\infty}^{\infty}\int_{-\infty}^{\infty}\frac{p(x',y')}{\sqrt{(x-x')^2+(y-y')^2}}dx'dy' \tag{2.2.5}$$

where x' and y' are dummy integration variables.

Summing the deformation of both surfaces and using the relation of Eq. (1.3.3) to map to the model problem, the film thickness equation becomes

$$h = h_0 + \frac{x^2}{2R} + \frac{y^2}{2R} + \frac{2}{\pi E'}\int_{-\infty}^{\infty}\int_{-\infty}^{\infty}\frac{p(x',y')}{\sqrt{(x-x')^2+(y-y')^2}}dx'dy' \tag{2.2.6}$$

2.2.4 Force balance

In standard hydrodynamic lubrication, the Reynolds equation is used in conjunction with a force balance that ensures that the pressure in the fluid is enough to balance the load applied to the system. This is true also for elasto-hydrodynamics and involves a simple integration of the pressure as follows, where w is the applied load:

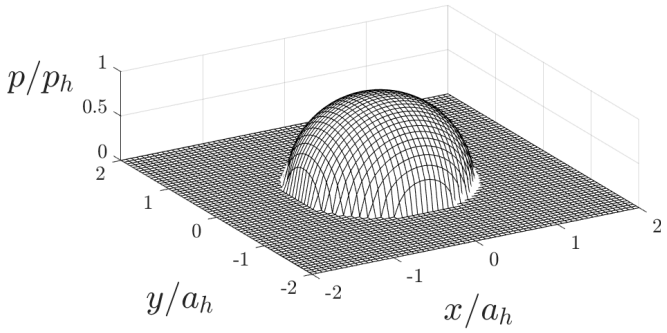
$$\int_{-\infty}^{\infty}\int_{-\infty}^{\infty} p(x,y)\,dx\,dy = w \tag{2.2.7}$$

2.3 Non-dimensionalisation

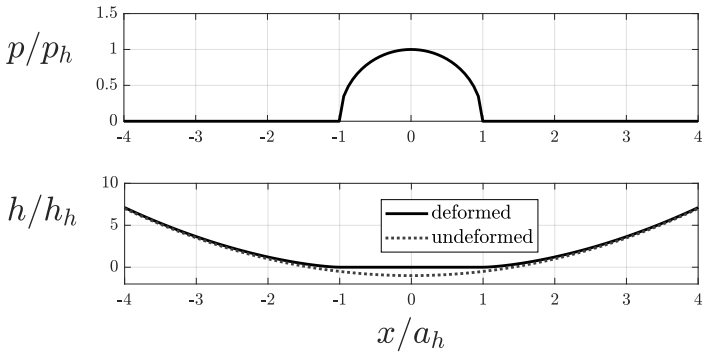
The non-dimensionalisation method used in this study stems from a comparison to the dry contact problem whereby two surfaces are forced together without a fluid lubricant and zero sliding speed. Hertz solved this problem in 1882 [18], and showed that the solution for the pressure profile is

$$p(x,y) = p_h\sqrt{1-(x/a_h)^2-(y/a_h)^2} \tag{2.3.1}$$

where a_h defines the limit of the contact region and p_h denotes the maximum pressure.



(a)



(b)

Figure 2.6: *Solution of the Hertzian dry contact problem for a sphere on a plane. Shown in (a) is the full pressure solution scaled with the maximum pressure on a spatial domain scaled by the radius of the contact area, a_h. Shown in (b) is the pressure profile over a slice at $y = 0$ and corresponding shape of the contact surfaces after deformation assuming a deformable sphere on a rigid half plane.*

From Fig. 2.6, it can be seen that the Hertzian solution for a sphere on a plane results in a circular contact region of radius, a_h. The radius of this region is calculated to

be

$$a_h = \left(\frac{3wR}{2E'}\right)^{1/3}. \tag{2.3.2}$$

It can also be seen that the pressure profile reaches a maximum at the origin, p_h. Another key result is the maximum deformation – also at this point, h_h. The maximum Hertzian pressure and deformation are

$$p_h = \frac{3w}{2\pi {a_h}^2} \qquad h_h = \frac{{a_h}^2}{R}. \tag{2.3.3}$$

Using these values as references for non-dimensionalisation, the following scaling can be applied to the elasto-hydrodynamic equations – Eq's. (2.2.2), (2.2.6), (2.2.7).

$$\begin{aligned} X &= x/a_h & Y &= y/a_h \\ P &= p/p_h & H &= h/h_h \\ \tilde{\rho} &= \rho/\rho_0 & \tilde{\eta} &= \eta/\eta_0 \\ & T = t/(2a_h/u_s) \end{aligned} \tag{2.3.4}$$

Here, the x- and y-directions are scaled with the contact radius, and the pressure and deformation are scaled with their respective maximum values from the Hertzian dry contact solution. The density and viscosity are scaled by a reference value also. Time has been scaled with a term containing a factor of two that is chosen to best suit the resulting equations. Substituting into the Reynolds equation and immediately dividing through by $\rho_0 h_h$ gives:

$$\frac{{h_h}^2 p_h}{{a_h}^2 \eta_0}\left(\frac{\partial}{\partial X}\left(\frac{\tilde{\rho}H^3}{\tilde{\eta}}\frac{\partial P}{\partial X}\right)+\frac{\partial}{\partial Y}\left(\frac{\tilde{\rho}H^3}{\tilde{\eta}}\frac{\partial P}{\partial Y}\right)\right) = \frac{6u_s}{a_h}\frac{\partial(\tilde{\rho}H)}{\partial X}+\frac{6u_s}{a_h}\frac{\partial(\tilde{\rho}H)}{\partial T} \tag{2.3.5}$$

Using this scaling and those of Eq. (2.3.4) the non-dimensional Reynolds equation can be written

$$\frac{\partial}{\partial X}\left(\frac{\tilde{\rho}H^3}{\tilde{\eta}}\frac{\partial P}{\partial X}\right)+\frac{\partial}{\partial Y}\left(\frac{\tilde{\rho}H^3}{\tilde{\eta}}\frac{\partial P}{\partial Y}\right)-\lambda\frac{\partial(\tilde{\rho}H)}{\partial X}-\lambda\frac{\partial(\tilde{\rho}H)}{\partial T}=0 \tag{2.3.6}$$

where the dimensionless parameter, λ is given by

$$\lambda = \frac{6u_s\eta_0 R^2}{{a_h}^3 p_h} \tag{2.3.7}$$

and the cavitation condition states that $P \geq 0$ within the domain and reaches 0 smoothly at the boundaries, where the downstream boundary is the cavitation line itself and is found during the solution.

The film thickness equation becomes

$$H(X,Y) = H_0 + \frac{X^2}{2} + \frac{Y^2}{2} + \frac{2}{\pi^2}\int_{-\infty}^{\infty}\int_{-\infty}^{\infty}\frac{P(X',Y')}{\sqrt{(X-X')^2+(Y-Y')^2}}dX'dY' \quad (2.3.8)$$

And finally, the force balance equation becomes

$$\int_{-\infty}^{\infty}\int_{-\infty}^{\infty}P(X,Y)dXdY - \frac{2\pi}{3} = 0 \quad (2.3.9)$$

2.4 Numerical methods

The domain of the modelled contact region is an equispaced square grid. The grid number, N, is defined such that the grid-points in each of the x- and y-directions are numbered 0 to N, resulting in a grid with $(N+1) \times (N+1)$ grid-points. The numbering convection can be seen in Figure 2.7.

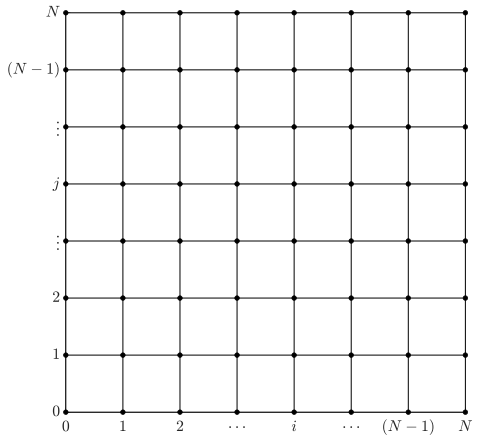


Figure 2.7: *Numbering convention for the equispaced grid of grid size N, such that an $(N+1) \times (N+1)$ grid is formed. Labels of subscript i indicate location in the x-direction and labels of subscript j indicate location in the y-direction.*

2.4.1 Discretisation

To solve Equations 2.3.6 – 2.3.9, finite difference methods have been utilised, similar to those used by Venner [43]. This involves a second order central discretisation for the first two terms of the Reynolds equation and a first order upwind scheme for the wedge term: $\partial(\tilde{\rho}H)/\partial X$. The squeeze term, $\partial(\tilde{\rho}H)/\partial T$, is calculated using the previous film height solution in the same first order manner as Gao [63] and is ignored for the first static solution. The resulting discretisation method for the Reynolds equation is:

$$\frac{\epsilon_{i-1/2,j}(P_{i,j} - P_{i-1,j}) + \epsilon_{i+1/2,j}(P_{i+1,j} - P_{i,j})}{\Delta X^2}$$

$$+ \frac{\epsilon_{i,j-1/2}(P_{i,j} - P_{i,j-1}) + \epsilon_{i,j+1/2}(P_{i,j+1} - P_{i,j}))}{\Delta Y^2}$$

$$= \frac{\rho_{i,j}H_{i,j} - \rho_{i-1,j}H_{i-1,j}}{\Delta X} + \frac{\rho_{i,j}H_{i,j} - \rho_{i,j}^{prev.}H_{i,j}^{prev.}}{\Delta T} \quad (2.4.1)$$

Here, $\epsilon = \tilde{\rho}H^3/\tilde{\eta}\lambda$ and values taken at the intermediate locations are defined in the manner:

$$\epsilon_{i+1/2,j} = \frac{1}{2}(\epsilon_{i,j} + \epsilon_{i+1,j}) \tag{2.4.2}$$

To discretise the film thickness equation, use is made of a deformation coefficient matrix, $\boldsymbol{K}$. This matrix stores the Hertzian deformation of every point in the domain subject to a unit point load at every other location in turn. These point load solutions can then be combined linearly to calculate the deformation for any pressure profile.

In general, the matrix $\boldsymbol{K}$ can be created using finite element analysis and loading a model of the required geometry at every grid location and recording the deformation at all others. For sphere on a plane geometry, it is possible to calculate $\boldsymbol{K}$ analytically – a derivation of which can be found in Venner [43] and is shown below.

$$\begin{aligned} K_{i,j,k,l} = |X_p| \ln\left(\frac{Y_p + \sqrt{X_p^2 + Y_p^2}}{Y_m + \sqrt{X_p^2 + Y_m^2}}\right) |Y_m| \ln\left(\frac{X_m + \sqrt{Y_m^2 + X_m^2}}{X_p + \sqrt{Y_m^2 + X_p^2}}\right) \\ |X_m| \ln\left(\frac{Y_m + \sqrt{X_m^2 + Y_m^2}}{Y_m + \sqrt{X_m^2 + Y_p^2}}\right) |Y_p| \ln\left(\frac{X_p + \sqrt{Y_p^2 + X_p^2}}{Y_m + \sqrt{Y_p^2 + X_m^2}}\right) \end{aligned} \tag{2.4.3}$$

where,

$$\begin{aligned} X_p = X_i - X_k + \Delta X/2 \quad , \quad X_m = X_i - X_k - \Delta X/2 \\ Y_p = Y_j - Y_l + \Delta Y/2 \quad , \quad Y_m = Y_j - Y_l - \Delta Y/2. \end{aligned} \tag{2.4.4}$$

Using this approach, the film thickness equation (Eq. 2.3.8) can be written as:

$$H_{i,j} = H_0 + \frac{X_{i,j}^2}{2} + \frac{Y_{i,j}^2}{2} + \frac{2}{\pi^2}\sum_{k=0}^{N}\sum_{l=0}^{N} K_{i,j,k,l}P_{k,l} \tag{2.4.5}$$

The force balance equation (Eq. 2.3.9)can be calculated using any number of discretised numerical integration techniques. For this study, the trapezium rule is utilised.

2.4.2 Solution method

Solution methods for the discretised equations have been refined multiple times over the last half century. Often, the Reynolds equation is solved using a point-wise Gauss-Seidel method whereby the new pressure solution is calculated at each grid-point in turn and applied immediately, or by point-wise Jacobi method whereby

the pressure solution is calculated for each point in turn but only applied after the full sweep of points is complete. The surface deformation is updated by matrix multiplication of Equation 2.4.5 and the force balance is checked. If the sum of pressures is too high, the value of H_0 is increased, globally separating the two surfaces (or moved together if the sum of pressures is too low).

These methods were shown to be unstable in some circumstances and a new standard for solving these equations was introduced by Lubrecht and Venner [44], whereby Gauss-Seidel line, and distributive Jacobi relaxation are utilised to solve the Reynolds equation. Intead of visiting each grid-point in turn, each line in the x-direction (i.e. each line of constant j) is solved simultaneously. The method used at each point along the line (i.e each i location) depends on the value of the parameter ϵ/h^2. For values of $\epsilon/h^2 \geqslant 0.3$, Gauss-Seidel relaxation is used and the point is updated with a new solution. For values of $\epsilon/h^2 < 0.3$, distributive Jacobi relaxation is used whereby the point and its immediate neighbours (including neighbouring lines) are updated. This method provides greater stability for the solution of the EHL problem. Venner and Lubrecht also introduced *'Multi-Level methods'* that use multiple grids of decreasing density to increase stability and solution speed further; however for the isoviscous and moderately loaded contacts encountered in this study, the solutions are solvable on a single grid.

An elasto-hydrodynamic lubrication solver incorporating the Gauss-Seidel line, and distributive Jacobi relaxation methods, was created in MATLAB by Butt [67], and has been adapted by the author to allow for locally varying viscosity throughout the domain.

2.5 Validation

To compare the steady EHL solutions to those of other studies, it is useful to introduce an alternative non-dimensionalisation introduced by Moes [93]. The important values for comparison are the load parameter, also known as the Moes number

$$M = \frac{w}{E'R^2}\left(\frac{E'R}{\eta_0 u_s}\right)^{3/4} \tag{2.5.1}$$

and the dimensionless film height

$$H^M = \frac{h}{R}\left(\frac{E'R}{\eta_0 u_s}\right)^{1/2} \tag{2.5.2}$$

where the superscript M is used to differentiate from the Hertzian dimensionless film height used thus far, $H = h/h_h$. A full discussion of popular non-dimensionalisation schemes and their relations is covered in Appendix B.

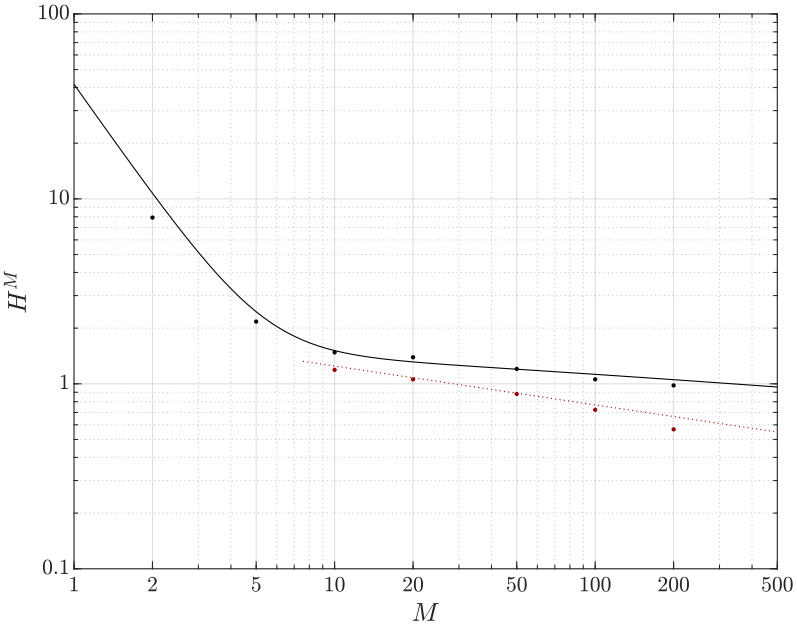


Figure 2.8: *Comparison of simulation results with best fit lines of other studies. The black points show the central film thickness (at peak pressure) of simulations compared to the solid line that was found to best describe simulation results by Venner and Lubrecht using Equation 2.5.6 [44]. The red points show the minimum film height for simulations in the isoviscous-elastic regime, $M \geqslant 10$, where the dotted line shows a best fit line proposed by Hamrock and Dowson using Equation 2.5.3 [94]*

Figure 2.8 shows the central film thickness results of steady simulations at various load parameter values with a grid number of $N = 2^7$. The central film thickness

can be defined as either $H_{X=Y=0}$ at the centre of the contact or as $H_{\partial P/\partial X=\partial P/\partial Y=0}$ at the peak pressure point. For simulations in the elastic regime, these locations are the same, however for simulations in the rigid regime, where the load is small and the surfaces do not deform, the pressure peak is located upstream of the centre point. For 1D line contact problems, simulations can be compared to analytical solutions; however the 2D circular contact problem is too complex and available reference formulae are best fit lines from other numerical studies.

One such study is that of Hamrock and Dowson [94] whereby a best fit line for the minimum film thickness in the isoviscous-elastic regime can be expressed in Moes non-dimensionalisation parameters [95] by the equation

$$H_{min}^{M} = 2.035 M^{-0.21} \tag{2.5.3}$$

which is shown in Figure 2.8 as a red dotted line. For comparing central film thickness, the asymptotic cases of the isoviscous-rigid and isoviscous-elastic contacts have been modelled respectively as

$$H_{ir}^{M} = 41.4 M^{-2} \tag{2.5.4}$$

$$H_{ie}^{M} = 1.96 M^{-1/9} \tag{2.5.5}$$

as expressed by Venner and Lubrecht [44]. These asymptotic cases can be combined along with the asymptotic cases for piezoviscous-rigid and piezoviscous-elastic regimes to predict the entire range of of possible parameter values [44, 93]. As the PAL model will not include piezoviscosity, this equation can be simplified to the following form

$$H_{c}^{M} = \left\{ (H_{ir}^{M})^{3/2} + \left[(H_{ie}^{M})^{-4} + 0.01 \right]^{-3/8} \right\}^{2/3} \tag{2.5.6}$$

which is plotted in Figure 2.8 as a solid black line. There is good agreement for both central and minimum film thickness in the elastic regime, but a slight under prediction of film thickness in the rigid regime. This could be due to numerical starvation, the phenomenon of the upstream pressure boundary conditions influencing the solution, resulting in smaller pressure than would otherwise develop. To combat this, as large a domain as possible is used for those simulations with load parameters below $M = 10$ however this regime is not of great importance for this study.

The experimental result that is used to verify the PAL model, as described in § 1.4, starts with a central film thickness of $h_c \approx 20$ nm. Using the isoviscous-elastic

formula of Equation 2.5.5 and the definition of the dimensionless parameters M and H^M from Equations 2.5.1 and 2.5.2 it is possible to deduce a value of the fluid viscosity that will result in a similar starting film thickness using the equation below.

$$\eta_0 = \left(\frac{E'R}{u_s}\right)\left(\frac{w}{E'R^2}\right)^{4/21}\left(\frac{h}{1.96R}\right)^{12/7} \tag{2.5.7}$$

Setting $h = 20 \times 10^{-9}$ m and the other values to match those of experiment in Table 1.2 gives an estimate value of $\eta_0 = 0.0743$ Pa.s. Parametric testing shows that a value for the initial viscosity, $\eta_0 = 0.075$ Pa.s leads to a simulation that matches the experimental initial central film thickness. This equates to a load parameter value of $M = 65$, comfortably in the isoviscous-elastic regime.

2.6 Mesh dependency

There are several different values that can be used to infer convergence and conclude the simulation at each time-step, namely the force balance, pressure error, height error and residual.

Conventionally, the solver is run until the force balance and iterative change in pressure are adequately small as defined by

$$\frac{\sum_{i,j=0}^{N} P_{i,j}^{n} - P_{i,j}^{n-1}}{\sum_{i,j=0}^{N} P_{i,j}^{n}} < \epsilon_{tol} \tag{2.6.1}$$

$$\frac{\sum_{i,j=0}^{N} P_{i,j}^{n} \Delta X \Delta Y - \frac{2\pi}{3}}{2\pi/3} < \epsilon_{tol} \tag{2.6.2}$$

Here, n denotes the iteration step and the solution scheme is terminated when the changes in pressure solution at each iteration become smaller than a prescribed tolerance as does the force imbalance between the summed pressure and load. The tolerance, ϵ_{tol}, is commonly in the region of 10^{-4} [63, 96].

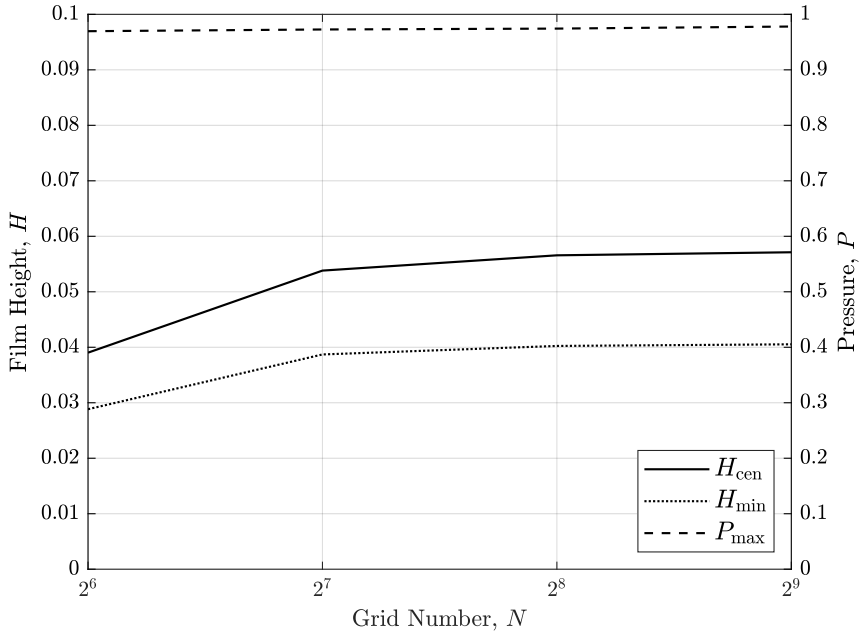
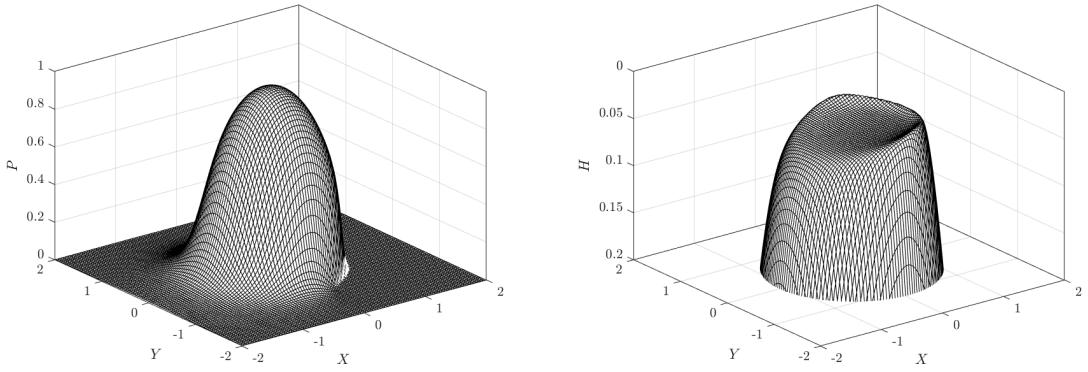


Figure 2.9: *Mesh independence study showing key values of interest, namely central film height, H_{cen}, minimum film height, H_{min}, and maximum pressure, P_{max}, over a range of $(N+1) \times (N+1)$ grids over the domain $-5 \leqslant X \leqslant 5, -5 \leqslant Y \leqslant 5$.*

Plotting the central film height, H_{cen}, minimum film height, H_{min}, and maximum pressure, P_{max}, for simulations using the convergence criteria in Equations 2.6.1 and

2.6.2 over a domain $-5 \leqslant X \leqslant 5, -5 \leqslant Y \leqslant 5$ shows that a grid of 257×257 is dense enough for mesh independence. The difference in these values of interest between grids of $N = 2^8$ and 2^9 are all less than 1%.



(a) (b)

Figure 2.10: *Steady (a) pressure and (b) film height solution of the elasto-hydrodynamic equations for the initial load parameter,* $M = 65$*, simulated on a* 257×257 *grid over the domain* $-5 \leqslant X \leqslant 5, -5 \leqslant Y \leqslant 5$.

Figure 2.10 shows the pressure and film height solutions of the steady solution at load parameter $M = 65$, which gives the initial dimensional film height of 20 nm. This solution shows the characteristic horseshoe-shaped lobe present in isoviscous-elastic lubricated contacts.

2.7 Reynolds equation super-solver

Running the EHL solver until the convergence criteria of Equations 2.6.1 and 2.6.2 gives acceptably converged film heights and pressure profiles and agree well with other studies. The use of these criteria, however, offers no explicit requirements over the residual of the Reynolds equation itself. The Reynolds equation is simply a mass conservation equation and as the pressure and film height results of the EHL step will be used to calculate fluid flow rates, it is important that mass is indeed conserved.

2.7.1 Residuals

The residual of the Reynolds equation, r_R, can be calculated by substituting the solution values of P and H into the same discretisation scheme as that of Equation 2.4.1 such that

$$(r_R)_{i,j} = \frac{\epsilon_{i-1/2,j}(P_{i1,j} - P_{i-1,j}) + \epsilon_{i+1/2,j}(P_{i+1,j} - P_{i,j})}{\Delta X^2} + \frac{\epsilon_{i,j-1/2}(P_{i,j} - P_{i,j-1}) + \epsilon_{i,j+1/2}(P_{i,j+1} - P_{i,j}))}{\Delta Y^2} - \frac{\rho_{i,j}H_{i,j} - \rho_{i-1,j}H_{i-1,j}}{\Delta X} - \frac{\rho_{i,j}H_{i,j} - \rho_{i,j}^{prev.}H_{i,j}^{prev.}}{\Delta T} \quad (2.7.1)$$

The maximum absolute value of the Reynolds equation residual for the steady solution with $\epsilon_{\text{tol}} = 10^{-4}$ is found to be 3.19, which is large enough to result in significant depletion of mass when results are used for transport equations. If the EHL solver is run to much stricter convergence criteria, the residual can be reduced but the computation time increases.

Figure 2.11 shows the residual of the Reynolds equation across the solution domain for three levels of convergence tolerance, ϵ_{tol}. Large residuals at the more relaxed tolerances are near the upstream boundaries where the pressure is set to zero. Pressure in this upstream region is small and the second derivative of these values is sensitive to minute changes. For this reason it takes much longer for the residuals to reduce adequately.

Table 2.1 shows the effect of ever stricter convergence criteria on computation times and select key values. Despite the continued reduction of the maximum absolute

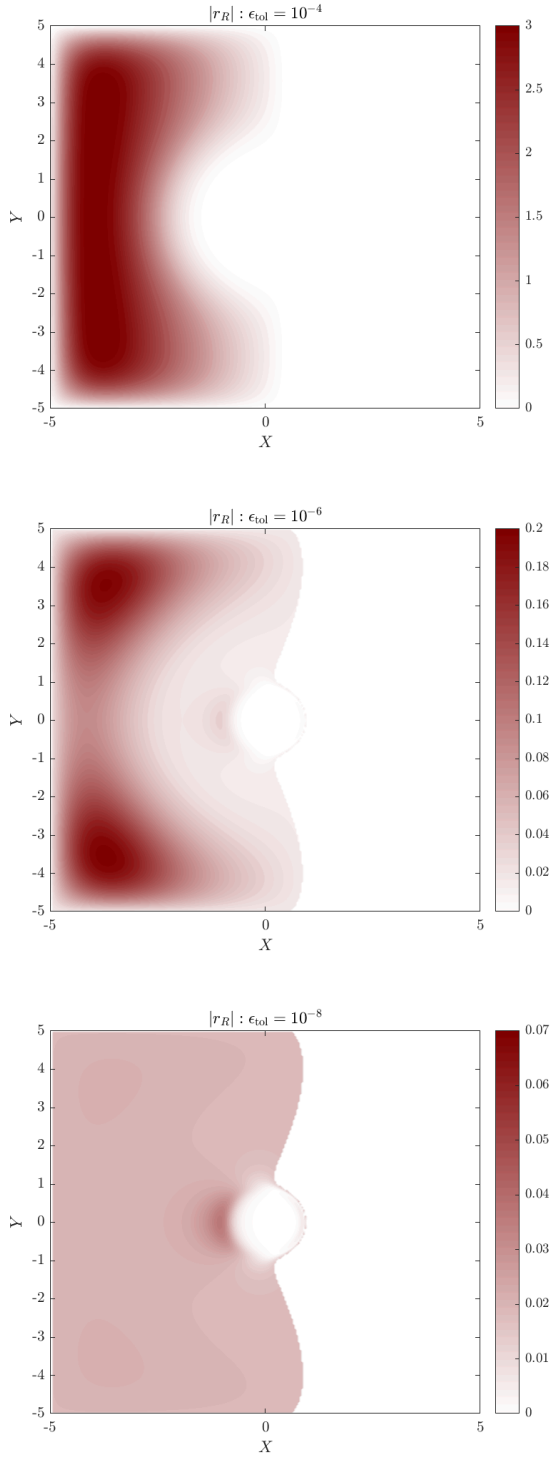


Figure 2.11: *Absolute value of the Reynolds residual, r_R of the initial steady EHL solution at varying convergence levels of the criteria in Equation 2.6.1 and 2.6.2. Residual values downstream of the cavitation line are set to zero as the Reynolds equation is not valid in this region. Particular attention should be paid to the contour scales on the right hand side.*

		ϵ_{tol}		
		10^{-4}	10^{-6}	10^{-8}
N	2^6	5	9	18
	2^7	28	145	303
	2^8	215	2275	4790

(a) *Computation time* $[s]$

		ϵ_{tol}		
		10^{-4}	10^{-6}	10^{-8}
N	2^6	0.6663	0.1453	0.1453
	2^7	2.2119	0.0935	0.0740
	2^8	3.1875	0.2038	0.0667

(b) *Maximum residual,* $|r_R|_{\max}$

		ϵ_{tol}		
		10^{-4}	10^{-6}	10^{-8}
N	2^6	0.0390	0.0385	0.0385
	2^7	0.0538	0.0538	0.0538
	2^8	0.0566	0.0566	0.0566

(c) *Central film height,* H_{cen}

		ϵ_{tol}		
		10^{-4}	10^{-6}	10^{-8}
N	2^6	0.9696	0.9692	0.9692
	2^7	0.9727	0.9715	0.9715
	2^8	0.9743	0.9711	0.9710

(d) *Maximum pressure,* $P_{\max}$

Table 2.1: *The effect of decreasing convergence tolerance on (a) computational time – to the nearest second, run on an Intel(R) Core(TM) i5-10210U CPU – and on key values of interest, namely (b) the maximum absolute residual of the Reynolds equation, (c) dimensionless central film height at* $x = y = 0$ *and (d) dimensionless maximum pressure.*

residual of the Reynolds equation as ϵ_{tol} decreases, it can be seen that the central film height and maximum pressure are already well converged at higher tolerance values, both changing less than 0.1% between $\epsilon_{\text{tol}} = 10^{-4}$ and 10^{-8}. Moreover, as the requirement for the residual to be low is solely to calculate flow rates that conserve mass for the next step in the PAL solver and not to calculate more accurate film height solutions, the large increase in computation time – in the case of the grid, $N = 2^8$, from approximately 3.5 minutes to over 1.3 hours – means that an alternative means of reducing the residual is desired.

2.7.2 Super-solver

To overcome the problems with mass conservation described above, it is proposed that the EHL solver runs until sufficient convergence of the height profile – as opposed to pressure solution – is reached and thereafter the Reynolds equation can be solved uncoupled from the deformation and load balance equations until a suitable residual remains. This pressure solution is then used only for calculating fluid flow rates such that mass is conserved.

A new convergence criterion for the height profile can be stated such that

$$\max_{\text{over all } i,j} \left\{ \frac{H^n_{i,j} - H^{n-1}_{i,j}}{H^n_{i,j}} \right\} \leq \epsilon_{\text{tol,EHL}} \tag{2.7.2}$$

The converged height and pressure solution are then passed to the Reynolds equation super-solver (RESS). For this uncoupled solver, a Gauss-Seidel scheme has been employed. In this scheme, during the solution iteration of the Reynolds equation, each grid-point is visited in turn and the pressure is solved for using known film heights. The uncoupled Reynolds solver is run with the convergence criteria

$$\max_{\text{over all } i,j} \{|r_R|_{i,j}\} \leq \epsilon_{\text{tol,RESS}}, \qquad \epsilon_{\text{tol,RESS}} = 10^{-3} \tag{2.7.3}$$

Table 2.2 shows the comparative computational times and values of interest for varying levels of convergence tolerance followed by the Reynolds equation super-solver with a grid number of $N = 2^8$. Even for tolerance levels of $\epsilon_{\text{tol,EHL}} = 10^{-3}$ the height profile is well converged, the maximum residual is adequately small such

		$\epsilon_{\text{tol,EHL}}$			
		10^{-3}	10^{-4}	10^{-5}	10^{-6}
C. Time	EHL	33	224	922	2885
	RESS	64	57	52	40
	Comb.	97	281	974	2925

(a) *Computation time [s] for EHL solver, for the Reynolds Equation Super Solver (RESS) and the combined total time.*

		$\epsilon_{\text{tol,EHL}}$			
		10^{-3}	10^{-4}	10^{-5}	10^{-6}
VOI	H_{cen}	0.0564	0.0566	0.0566	0.0566
	H_{min}	0.0402	0.0402	0.0402	0.0402
	P_{max}	0.9831	0.9743	0.9715	0.9711

(b) *Key values of interest (VOI) for varying ϵ_{tol} for the film height convergence criteria of Equations 2.6.2 and 2.7.2.*

Table 2.2: *The effect of decreasing convergence tolerance on (a) computational time – to the nearest second, run on an Intel(R) Core(TM) i5-10210U CPU – and (b) on key values of interest, namely dimensionless central film height at $x = y = 0$, the dimensionless minimum film height and the maximum dimensionless pressure.*

that derived flow rates and velocities will be consistent and conserve mass, and the computational times are small when compared to those of Table 2.1. Figure 2.12 shows a comparison of the pressure solution and residual at the output of the EHL solver and after the RESS. The pressure profile is slightly steeper at the inlet; the effect this has on the calculated flow rates and velocities will be described in §2.8. A minimal change in velocity is preferable to flow rates that do not conserve mass and thus artificially create or destroy protein concentration when used for scalar transport.

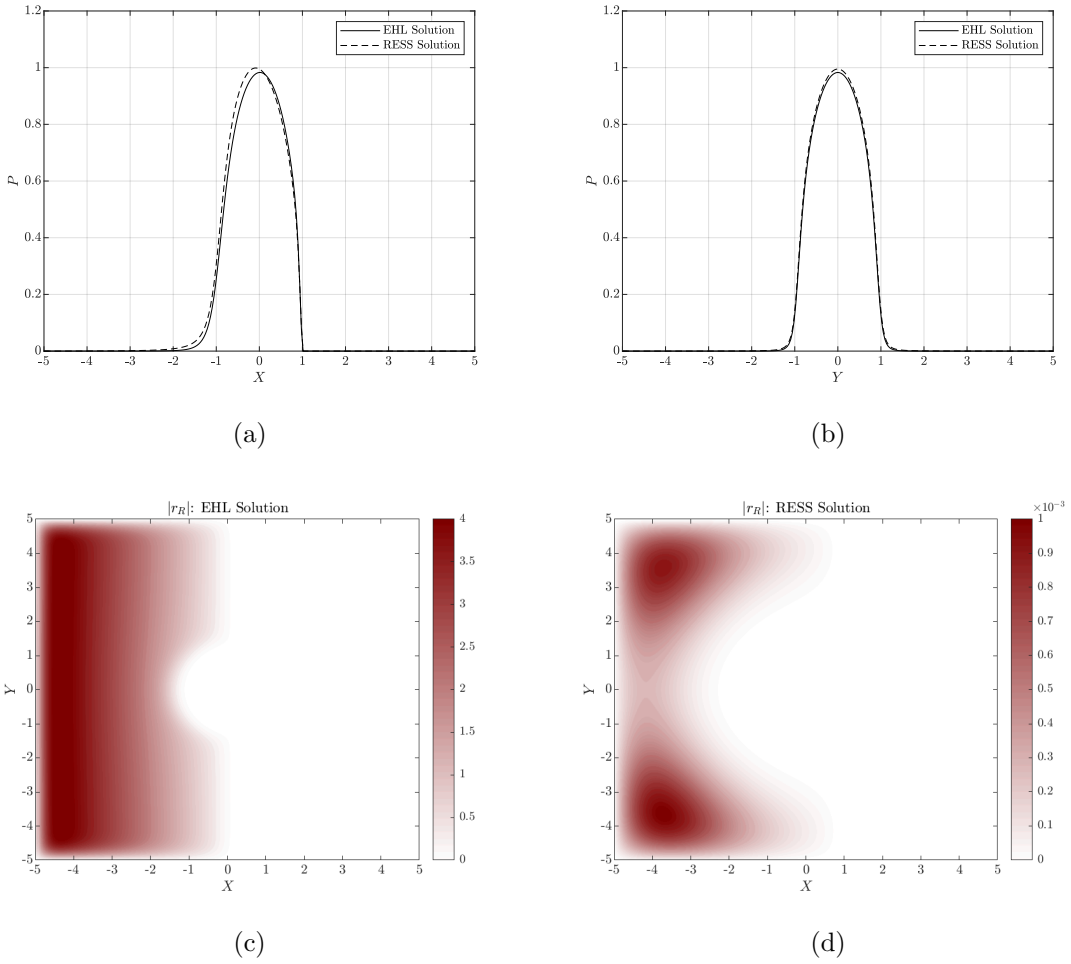


Figure 2.12: *Plots (a) and (b) show comparison of pressure solution from EHL solver and uncoupled RESS along the line $y = 0$ and $x = 0$ respectively. The EHL solution is considered converged at a value of $\epsilon_{\text{tol,EHL}} = 10^{-3}$. Contours (c) and (d) show the residual of the absolute value of the Reynolds residual, r_R, of the initial steady EHL solution after convergence to film height criterion of Equation 2.7.2 and subsequent super-solve of the Reynolds equation. Particular attention should be paid to the contour scale on the right hand side.*

2.8 Fluid flow rates

In order to model the transport of protein concentration at each time-step, the pressure solution from the EHL equations is used to calculate volumetric flow rate of the fluid in each direction as follows:

$$q_x = -\frac{h^3}{12\eta}\frac{\partial p}{\partial x} + u_s\frac{h}{2} \tag{2.8.1}$$

$$q_y = -\frac{h^3}{12\eta}\frac{\partial p}{\partial y} \tag{2.8.2}$$

Using the scaling of Equation 2.3.4 with the added parameters

$$Q_x = q_x/(u_s h_h), \qquad Q_y = q_y/(u_s h_h) \tag{2.8.3}$$

the flow rate equations can be non-dimensionalised as

$$Q_x = -\frac{\epsilon}{2\tilde{\rho}}\frac{\partial P}{\partial X} + \frac{H}{2} \tag{2.8.4}$$

$$Q_y = -\frac{\epsilon}{2\tilde{\rho}}\frac{\partial P}{\partial Y} \tag{2.8.5}$$

where $\epsilon = \tilde{\rho}H^3/\tilde{\eta}\lambda$ as introduced in Equation 2.4.1. The equations are only valid upstream of the cavitation line. In the cavitation region, flow rate is conserved such that Q_x downstream of the cavitation line is constant and equal to the flow rate at the point of cavitation [97]. This model does not calculate the reformation point and thus calculated flow rates in this region are not entirely accurate, however flow downstream of the cavitation line is outside the area of interest.

The flow rates are calculated using central differencing as follows

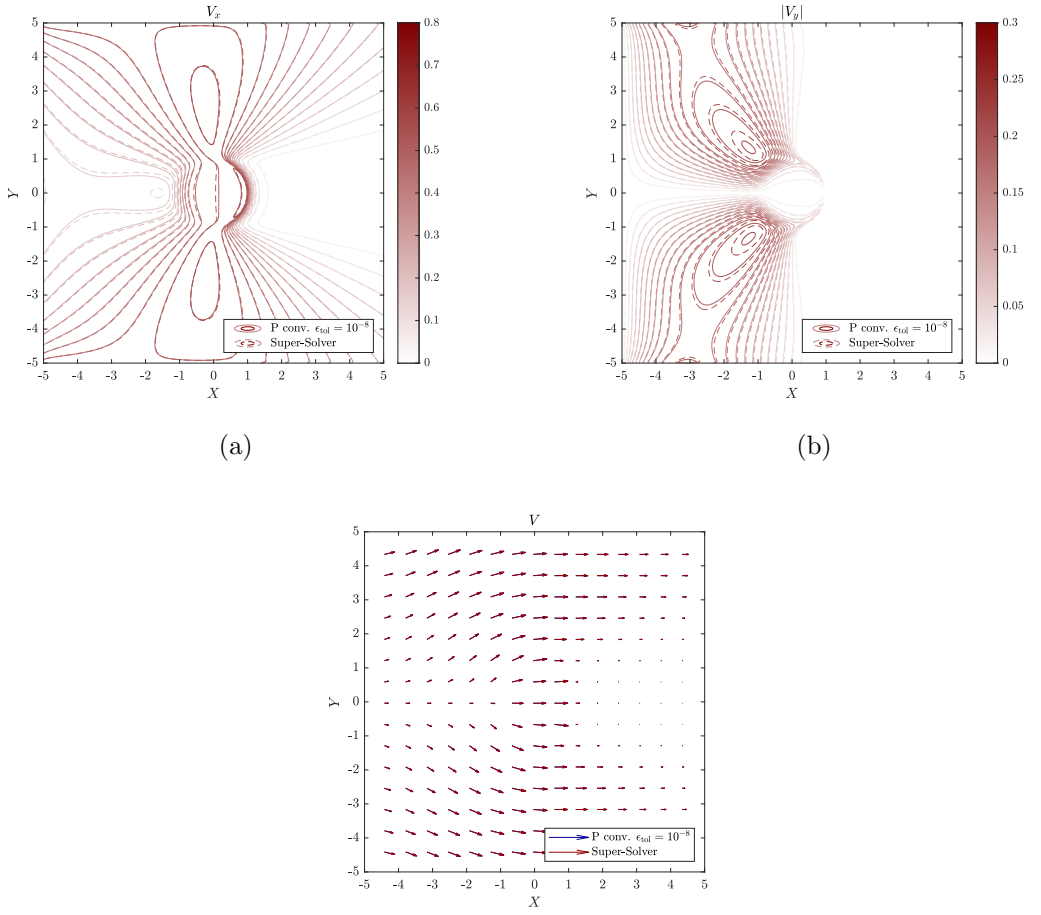
$$(Q_x)_{i,j} = -\frac{\epsilon_{i,j}}{2\tilde{\rho}_{i,j}}\left(\frac{P_{i+1,j} - P_{i-1,j}}{2\Delta X}\right) + \frac{H_{i,j}}{2} \tag{2.8.6}$$

$$(Q_y)_{i,j} = -\frac{\epsilon_{i,j}}{2\tilde{\rho}_{i,j}}\left(\frac{P_{i,j+1} - P_{i,j-1}}{2\Delta Y}\right) \tag{2.8.7}$$

and dimensionless average flow velocities across the lubricating gap can be calculated simply as

$$V_x = \frac{Q_x}{H}, \qquad V_y = \frac{Q_y}{H} \tag{2.8.8}$$

Figure 2.13 shows a comparison of fluid velocities for two simulations. One that relies on the pressure convergence of Equations 2.6.1 and 2.6.2 reaching a tolerance of $\epsilon_{\text{tol,EHL}} = 10^{-8}$. This simulation can be seen in Table 2.1 to take 4790 seconds



(a) (b)

(c)

Figure 2.13: *Comparison of flow velocities between the lowest residual EHL solver simulation – that of pressure convergence to a tolerance of* $\epsilon_{\text{tol}} = 10^{-8}$ *– and that of the EHL solver to a height convergence of* $\epsilon_{\text{tol,EHL}} = 10^{-3}$ *followed by the Reynolds equation super-solver. Contours (a) and (b) show separated x- and y-component magnitudes respectively. Velocities in the y-direction are negative when Y is negative and positive when Y is positive, the absolute values have been plotted here for simplicity. Vector plot (c) shows the direction and magnitude of the velocity field at select grid-points.*

(1.3 hrs) to converge and reaches a maximum Reynolds equation residual of 0.0667, and another that uses the full EHL solver to a film height convergence such that Equations 2.6.2 and 2.7.2 reach $\epsilon_{\text{tol,EHL}} = 10^{-3}$ and the subsequent Reynolds equation super-solver to reduce the maximum residual to a value of 10^{-3} also. This two step simulation takes just 97 seconds combined. It is evident that the contours of magnitude of V_x and V_y differ slightly however the vector plot in Figure 2.13c indicates that the direction of fluid flow differs indistinguishably.

The biggest difference – and the reason for the super-solver at all – can be seen when analysing the derivatives of the flow rates.

$$\frac{\partial Q_x}{\partial X} = \frac{\partial}{\partial X}\left(-\frac{\epsilon}{2\tilde{\rho}}\frac{\partial P}{\partial X} + \frac{H}{2}\right) \tag{2.8.9}$$

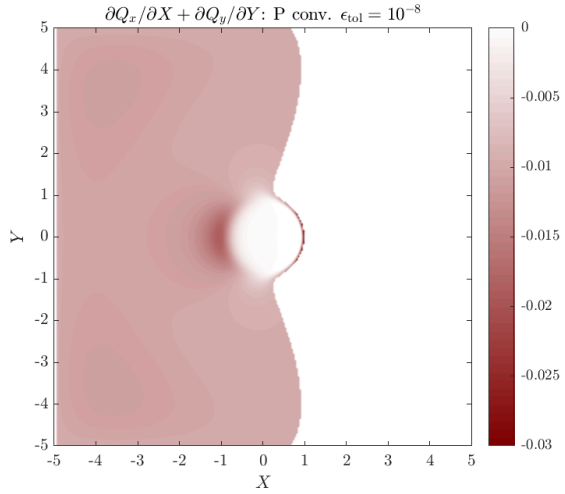
$$\frac{\partial Q_y}{\partial Y} = \frac{\partial}{\partial Y}\left(-\frac{\epsilon}{2\tilde{\rho}}\frac{\partial P}{\partial Y}\right) \tag{2.8.10}$$

These are calculated using the same scheme used to solve the Reynolds equation in Equation 2.4.1 and residual in Equation 2.7.1 such that

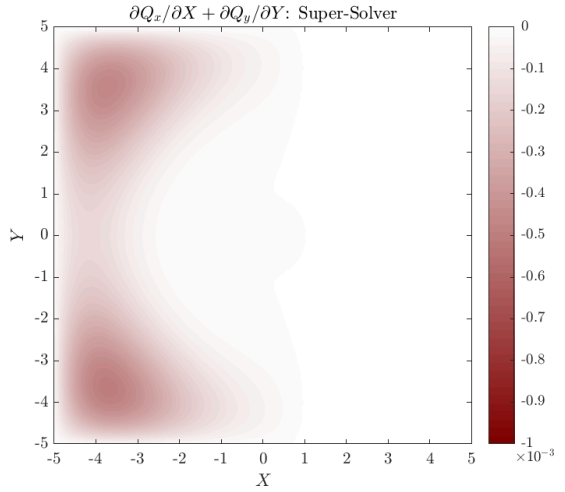
$$\left(\frac{\partial Q_x}{\partial X}\right)_{i,j} = -\left(\frac{\epsilon_{i-1/2,j}(P_{i,j} - P_{i-1,j}) + \epsilon_{i+1/2,j}(P_{i+1,j} - P_{i,j})}{2\tilde{\rho}_{i,j}\Delta X^2}\right) + \frac{H_{i,j} - H_{i-1,j}}{2\Delta X} \tag{2.8.11}$$

$$\left(\frac{\partial Q_y}{\partial X}\right)_{i,j} = -\left(\frac{\epsilon_{i,j-1/2}(P_{i,j} - P_{i,j-1}) + \epsilon_{i,j+1/2}(P_{i,j+1} - P_{i,j}))}{2\tilde{\rho}_{i,j}\Delta Y^2}\right) \tag{2.8.12}$$

Figure 2.14 shows the mass conservation conditions for the two simulations. It can be seen not only that the magnitude of the residual for the full EHL solver solution is larger, but it is also across the entire domain – with the exception of the region post-cavitation which is set to zero – being largest around the contact zone. The sum of the derivatives of the flow rates as calculated from the super-solver solution are much smaller generally but most importantly are at their largest only local to the upstream boundary and away from the contact zone.



(a)



(b)

Figure 2.14: *Comparison of the sum of flow derivatives between (a) the lowest residual EHL solver simulation – that of pressure convergence to a tolerance of* $\epsilon_{\text{tol}} = 10^{-8}$ *– and (b) that of the EHL solver to a height convergence of* $\epsilon_{\text{tol}} = 10^{-3}$ *followed by the Reynolds equation super-solver.*

2.9 Summary

In this chapter, the equations that govern elasto-hydrodynamic theory have been non-dimensionalised, discretised and a solution method proposed for solving the coupled system. The EHL solver has been tested for mesh independence and a mesh number of $N = 2^8$ (a grid of 257x257 nodes) is found to be sufficient. The solver has also been validated against other studies and found to agree well.

Further to traditional solution methods, the inclusion of a novel *Reynolds Equation Super Solver* (RESS) is necessary to ensure that the residual of the Reynolds equation is sufficiently small, such that the pressure solutions can be used to calculate flow rates for use in subsequent solver blocks while ensuring conservation of mass.

The output of this solver block provides fluid flow rate to the *Flow Rate Attenuation* block and receives the viscosity field as input from the *Constitutive Equation* block, both of which are covered in Chapter 4. The blocks that are covered in Chapter 4 can be viewed as in-between handling of information between the EHL solver of this chapter and the *Protein Transport Solver* to be covered in Chapter 3.

Chapter 3

Transport Modelling

3.1 Introduction

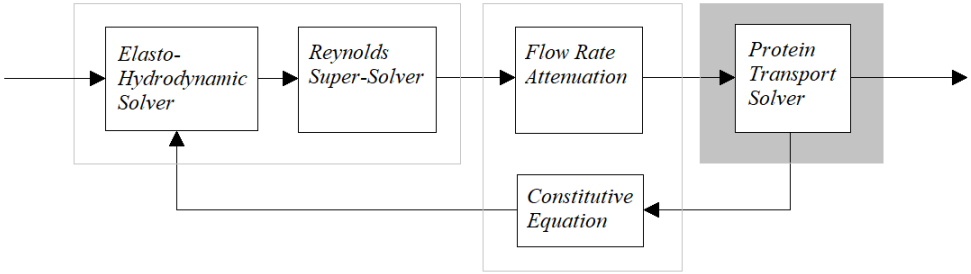


Figure 3.1: *Flow diagram showing overall PAL model schematic and the placement of the protein transport solver block within it. The block receives attenuated flow rates and film heights and outputs protein concentration.*

This chapter focusses on the protein transport solver, the position of which in the overall model flow diagram can be seen in Figure 3.1. The transport of protein matter in the contact zone of this protein aggregation lubrication model is governed by the advection-diffusion equation. This method has been used to model protein movement in previous studies including those of Hron et al., and Bridges and Rajagopal [88, 89], however not for lubricated contacts. In the case of Hron et al. the geometry was a wall-bounded rectangular domain and in the case of Bridges and Rajagopal, the study was of blood plasma in an artery. In these studies, the boundary conditions and initial condition play a pivotal role in determining the evolution of protein concentration over time. Other studies such as those of Pritchard, Wilson et al. [98, 99] use a transport equation that includes shear stress terms that affect the build-up and break-down of a structure parameter to describe aggregation of protein matter along a slowly varying pipe. The hypothesis of this study, however, is that the geometry of the thin film contact zone plays the dominant role in the aggregation of proteins in joint prothesis modelling. How the model captures this geometry-specific aggregation will be covered in Chapter 4 but it is assumed here that shear effects are negligible and as such these terms are not included in the advection-diffusion analysis. The validity of this assumption is discussed in Chapter 5.

3.2 Advection-diffusion

Local protein concentration can be calculated using a scalar transport equation of the form,

$$\frac{\partial c}{\partial t} + \nabla \cdot (\boldsymbol{v}c) - D\nabla^2 c = 0 \tag{3.2.1}$$

where c, $\boldsymbol{v}$ and D are the concentration, velocity and diffusion constant respectively. Because of the thin-film nature of the lubrication problem, it is reasonable to assume that the concentration is constant across the thickness of the fluid film and thus, Eq. 3.2.1 can be integrated in this direction, resulting in the following equation

$$\int_0^h \frac{\partial c}{\partial t} dz + \int_0^h \left(u\frac{\partial c}{\partial x} + v\frac{\partial c}{\partial y} + w\frac{\partial c}{\partial z} \right) dz$$

$$+ \int_0^h \left(c\frac{\partial u}{\partial x} + c\frac{\partial v}{\partial y} + c\frac{\partial w}{\partial z} \right) dz - \int_0^h D\left(\frac{\partial^2 c}{\partial x^2} + \frac{\partial^2 c}{\partial y^2} \right) dz = 0 \tag{3.2.2}$$

The assumption of constant concentration along the z-direction results in

$$h\frac{\partial c}{\partial t} + \frac{\partial c}{\partial x}\int_0^h u\, dz + \frac{\partial c}{\partial y}\int_0^h v\, dz$$

$$+ c\int_0^h \left(\frac{\partial u}{\partial x} + \frac{\partial v}{\partial y} + \frac{\partial w}{\partial z} \right) dz - Dh\left(\frac{\partial^2 c}{\partial x^2} + \frac{\partial^2 c}{\partial y^2} \right) = 0 \tag{3.2.3}$$

The remaining integrals are of either velocities or velocity gradients and these are simply volumetric flow rates or gradients thereof respectively. The flow rates, q_x and q_y, are defined as such

$$q_x = \int_0^h u\, dz, \qquad q_y = \int_0^h v\, dz \tag{3.2.4}$$

reducing Eq. 3.2.3 further to

$$h\frac{\partial c}{\partial t} + \frac{\partial c}{\partial x}q_x + \frac{\partial c}{\partial y}q_y + c\int_0^h \left(\frac{\partial u}{\partial x} + \frac{\partial v}{\partial y} + \frac{\partial w}{\partial z} \right) dz - Dh\left(\frac{\partial^2 c}{\partial x^2} + \frac{\partial^2 c}{\partial y^2} \right) = 0 \tag{3.2.5}$$

The remaining integration can be dealt with using the Leibniz integral rule to interchange integral and differential operators. The extra terms associated with this

rule are all zero due to the no-slip condition at the boundaries. The integral of the $\partial w/\partial z$ term is simply the vertical velocities at the surfaces which are $\partial h/\partial t$ and 0 at the upper and lower surfaces respectively, thus the advection-diffusion equation can be written as:

$$h\frac{\partial c}{\partial t} + \frac{\partial c}{\partial x}q_x + \frac{\partial c}{\partial y}q_y + c\left(\frac{\partial q_x}{\partial x} + \frac{\partial q_y}{\partial y} + \frac{\partial h}{\partial t}\right) - Dh\left(\frac{\partial^2 c}{\partial x^2} + \frac{\partial^2 c}{\partial y^2}\right) = 0 \qquad (3.2.6)$$

3.3 Non-dimensionalisation

Non-dimensionalisation of these equations is carried out using the same scaling as used in Equations 2.3.4 and 2.8.3, and by scaling the concentration by an initial value c_0, such that

$$C = c/c_0. \tag{3.3.1}$$

The resulting non-dimensional equation can be written as

$$\frac{1}{2}\frac{\partial C}{\partial T} + \frac{Q_x}{H}\frac{\partial C}{\partial X} + \frac{Q_y}{H}\frac{\partial C}{\partial Y} + \frac{C}{H}\left(\frac{\partial Q_x}{\partial X} + \frac{\partial Q_y}{\partial Y} + \frac{1}{2}\frac{\partial H}{\partial T}\right) - \frac{1}{\mathrm{Pe}}\left(\frac{\partial^2 C}{\partial X^2} + \frac{\partial^2 C}{\partial Y^2}\right) = 0 \tag{3.3.2}$$

The factors of 1/2 that appear are due to the non-dimensionalisation, $T = tu_s/2a_h$, that was convenient for the Elasto-Hydrodynamic Lubrication analysis. For the purposes of discussing the transport of protein concentration it is useful to use the non-dimensionalisation, $\tau = tu_s/a_h$, noting that $\tau = 2T$. This gives the more convenient advection-diffusion equation

$$\frac{\partial C}{\partial \tau} + \frac{Q_x}{H}\frac{\partial C}{\partial X} + \frac{Q_y}{H}\frac{\partial C}{\partial Y} + \frac{C}{H}\left(\frac{\partial Q_x}{\partial X} + \frac{\partial Q_y}{\partial Y} + \frac{\partial H}{\partial \tau}\right) - \frac{1}{\mathrm{Pe}}\left(\frac{\partial^2 C}{\partial X^2} + \frac{\partial^2 C}{\partial Y^2}\right) = 0 \tag{3.3.3}$$

where Pe is the Péclet number, defined as

$$\mathrm{Pe} = \frac{u_s a_h}{D} \tag{3.3.4}$$

3.4 Discretisation

To start discretising the transport equation, it is best to move the temporal term to the left and the spatial terms to the right hand side as these will be dealt with differently. This results in the following form where the right hand side can be vectorised

$$\frac{\partial C}{\partial \tau} = \mathrm{RHS}(C) \tag{3.4.1}$$

3.4.1 Spatial discretisation

The flow rates, Q_x and Q_y, and their derivatives along with the squeeze term, $\partial H/\partial \tau$, are calculated at each grid-point prior to solving the advection-diffusion equation thus the conservation terms are the simplest to implement:

$$\frac{C}{H}\left(\frac{\partial Q_x}{\partial X} + \frac{\partial Q_y}{\partial Y} + \frac{\partial H}{\partial \tau}\right) \approx \frac{C_{i,j}}{H_{i,j}}\left(\left(\frac{\partial Q_x}{\partial X}\right)_{i,j} + \left(\frac{\partial Q_y}{\partial Y}\right)_{i,j} + \left(\frac{\partial H}{\partial \tau}\right)_{i,j}\right) \tag{3.4.2}$$

The diffusion terms can be discretised using a second order central difference scheme as follows:

$$\frac{1}{\mathrm{Pe}}\left(\frac{\partial^2 C}{\partial X^2} + \frac{\partial^2 C}{\partial Y^2}\right) \approx \frac{1}{\mathrm{Pe}}\left(\frac{C_{i-1,j} - 2C_{i,j} + C_{i+1,j}}{\Delta X^2} + \frac{C_{i,j-1} - 2C_{i,j} + C_{i,j+1}}{\Delta Y^2}\right) \tag{3.4.3}$$

The advection terms can be handled in a number of ways and here focus is on the second order central method and the first order upwind method. Upwinding – using gradient approximations exclusively from the upstream direction – is a useful tool for maintaining stability of advection solutions particularly when using explicit Euler methods – discussed further in § 3.4.2.

The central differencing scheme results in the following approximations for the advection terms:

$$\frac{Q_x}{H}\frac{\partial C}{\partial X} \approx \left(\frac{Q_x}{H}\right)_{i,j} \frac{C_{i+1,j} - C_{i-1,j}}{2\Delta X} \tag{3.4.4}$$

$$\frac{Q_y}{H}\frac{\partial C}{\partial Y} \approx \left(\frac{Q_y}{H}\right)_{i,j} \frac{C_{i,j+1} - C_{i,j-1}}{2\Delta Y} \tag{3.4.5}$$

The upwind scheme results in the following approximations for the advection terms (assuming here that the flow velocity is positive in the x- and y-directions)

$$\frac{Q_x}{H}\frac{\partial C}{\partial X} \approx \left(\frac{Q_x}{H}\right)_{i,j} \frac{C_{i,j} - C_{i-1,j}}{\Delta X} \tag{3.4.6}$$

$$\frac{Q_y}{H}\frac{\partial C}{\partial Y} \approx \left(\frac{Q_y}{H}\right)_{i,j} \frac{C_{i,j} - C_{i,j-1}}{\Delta Y} \tag{3.4.7}$$

These finite difference approximations can be used to create a matrix equation that models the right hand side of Equation 3.4.1 such that

$$\mathrm{RHS}(C) \approx \boldsymbol{Ac} \tag{3.4.8}$$

The process is the same for any spatial discretisation scheme be it central differenced advection, upwind advection or a combination such that upwinding is used in the x-direction – the direction in which the global sliding velocity acts – and central differencing in the y-direction. Here the steps are shown for a scheme in which central differencing is used for both advection terms.

Gathering the terms for each concentration location in the form

$$\mathrm{RHS}(C)_{i,j} \approx A_c C_{i,j} + A_{x-} C_{i-1,j} + A_{x+} C_{i+1,j} + A_{y-} C_{i,j-1} + A_{y+} C_{i,j+1} \tag{3.4.9}$$

results in the following coefficients

$$A_c = \left\{ \frac{1}{H_{i,j}} \left(\left(\frac{\partial Q_x}{\partial X}\right)_{i,j} + \left(\frac{\partial Q_y}{\partial Y}\right)_{i,j} + \left(\frac{\partial H}{\partial \tau}\right)_{i,j} \right) + \frac{1}{\mathrm{Pe}} \left(\frac{2}{\Delta X^2} + \frac{2}{\Delta Y^2} \right) \right\} \tag{3.4.10}$$

$$A_{x-} = \left\{ \frac{1}{2\Delta X} \left(\frac{Q_x}{H}\right)_{i,j} + \frac{1}{\mathrm{Pe}} \left(\frac{1}{\Delta X^2} \right) \right\} \tag{3.4.11}$$

$$A_{x+} = \left\{ -\frac{1}{2\Delta X} \left(\frac{Q_x}{H}\right)_{i,j} + \frac{1}{\mathrm{Pe}} \left(\frac{1}{\Delta X^2} \right) \right\} \tag{3.4.12}$$

$$A_{y-} = \left\{ \frac{1}{2\Delta Y} \left(\frac{Q_y}{H}\right)_{i,j} + \frac{1}{\mathrm{Pe}} \left(\frac{1}{\Delta Y^2} \right) \right\} \tag{3.4.13}$$

$$A_{y+} = \left\{ -\frac{1}{2\Delta Y} \left(\frac{Q_y}{H} \right)_{i,j} + \frac{1}{\mathrm{Pe}} \left(\frac{1}{\Delta Y^2} \right) \right\} \tag{3.4.14}$$

If the concentration at each point in the $(N+1) \times (N+1)$ domain are stored in a vector organised as follows

$$\boldsymbol{c} = \begin{bmatrix} C_{1,1} \\ C_{2,1} \\ \vdots \\ C_{i,j-1} \\ \vdots \\ C_{i-1,j} \\ C_{i,j} \\ C_{i+1,j} \\ \vdots \\ C_{i,j+1} \\ \vdots \\ C_{N,N+1} \\ C_{N+1,N+1} \end{bmatrix} \tag{3.4.15}$$

then the right hand side for an internal point at location i, j can be calculated by a multiplication of vectors.

$$\mathrm{RHS}(C)_{i,j} \approx \begin{bmatrix} 0 & \cdots & A_{y-} & \cdots & A_{x-} & A_c & A_{x+} & \cdots & A_{y+} & \cdots & 0 \end{bmatrix} \begin{bmatrix} \\ \boldsymbol{c} \\ \\ \end{bmatrix} \tag{3.4.16}$$

External points at the edges of the domain are created far enough away from the contact region that the boundary condition $\partial C / \partial \tau = 0$ is used such that

$$\begin{aligned} C_{1,j}^{n+1} &= C_{1,j}^{n} \\ C_{N+1,j}^{n+1} &= C_{N+1,j}^{n} \\ C_{i,1}^{n+1} &= C_{i,1}^{n} \\ C_{i,N+1}^{n+1} &= C_{i,N+1}^{n} \end{aligned} \tag{3.4.17}$$

With these conditions, the full matrix, $\boldsymbol{A}$, can be built in the following manner, whereby the sub-matrices

$$\boldsymbol{A}_c = \begin{bmatrix} 0 & & & & \\ A_{x-} & A_c & A_{x+} & & \\ & \ddots & \ddots & \ddots & \\ & & A_{x-} & A_c & A_{x+} \\ & & & & 0 \end{bmatrix} \tag{3.4.18}$$

$$\boldsymbol{A}_{y-} = \begin{bmatrix} 0 & & & & \\ & A_{y-} & & & \\ & & \ddots & & \\ & & & A_{y-} & \\ & & & & 0 \end{bmatrix}, \quad \boldsymbol{A}_{y+} = \begin{bmatrix} 0 & & & & \\ & A_{y+} & & & \\ & & \ddots & & \\ & & & A_{y+} & \\ & & & & 0 \end{bmatrix} \tag{3.4.19}$$

are used to form the sparse matrix which contains five non-zero diagonals

$$\boldsymbol{A} = \begin{bmatrix} \boldsymbol{0} & & & & \\ \boldsymbol{A}_{y-} & \boldsymbol{A}_c & \boldsymbol{A}_{y+} & & \\ & \ddots & \ddots & \ddots & \\ & & \boldsymbol{A}_{y-} & \boldsymbol{A}_c & \boldsymbol{A}_{y+} \\ & & & & \boldsymbol{0} \end{bmatrix} \tag{3.4.20}$$

such that

$$\mathrm{RHS}(C) \approx \begin{bmatrix} & \boldsymbol{A} & \end{bmatrix} \begin{bmatrix} \\ \boldsymbol{c} \\ \\ \end{bmatrix} \tag{3.4.21}$$

3.4.2 Temporal discretisation

It is common to discretise the time derivative of the left hand side as follows

$$\frac{\partial C_{i,j}}{\partial \tau} \approx \frac{C_{i,j}^{n+1} - C_{i,j}^{n}}{\Delta \tau} \tag{3.4.22}$$

where the superscript, n, denotes the current time-step and $n+1$, the subsequent time-step. The relation of left to right hand side can take a number of forms, and here we will address the θ-methods which are of the form

$$\frac{\boldsymbol{c}^{n+1}-\boldsymbol{c}^{n}}{\Delta\tau}=(1-\theta)\boldsymbol{A}\boldsymbol{c}^{n}+\theta\boldsymbol{A}\boldsymbol{c}^{n+1} \tag{3.4.23}$$

Setting θ to 0, 1, and 1/2 gives rise to the *'explicit'* (or *'forward'*) Euler, *'implicit'* (or *'backward'*) Euler and *'Crank-Nicolson'* methods respectively.

The explicit Euler method is of first order accuracy and is known to be stable only when the Courant-Friedrichs-Lewy (CFL) condition is met. This condition imposes an upper limit on the time-step such that $u\Delta\tau/\Delta X \leqslant 1$, and similarly for the y-direction [100]. Furthermore upwinding spatial schemes are frequently used with explicit Euler schemes because information about the next time-step is travelling from upstream. The solution for the subsequent time-step is calculated as

$$\frac{\boldsymbol{c}^{n+1}-\boldsymbol{c}^{n}}{\Delta\tau}=\boldsymbol{A}\boldsymbol{c}^{n} \tag{3.4.24}$$

$$\boldsymbol{c}^{n+1}=(\boldsymbol{I}+\Delta\tau\boldsymbol{A})\boldsymbol{c}^{n} \tag{3.4.25}$$

needing only a matrix multiplication and is thus the simplest method to implement.

The implicit Euler method is stable for all values of $\Delta\tau$ and furthermore, as the right hand side uses the next time-step as its domain, the need for upwinding is relaxed. This scheme is also first order accurate in time and is solved as follows

$$\frac{\boldsymbol{c}^{n+1}-\boldsymbol{c}^{n}}{\Delta\tau}=\boldsymbol{A}\boldsymbol{c}^{n+1} \tag{3.4.26}$$

$$\boldsymbol{c}^{n+1}=(\boldsymbol{I}-\Delta\tau\boldsymbol{A})^{-1}\boldsymbol{c}^{n} \tag{3.4.27}$$

requiring a matrix inversion to solve, which is more costly than the explicit method.

The Crank-Nicolson method uses both the current and next time-step in the right hand side and is of second order accuracy. The solution is found as follows

$$\frac{\boldsymbol{c}^{n+1}-\boldsymbol{c}^{n}}{\Delta\tau}=\frac{1}{2}\boldsymbol{A}\boldsymbol{c}^{n}+\frac{1}{2}\boldsymbol{A}\boldsymbol{c}^{n+1} \tag{3.4.28}$$

$$\boldsymbol{c}^{n+1}=(\boldsymbol{I}-\frac{\Delta\tau}{2}\boldsymbol{A})^{-1}(\boldsymbol{I}+\frac{\Delta\tau}{2}\boldsymbol{A})\boldsymbol{c}^{n} \tag{3.4.29}$$

and requires the most costly matrix manipulation to solve, with what is fundamentally an explicit step of $\Delta\tau/2$ followed by an implicit step of the same size.

3.5 Scheme testing

To test validity and accuracy of the advection-diffusion solver it is possible to test it against some well-studied analytic cases. Most cases deal with purely one- or two-dimensional advection-diffusion problems and as such it is possible to set H to unity for the following test cases, thereby effectively reducing the flow rates to velocities such that the equation looks more conventional:

$$\frac{\partial C}{\partial \tau} + V_x \frac{\partial C}{\partial X} + V_y \frac{\partial C}{\partial Y} + C\left(\frac{\partial V_x}{\partial X} + \frac{\partial V_y}{\partial Y}\right) - \frac{1}{\mathrm{Pe}}\left(\frac{\partial^2 C}{\partial X^2} + \frac{\partial^2 C}{\partial Y^2}\right) = 0 \tag{3.5.1}$$

where

$$V_x = Q_x/H, \qquad V_y = Q_q/H. \tag{3.5.2}$$

After the schemes have been tested, this assumption can be relaxed when analysing the lubricated contact geometry.

3.5.1 Gaussian pulse

The first test case is that of a Gaussian pulse that has initial form

$$C(X, Y, 0) = \exp(-\mathrm{Pe}(X - X_{\mathrm{init}})^2 - \mathrm{Pe}(Y - Y_{\mathrm{init}})^2) \tag{3.5.3}$$

where X_{init} and Y_{init} are the initial coordinates of the Gaussian peak. The evolution of this pulse over time follows the following analytic expression [101]

$$C(X, Y, \tau) = \frac{1}{1 + 4\tau} \exp\left(-\mathrm{Pe}\frac{(X - X_{\mathrm{init}} - V_x\tau)^2}{1 + 4\tau} - \mathrm{Pe}\frac{(Y - Y_{\mathrm{init}} - V_y\tau)^2}{1 + 4\tau}\right) \tag{3.5.4}$$

where V_x and V_y are constant in space and time. The initial starting point of the peak was set to $X_{\mathrm{init}} = Y_{\mathrm{init}} = 0.4$ and the simulation was run for a duration of $\tau = 0.2$. The results of simulations at multiple Péclet numbers and values of $\Delta\tau$ are shown in Figures 3.2 and 3.3.

Figure 3.2 shows the results of several different schemes predicting the solution to the Gaussian pulse advection-diffusion problem with a Péclet number of 100 and velocities $V_x = V_y = 1$. The solutions are fully 2D, however, for comparison, only the slice along $X = Y$ is plotted. The grid is such that $N = 2^7$ over the domain

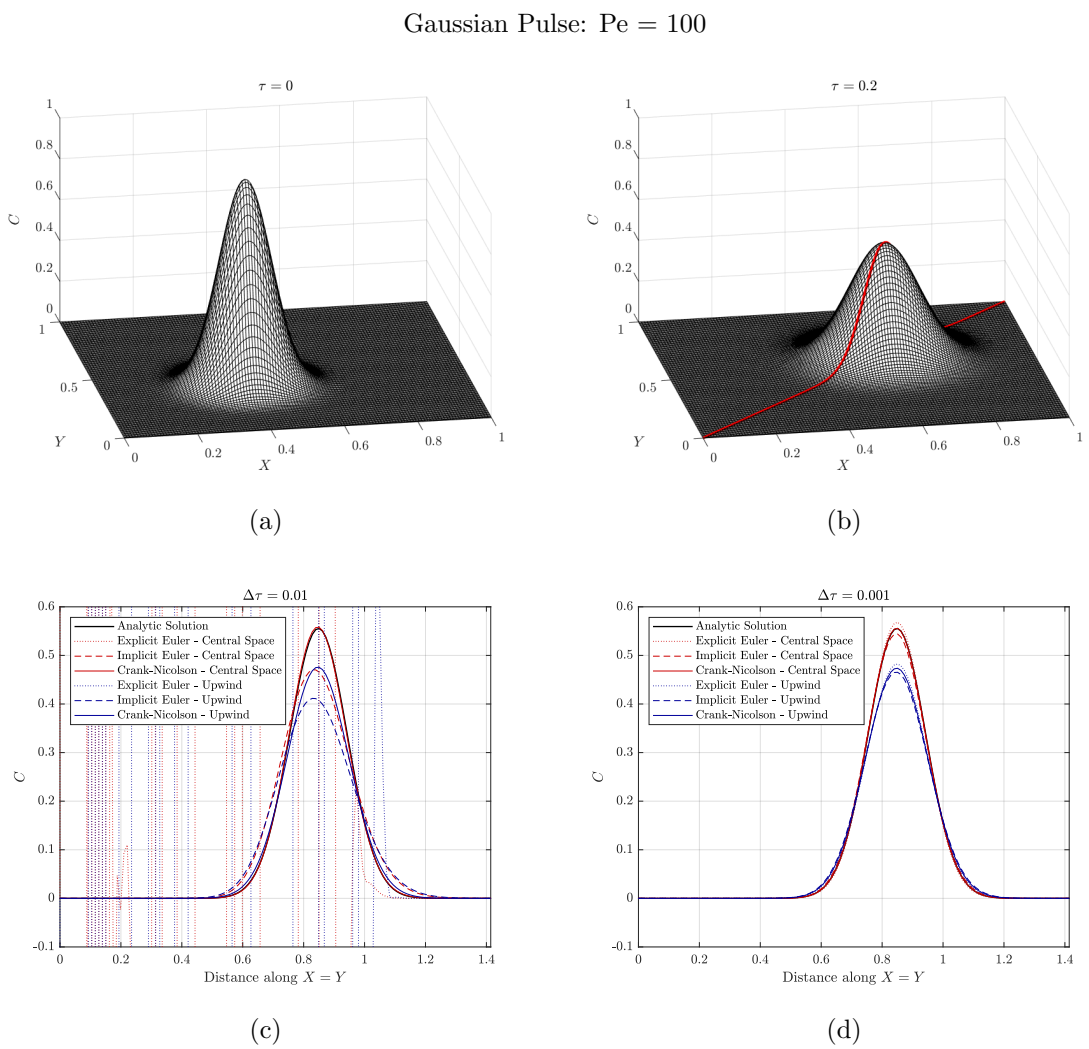


Figure 3.2: *Gaussian pulse simulations at* Pe $= 100$ *where (a) shows the initial condition at* $\tau = 0$ *and (b) shows the analytic result at* $\tau = 0.2$*. The red line shows the slice along* $X = Y$ *along which the following plots (c) and (d) are shown with simulations using time-steps of* $\Delta\tau = 0.01$ *and* $\Delta\tau = 0.001$ *respectively.*

$0 \leqslant X, Y \leqslant 1$, which gives a value of $\Delta X = 0.00781$. Time-steps have been chosen at values of $\Delta\tau = 0.01$ and $\Delta\tau = 0.001$ such that the results of violating and meeting the CFL condition can be analysed. When the time-step is larger, the explicit Euler method leads to an unstable solution and the difference in accuracy between the implicit Euler and the Crank-Nicolson methods is evident. When the time-step becomes smaller, the explicit method is stable and the difference in accuracy of the different temporal schemes becomes smaller as expected. The inaccuracy of the first order upwind method is persistent across both simulations and will only improve with increased grid density, which is more expensive than increased time density.

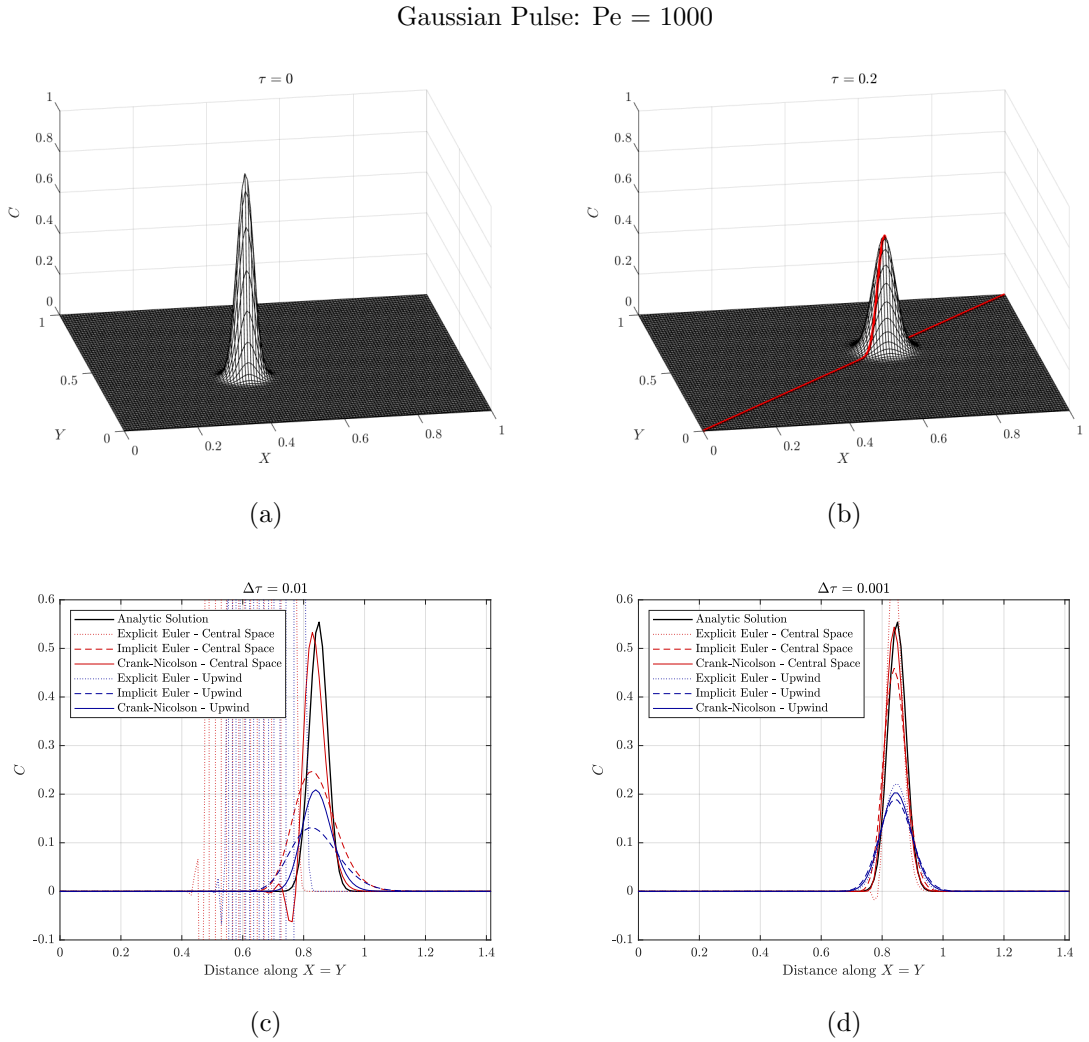


Figure 3.3: *Gaussian pulse simulations at* Pe = 1000 *where (a) shows the initial condition at* $\tau = 0$ *and (b) shows the analytic result at* $\tau = 0.2$. *The red line shows the slice along* $X = Y$ *along which the following plots (c) and (d) are shown with simulations using time-steps of* $\Delta\tau = 0.01$ *and* $\Delta\tau = 0.001$ *respectively.*

Increasing the Péclet number to 1000 as is shown in Figure 3.3 results in the disparity of solution accuracy between the second order central scheme and the first order upwind scheme becoming more apparent. Another feature of this higher Péclet simulation is the introduction of oscillatory behaviour in the Crank-Nicolson scheme at larger time-steps. This is a well-known feature of the scheme and occurs because this method is partly reliant on a sub explicit Euler step. This oscillatory behaviour does not manifest in the upwind schemes because the numerical diffusion present is enough to artificially smooth the high gradient. The fully implicit method does not suffer from these oscillations but still requires an adequately small time-step to be considered accurate.

3.5.2 High gradients

To better understand the behaviour of these schemes near high concentration gradients, simulations were run for initial conditions of a discontinuous step down from $C = 1$ to 0 and also the equivalent step up from 0 to 1.

$$\text{Step down:} \qquad C(X,0) = \begin{cases} 1, & \text{for } X \leqslant 0.4 \\ 0, & \text{for } X > 0.4. \end{cases} \tag{3.5.5}$$

$$\text{Step up:} \qquad C(X,0) = \begin{cases} 0, & \text{for } X \leqslant 0.4 \\ 1, & \text{for } X > 0.4 \end{cases} \tag{3.5.6}$$

The analytic solution for the advection-diffusion of these initial conditions are as shown [102]

$$\text{Step down:} \quad C(X,\tau) = \frac{1}{2}\left(1 - \operatorname{erf}\left(\frac{X - X_{\text{init}} - V_x\tau}{\sqrt{4D\tau}}\right)\right) \tag{3.5.7}$$

$$\text{Step up:} \quad C(X,\tau) = \frac{1}{2}\left(1 + \operatorname{erf}\left(\frac{X - X_{\text{init}} - V_x\tau}{\sqrt{4D\tau}}\right)\right) \tag{3.5.8}$$

For these simulations the domain $0 \leqslant X \leqslant 1$ is split in to steps of $\Delta X = 0.01$ and again run with time-steps of both $\Delta\tau = 0.01$ and 0.001. The velocity, $V_x = 1$ and the initial conditions are such that the step change occurs at $X_{\text{init}} = 0.4$ in both cases. If the dominant length scale and velocity are both unity, the diffusion constant, D, is simply, 1/Pe. The simulations were run for a total time of $\tau = 0.2$ and the results can be seen in Figures 3.4 and 3.5.

These simulations show similar behaviour to those for the Gaussian pulse with respect to the upwind schemes showing more numerical diffusion than the central schemes. The instability of the explicit Euler methods and the oscillatory behaviour of the Crank-Nicolson scheme at larger time-steps are also still apparent, however, in Figures 3.4f and 3.5f all three central differencing schemes also suffer from spurious oscillations. This phenomena is due to the spatial density rather than temporal density and is know to occur where concentration gradients are especially large. Sufficient diffusion – whether physical or numerical – will suppress the onset of these spurious oscillations and as such they are not present in the solutions involving lower Péclet number. The oscillations can also be suppressed with sufficient spatial grid density.

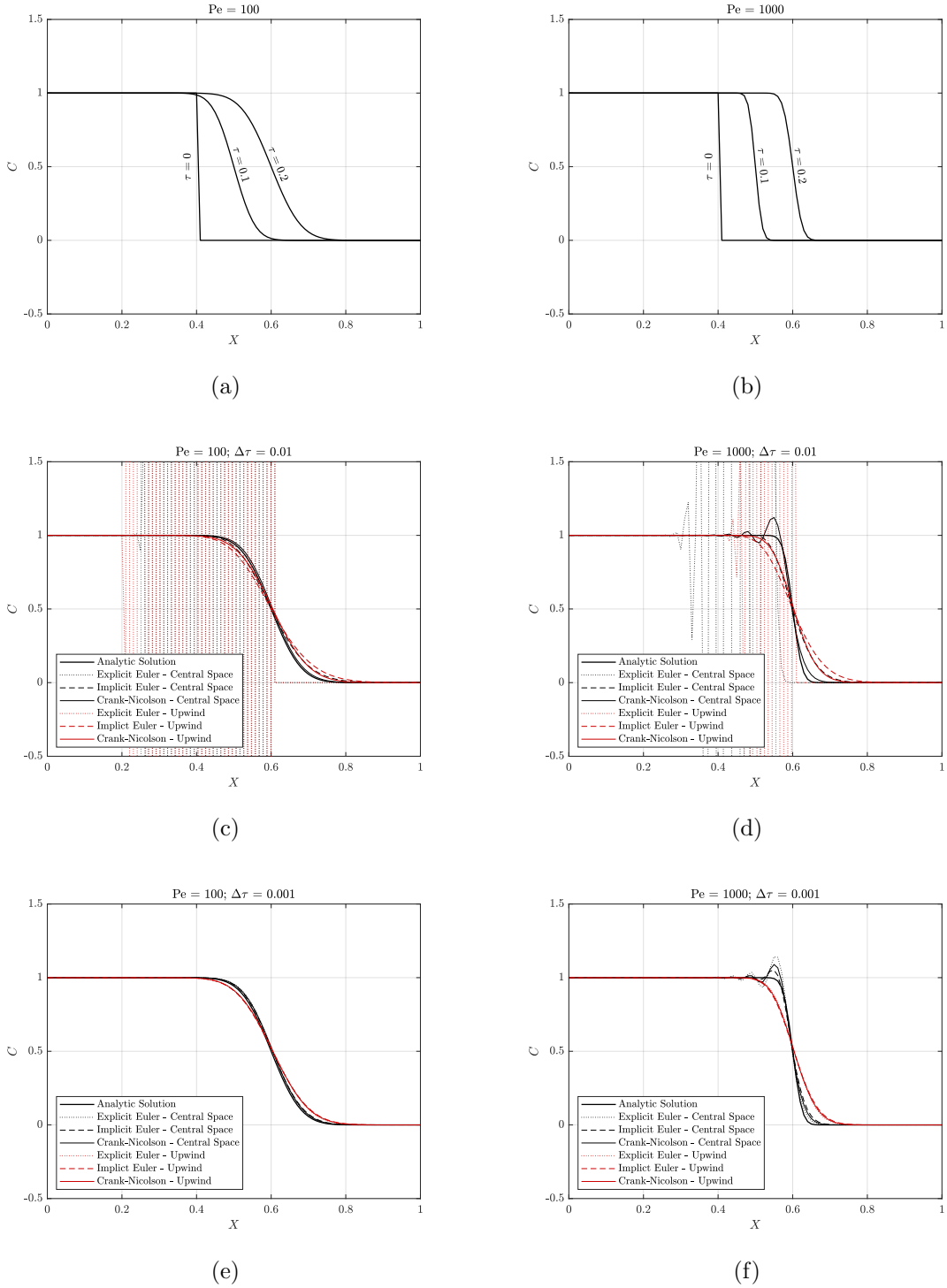


Figure 3.4: *Comparison of numerical simulation with analytic solution to the advection-diffusion of a downward step function. The uppermost plots (a) and (b) show the analytic solution at times* $\tau = 0, 0.1$ *and* 0.2 *for Péclet numbers 100 and 1000 respectively. The following plots (c),(d),(e) and (f) show the comparison at time* $\tau = 0.2$ *of the analytic solution with those of the different numerical schemes using time-steps* $\Delta\tau = 0.01$ *and* 0.001.

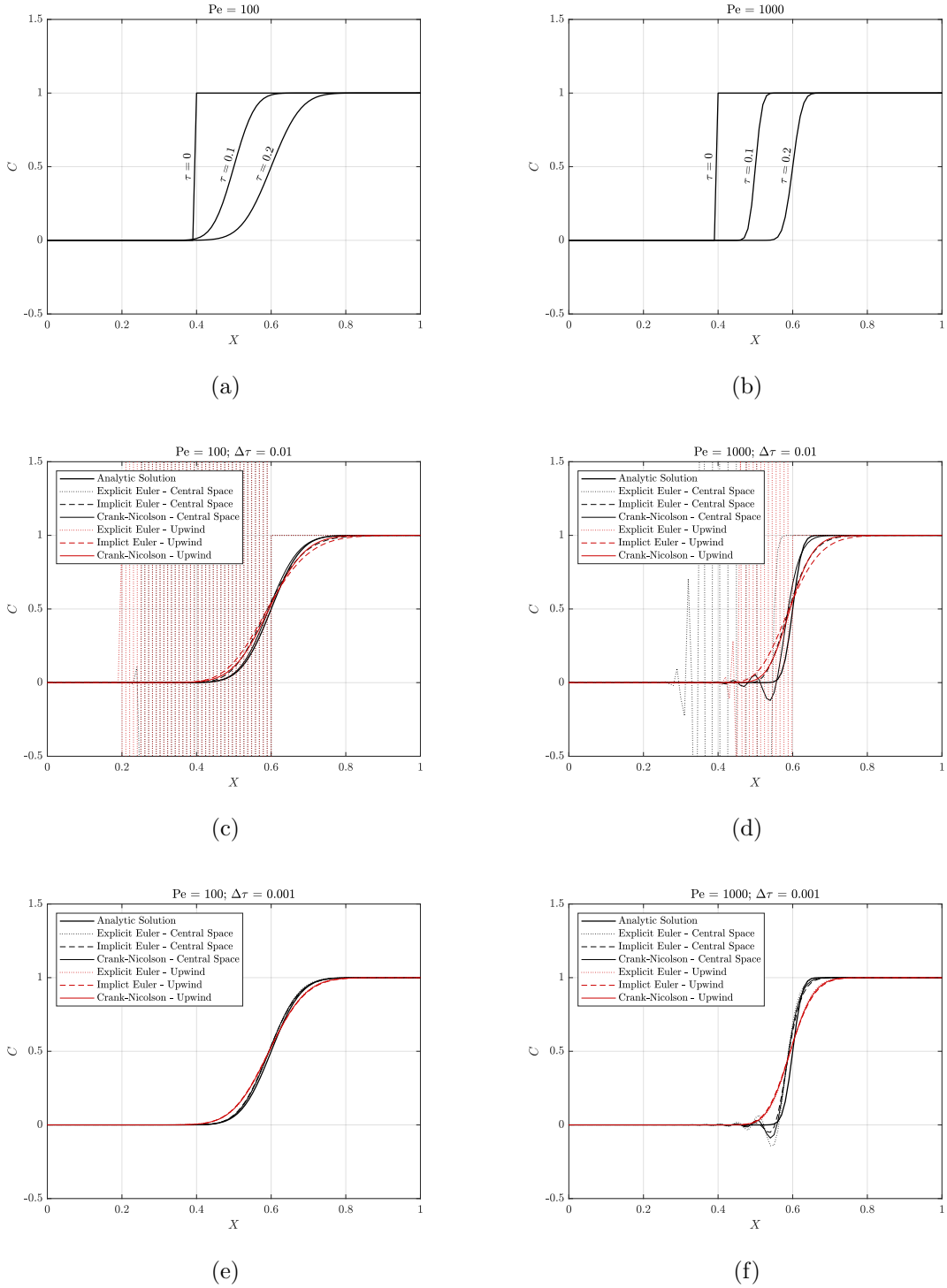


Figure 3.5: *Comparison of numerical simulation with analytic solution to the advection-diffusion of an upward step function. The uppermost plots (a) and (b) show the analytic solution at times* $\tau = 0, 0.1$ *and* 0.2 *for Péclet numbers 100 and 1000 respectively. The following plots (c),(d),(e) and (f) show the comparison at time* $\tau = 0.2$ *of the analytic solution with those of the different numerical schemes using time-steps* $\Delta\tau = 0.01$ *and* 0.001.

3.6 Conservation terms

Having tested the validity of the developed solver on conventional advection-diffusion problems, the final terms to be addressed are the flow rate conservation terms. For the calculated fluid flow rates of the EHL contact the terms

$$\frac{\partial Q_x}{\partial X} + \frac{\partial Q_y}{\partial Y} + \frac{\partial H}{\partial \tau} = 0 \tag{3.6.1}$$

are necessarily equal to zero as a result of mass conservation. In fact, Equation 3.6.1 is indeed just the Reynolds equation in an alternate form. Although this is still true of the fluid, the protein matter itself is modelled with attenuated flow rates. These terms are no longer necessarily equal to zero and must be included in the scalar transport solver. The effect of flow rate attenuation on the transport of protein matter is covered in Chapter 4.

3.6.1 Squeeze term

It is possible to examine the effect of the squeeze term, $\partial H/\partial \tau$, independently and the role that this transient behaviour has on protein concentration. It is noted that if all flow rates are set to zero, and in the absence of any diffusion, the amount of protein matter across the thin film at any given point should remain constant. The total protein content is calculated by multiplying the concentration by the height of the gap, i.e

$$\frac{\partial}{\partial t}(ch) = 0 \tag{3.6.2}$$

which can be expanded to give the relation

$$\frac{\partial c}{\partial t} = -\frac{c}{h}\frac{\partial h}{\partial t} \tag{3.6.3}$$

the non-dimensionalised form of which can be obtained by setting $Q_x = Q_y = 1/\mathrm{Pe} = 0$ in Equation 3.3.3 such that

$$\frac{\partial C}{\partial \tau} = -\frac{C}{H}\frac{\partial H}{\partial \tau}. \tag{3.6.4}$$

The derivative of height with time is calculated for this test case such that

$$\frac{C_{i,j}^{n+1} - C_{i,j}^{n}}{\Delta \tau} = -\frac{1}{H_{i,j}^{n+1}}\frac{H_{i,j}^{n+1} - H_{i,j}^{n}}{\Delta \tau} C_{i,j}^{n+1} \tag{3.6.5}$$

Setting H^n to that of the steady state EHL solution from Chapter 2 and C^n to unity across the domain a simulation setting flow rates and diffusion terms to zero

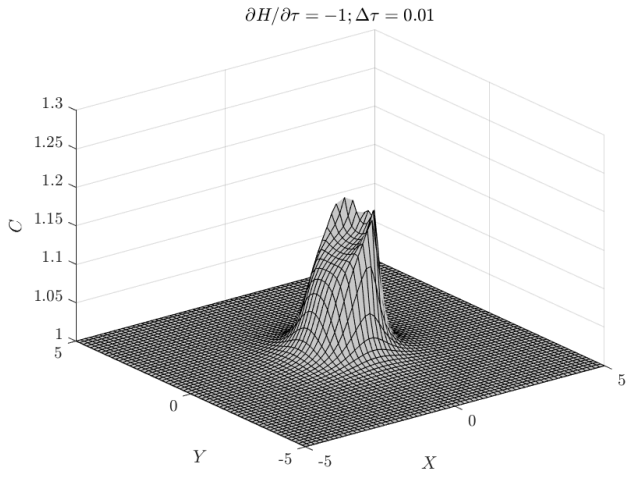


Figure 3.6: *Concentration profile after simulation step of* $\Delta\tau = 0.01$ *and rate of change of film height set to* $\partial H/\partial\tau = -1$ *across the domain. The simulation was run with a grid density of* $N = 2^7$ *but downsampled to a grid density of* $N = 2^5$ *when plotted to aid visualisation.*

was run for a time-step of $\Delta\tau = 0.01$ and $\partial H/\partial\tau = -1$ at all points such that $H^{n+1} = H^n + \Delta\tau(\partial H/\partial\tau) = H^n - 0.01$.

Figure 3.6 shows the results of a decreasing gap height on the concentration of protein throughout the lubricating domain. In the contact region where film height is smallest, relatively large changes in concentration are seen. In regions further away from the contact zone, where film heights are much larger, the squeeze term has minimal effect and the concentration stays close to unity. For a film height that is increasing, i.e. $\partial H/\partial\tau > 0$, concentration would decrease in the same manner. This term ensures the conservation of total protein mass.

3.7 Unknown value problem

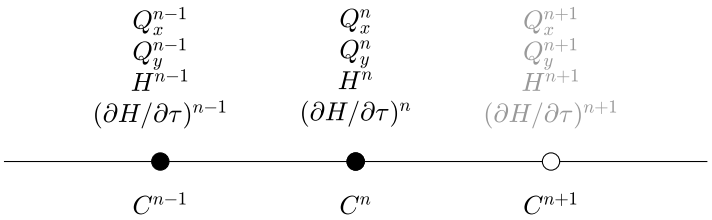


Figure 3.7: *Diagram showing available known variables at each time-step of the transport problem. C^{n+1} can be used for calculations of the implicit scheme, however the film height and flow rate conditions at that time-step are not yet known.*

Until now, the scalar transport solver has been tested on cases where Q_x, Q_y and H have been constant – or in the case of the squeeze term, known – however when using the values as calculated by the EHL solver, all of these values are varying in time. For this reason, it matters which time-step is used in calculating those terms that are included in the right hand side matrix. They should match the temporal scheme and therefore the matrix, $\boldsymbol{A}$, will be different for explicit and implicit methods. For the Crank-Nicolson method this requires both the explicit matrix and implicit matrix to be calculated. Figure 3.7 highlights an issue with the full protein aggregation lubrication model in that the film height and flow conditions of the next time-step are unknown, and cannot be calculated until the resulting concentration profile from the transport solver can be applied via the constitutive equation back into the elasto-hydrodynamic solver. It is desirable to use the implicit Euler scheme for its stability over the explicit Euler method and even over the Crank-Nicolson method – the increased accuracy of which comes also with the potential for oscillatory behaviour. To do so, however, would entail creating the matrix, $\boldsymbol{A}$, with conditions from the current time-step instead of the subsequent. If the time-steps are sufficiently small, any error incurred by this scheme are minimised. The efficacy of this approach is analysed in Chapter 5.

3.8 Summary

In this chapter, a protein transport solver that models the movement of protein concentration has been developed. The advection-diffusion equation that governs this behaviour has been non-dimensionalised and multiple discretisation methods have been introduced. The solver and discretisation methods have been verified against known solution test cases and found to agree well under certain conditions, namely if sufficiently high order advection scheme, mesh density and time-step density are used.

The implicit Euler temporal discretisation scheme has been chosen for it's stability. A second order central differencing spatial discretisation scheme has been chosen for the advection terms, which are the primary source of solver instability. It is noted that this scheme is revisited after model calibration to provide higher order schemes by introducing additional diagonals in the solution matrix, $\mathbf{A}$.

This *Protein Transport Solver* block takes protein flow rates as input to the advection-diffusion equation from the *Flow Rate Attenuation* solver block and outputs an updated protein concentration field which is passed to the *Constitutive Equation* block, both of which are covered in Chapter 4.

Chapter 4

Protein Aggregation and Rheology

4.1 Introduction

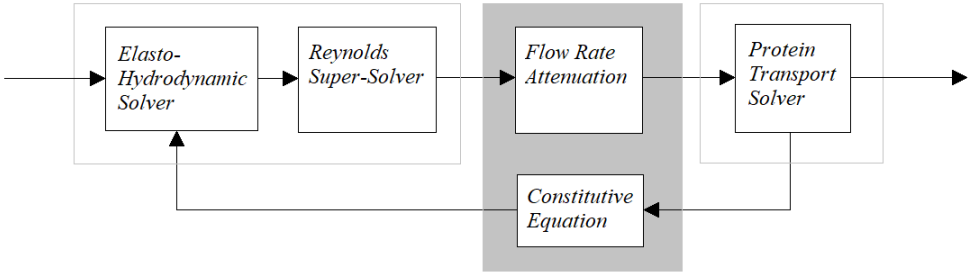


Figure 4.1: *Flow diagram showing overall PAL model schematic and the placement of the flow rate attenuation and constitutive equation blocks within it. The flow rate attenuation block receives volumetric fluid flow rate and outputs protein flow rates to be used in the scalar transport equation. Protein concentration profiles are then sent to the constitutive equation which calculates the viscosity field and passes this back to the EHL solver to begin the next time-step.*

This chapter describes the two solver blocks that deal with the rheology of the lubricating fluid. Figure 4.1 shows the location of these two blocks within the full PAL solver diagram. The flow rate attenuation block sits between the output of the RESS and the input of the scalar transport equations. This block takes the fluid flow rate and calculates an appropriate flow rate for the protein molecules as described by the concentration field. The second block contains the constitutive equation which receives the resulting protein concentration field from the scalar transport equation and calculates the viscosity field which is then used in the next time-step.

4.2 Protein movement attenuation

If the protein matter is modelled as moving freely with the fluid, the concentration of protein matter throughout the contact zone remains uniform over time. There are many factors that can alter the flow rate of protein molecules, with respect to the flow rate of fluid, including surface adsorption [103, 104], increased concentration causing hindrance by neighbouring particles [105, 106], and physical obstruction by decreasing gap size [107, 108].

The adsorption of protein molecules onto the lubrication surfaces will have an effect on the concentration of protein content at points throughout the domain. Adsorption is the process by which molecules adhere to the lubricated surfaces by means such as electrostatic interaction or hydrophobicity [104]. The complex nature by which tribochemistry influences lubrication is beyond the scope of this thesis which instead aims to model PAL by a singular modified flow rate approach and to ascertain whether this approach is sufficient to replicate the behaviour of PAL.

To do this, a scaling factor, ϕ is introduced such that the protein flow rate is related to the fluid flow rate such that

$$\mathbf{Q} = \phi \mathbf{Q}_\infty. \tag{4.2.1}$$

and resolved in the defined x- and y-directions as

$$Q_x = \phi_x Q_{x,\infty} \tag{4.2.2}$$

$$Q_y = \phi_y Q_{y,\infty} \tag{4.2.3}$$

Here, there is a change in notation such that Q_∞ denotes the fluid flow rate as calculated from the results of the EHL and RESS, and Q denotes the protein flow rates that are to be used in the scalar transport equation. The scaling factor, ϕ, is a function that can be used to capture the protein flow rate behaviour with respect to multiple different underlying variables.

The variables that the function ϕ depends upon could include – but is not limited to – the concentration of protein matter, C, the height of the lubricating gap, H, and the gradient of the height, resolved as $\partial H/\partial X$ and $\partial H/\partial Y$. These variables make intuitive sense as potential factors; increased concentration can cause overcrowding of suspended macromolecules and in turn reduce the flow rate. This is included in Stokesian dynamics simulations whereby the presence of neighbouring molecules affect the drag experienced by others [86]. At points in the domain where the fluid

film is thin enough, protein flow rate will differ from that of the fluid as the gap becomes too small for the macromolecules to flow freely and unobstructed [108]. It is also intuitive that converging gaps may attenuate the flow of protein more-so than a diverging gap as would be experienced as the matter close to the centreline flows outwards in the y-direction. The inclusion of a direction dependant term such as the height gradient – or indeed any other directional variable, such as the sliding speed or shear rate – would lead to different scaling to the flow rates in the x- and y-direction as the functions ϕ_x and ϕ_y would differ.

For this first PAL model, it is desirable to keep the function as simple as possible while still capturing the fundamental behaviour of protein aggregation. Including multiple variables introduces many weighting coefficients in the function, ϕ, which require calibrating. Instead, the hypothesis of this thesis is that the geometry of the problem, namely the film height, is the single most influential factor in the attenuation of protein flow rate and as such a scaling factor dependant on this variable alone is used as the focus of this study into modelling the behaviour of protein aggregation lubrication. The film height is not dependant on the direction of the flow rate and as such the functions, ϕ_x and ϕ_y become the same, resulting in the relations

$$Q_x = \phi(H) Q_{x,\infty} \tag{4.2.4}$$

$$Q_y = \phi(H) Q_{y,\infty}. \tag{4.2.5}$$

4.3 Proposed scaling factor

The nature by which the small gap hinders protein movement lies within the shape of the function, ϕ. It is clear that when the gap becomes smaller than individual unaggregated protein molecules, no protein matter can flow with the fluid, i.e

$$\phi(H) = 0, \quad \text{when} \quad H < H_p \tag{4.3.1}$$

where H_p is used to donate the dimensionless length scale of individual protein molecules. The Stokes radii of Albumin and Globulin are around 3.5 and 5.4 nm respectively [109, 110], giving a good indicator of molecule size. The Stokes radius is defined as the radius of a hard sphere that diffuses at the same rate as the solute [111]. Non-dimensionalising these length scales with the Hertzian deformation height, h_h, for this PAL model gives dimensionless values $H_{p,Globulin} = 0.0156$ and $H_{p,Albumin} = 0.0101$. For the purposes of simplicity, it is assumed that these lengths are sufficiently small as to be treated as zero with little effect to the filter function, ϕ. The validity of this assumption is examined in Chapter 5.

It is also clear that as the film height becomes large enough, the protein molecules and even large aggregate clumps of protein matter should be able to flow freely with the fluid, i.e

$$\phi(H) \to 1, \quad \text{as} \quad H \to \infty. \tag{4.3.2}$$

Between these limits the function should increase monotonically as there should be no instance of a smaller film height allowing protein to move more freely than a larger film height. The exact behaviour and shape of the function, however, depends on the distribution of protein aggregate size within the fluid, which is unknown. In lieu of modelling protein interactions and the subsequent build up and breakdown of aggregate networks, which would require much computational expense and knowledge of the particle initial conditions, a reasonable estimate of a likely size distribution shape can be used.

Particle size distributions for suspensions in fluids are commonly modelled using log-normal or Rosin–Rammler (also known as Weibull) distributions [112]. Another method is to use the hyperbolic tangent distribution family to model the cumulative distribution of particle size as both log-normal and Rosin-Rammler distributions can be approximated well by this family of curves and thus it provides a convenient comparison to multiple different studies and is more general [113, 114]. The hyperbolic tangent family of curves is given by:

$$F(x) = \begin{cases} \tanh^m(ax+b)^n, & \text{for } ax+b<0 \\ 0, & \text{otherwise} \end{cases} \tag{4.3.3}$$

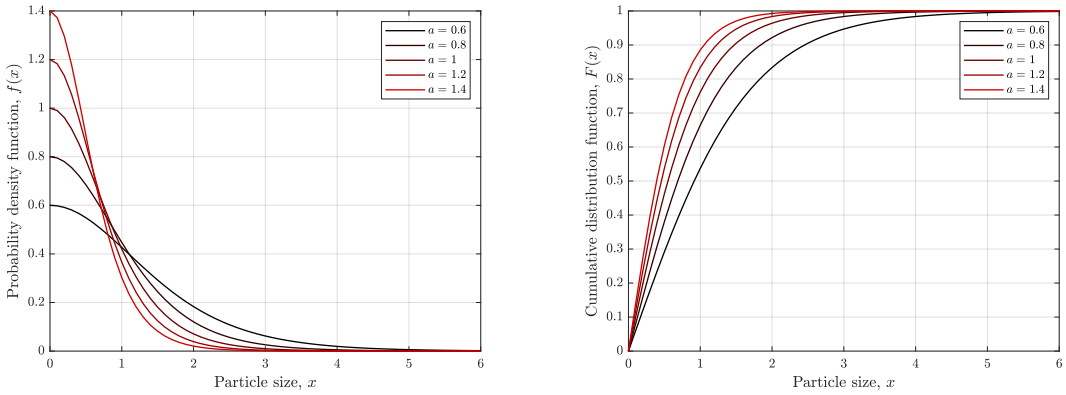
The parameters, a, and, b, govern the range over which the particle size is distributed and the parameters, m, and, n, govern the location and magnitude of inflection points of the probability distribution curve. It is an assumption that the number of aggregate clumps at any given size decreases as that size becomes larger. This is shown to be the case for human serum albumin (HSA) samples with the largest aggregate particles being of the 50–100 μm scale [115]. This would suggest that a cumulative curve of the hyperbolic tangent family with values of m and n close to 1 would be an appropriate approximation of distribution for this first PAL model. For simplicity in this study, these parameters are fixed as $m = n = 1$, however further studies modelling PAL could allow these values to be discovered during the calibration process of Chapter 5.

Further simplifications can be made by examining the effects of the parameters, a, and b. These parameters govern the 'significant size interval', that is the range of sizes over which the majority of particles lie and can be related to the minimum and maximum particle size [113] (if known) as

$$a = \frac{1}{x_{\max} - x_{\min}}, \qquad b = -\frac{x_{\min}}{x_{\max} - x_{\min}}. \tag{4.3.4}$$

It has been discussed in §4.2 that the minimum length scale of aggregate molecules is of the order of the Stokes' radii of albumin and globulin and are of such a size as can be assumed zero. This, in turn, results in a value of $b = 0$. Without knowledge of the maximum particle size, parameter, a, is free to be calibrated.

The resulting modelled particle size distributions can be seen in Figure 4.2, where the cumulative distribution functions are given by the hyperbolic tangent function family of Equation 4.3.3 with parameters, $b = 0$, and $m = n = 1$, and with varying values of parameter, a. Also shown is the associated probability density functions. If it is the assumption that protein aggregate size is distributed in a manner similar to those functions, $f(x)$, then it follows that the flow rate attenuation function, $\phi(H)$, should be of a form similar to those functions, $F(x)$, as this simply indicates the proportion of protein aggregates smaller than the film height at that point. Any aggregate molecules larger than the film height will be obstructed.



(a) (b)

Figure 4.2: *Particle size distribution models showing. Plot (a) shows the modelled probability density function of particle size. Plot(b) shows the modelled cumulative distribution function. Both plots show a range of values of parameter, a.*

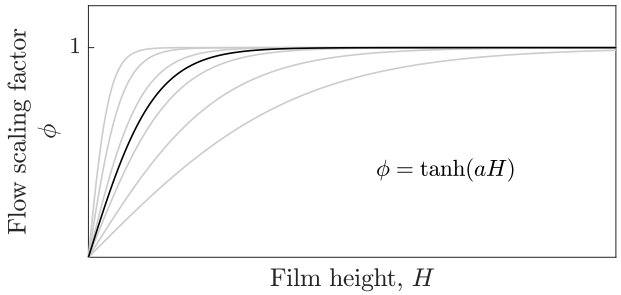


Figure 4.3: *Proposed scaling factor function for limiting flow rate of protein transportation. The gradient parameter, a, can be used for tuning the function – various values of parameter, a, shown in grey.*

As such the proposed scaling factor function is the modelled cumulative particle size distribution of the form

$$\phi = \tanh(aH) \tag{4.3.5}$$

the gradient of which can be tuned via the free parameter, a, as depicted in Figure 4.3.

4.4 Scalar transport with attenuated flow rates

The parameter a is subject to a search to determine which value gives the closest approximation to experiment in Chapter 5, however we can examine the result of flow attenuation on the concentration of protein matter across the lubrication region.

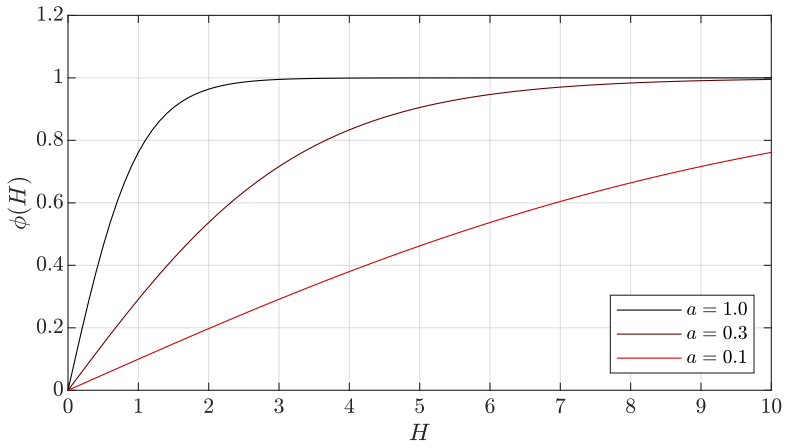


Figure 4.4: *Varying gradient parameter showing effects on the flow rate attenuation function* $\phi = \tanh(aH)$.

Figure 4.4 shows three different gradient parameters, $a = 1.0, 0.3$ and 0.1 and the effect that has on the resulting flow filter function ϕ. Using the central differenced implicit Euler method for the scalar transport equation a single time-step of $\Delta T = 0.1$ can be solved to view the effect the gradient of the attenuation function has on the impediment of protein matter. Decreasing the gradient results in the accumulation of protein matter further upstream, and for these simulations the steady solution, with the parameters from Table 1.2, is solved over a domain of $-8 \leqslant X \leqslant 2, -5 \leqslant Y \leqslant 5$ with a grid density of $N = 2^8$. This grid density is the same as previously found mesh independent and the domain has not been stretched in the x-direction but merely shifted such that the steady solution results in key values $H_{\text{cen}}, H_{\text{min}}$ and P_{max} that negligibly differ.

Figure 4.5 show the concentration fields after a single time-step for these three values of parameter a. Where the gradient is highest, the protein matter accumulates in a very local region at the inlet of the contact zone. As protein matter is also slower moving in the contact zone, the region directly downstream is starved. This is most noticeable in two large regions where if the cavitation condition had not been enforced, matter would be flooding in from the sides. Flow rates in this region downstream of the cavitation line are not accurate but are also outside the region

of interest. As the gradient parameter decreases, the flow rate is more greatly attenuated and the protein accumulates further upstream. As the slope of the filter function is less severe, the concentration peak is much smaller but vastly more spread out across the domain.

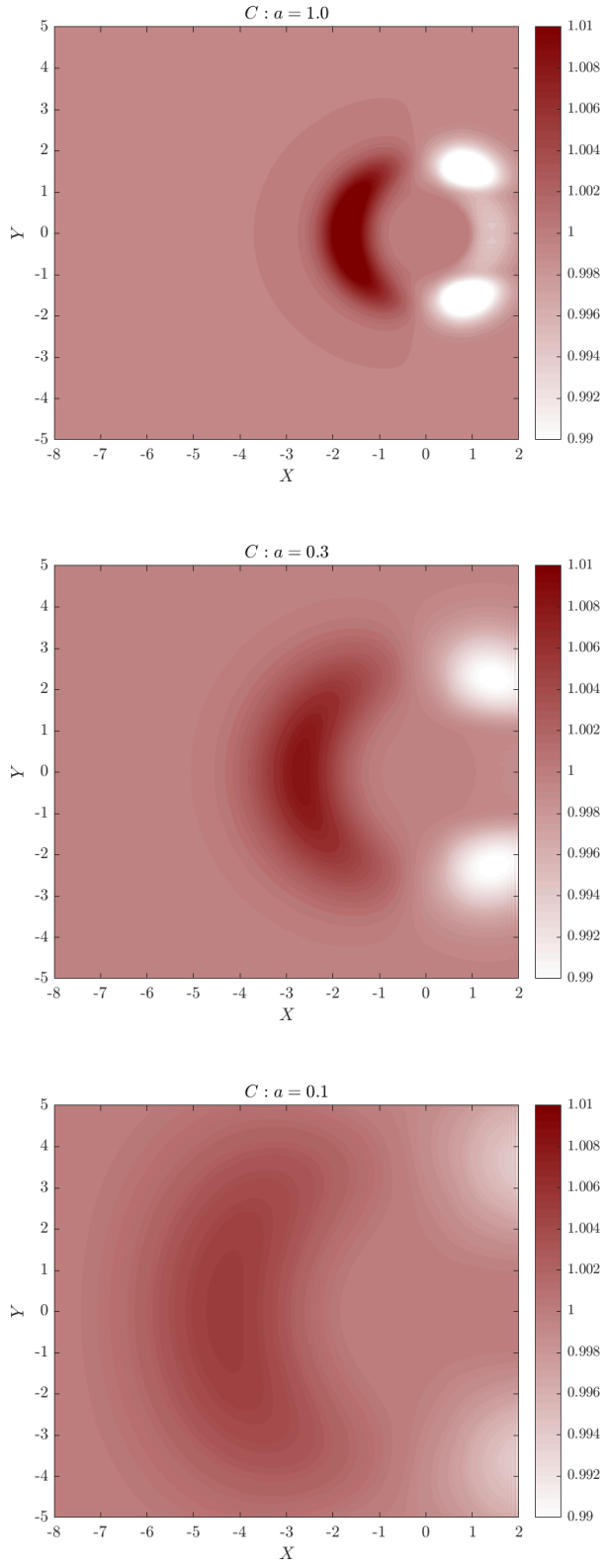


Figure 4.5: *Concentration profile after a time-step of* $\Delta T = 0.1$ *and a Péclet number of* $\mathrm{Pe} = 10^4$ *for varying values of the gradient parameter,* a*. The film height and flow rate are of the initial steady solution.*

4.5 Diffusion

The Péclet number is assumed to be in the order of 10^4 – 10^5 based on available studies of the diffusion constant of synovial proteins, albumin and globulin [102, 116, 117]. The studies show that the diffusion constant and thus the Péclet number are concentration-dependent.

The study by Wakeham et al. [102] shows that the diffusion constant for albumin decreases as concentration increases ranging from $D = 4.4 \times 10^{-11}$ m^2/s at a concentration of 21.4 mg/ml down to a diffusion constant of $D = 2.4 \times 10^{-11}$ m^2/s at a concentration of 163 mg/ml, which is over nine times the initial concentration of 18 mg/ml from experiments by Myant and Cann [39]. These values of diffusion constant, D, result in Péclet numbers of $\mathrm{Pe} = 3.7 \times 10^4$ and 6.8×10^4 respectively using Equation 3.3.4.

A study by Grimaldo et al. [116] shows similar behaviour for the diffusion constant of globulin with diffusion constant in the dilute limit of $D = 3.3 \times 10^{-11}$ m^2/s ($\mathrm{Pe} = 4.9 \times 10^4$), decreasing as the volume fraction of globulin increases. The study shows that the diffusion constant is roughly halved as the volume fraction reaches 0.1. Using the specific volume of globulin $\theta = 0.739$ ml/g [116] this equates to a concentration of 150 mg/ml (8.4 times the initial concentration, c_0) and results in a Péclet number of $\mathrm{Pe} = 9.8 \times 10^4$.

Péclet numbers in the region of 10^4 – 10^5 show that advection dominates the scalar transport equation and changes to the diffusion constant may have a negligible effect on the movement of protein matter where the diffusion plays such a small role. Figure 4.6 shows the concentration field after a single time-step for varying Péclet number using a gradient parameter of $a = 0.3$. There is very little to distinguish the resulting fields and it is assumed that if the Péclet number is sufficiently large, the effect of concentration-dependent diffusion can be assumed negligible. Over longer periods of time, the relative value of the Péclet number could have a more pronounced effect and as such the validity of this assumption is examined in Chapter 5.

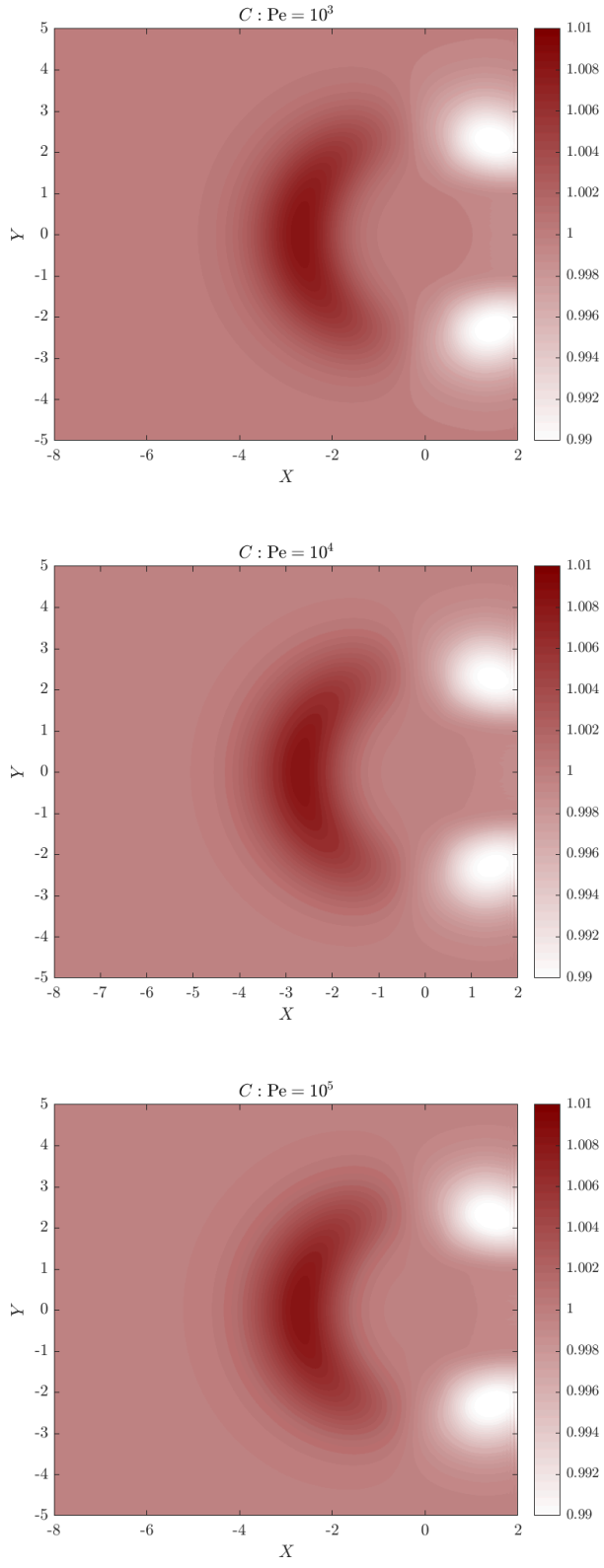


Figure 4.6: *Concentration profile after a time-step of* $\Delta T = 0.1$ *and gradient parameter,* $a = 0.3$*, for varying values of the Péclet number. The film height and flow rate are of the initial steady solution.*

4.6 Constitutive equation

As has been discussed in §1.3.1, the viscosity should increase exponentially with increasing concentration of protein and therefore should be of the form

$$\eta = \eta_{\mathrm{pf}} e^{\beta(c/c_0)} \tag{4.6.1}$$

where η_{pf} is the protein-free viscosity i.e. at zero concentration and c_0 is the initial concentration at zero time. As the concentration does not change over time far from the contact zone, c_0 is the fixed concentration upstream.

Knowing the initial condition, $\eta = \eta_0$, $c = c_0$, leads to the following relation

$$\beta = ln(\eta_0/\eta_{\mathrm{pf}}). \tag{4.6.2}$$

Substituting back into Equation 4.6.1 gives

$$\eta = \eta_{\mathrm{pf}} \left(\frac{\eta_0}{\eta_{\mathrm{pf}}} \right)^C \tag{4.6.3}$$

such that when non-dimensionalised, the constitutive equation becomes

$$\tilde{\eta} = \left(\frac{1}{\hat{\eta}} \right)^{(C-1)} \qquad \hat{\eta} = \eta_{\mathrm{pf}}/\eta_0. \tag{4.6.4}$$

Here, $\hat{\eta}$, is a dimensionless viscosity parameter, normalised in the same manner as $\tilde{\eta}$ using the initial reference viscosity, η_0. In Chapter 2 an initial reference viscosity of $\eta_0 = 0.075$ Pa.s was shown to give good agreement with the initial central film thickness measurements of the experiment by Myant and Cann [71], in which the post-scratch central film thickness just before the inlet aggregate starts to accumulate, is around 20 nm. The value of $\hat{\eta}$ is subject to a search to examine which value best replicates the results of experiment.

4.7 Summary

In this chapter, the two solver blocks that deal with the rheology of the lubricating fluid have been developed. These are namely the *Flow Rate Attenuation* and *Constitutive Equation* blocks. The former of these blocks takes as input the fluid flow rate from the *EHL Solver* and *RESS* (Chapter 2) and uses a simple scaling function to deduce the protein flow rate, which is then passed to the *Protein Transport Solver* block (Chapter 3). The scaling function, ϕ is dependant on lubricating film height and has the form of an approximated cumulative distribution function of protein molecule size. This allows for the modelling of protein obstruction by the geometry of the lubricated surfaces and results in the localised accumulation of protein concentration at the inlet of the contact zone. The behaviour of the scaling function is adjusted by the gradient parameter, a.

The second block discussed in this chapter is a constitutive equation that takes as input the updated protein concentration field and derives the local viscosity of the fluid. The relation between protein concentration and viscosity has been found in previous literature to be exponential in nature and as such the constitutive equation in this study is of this form whereby the severity of this relation is governed by the dimensionless viscosity parameter, $\hat{\eta}$

The two parameters, a, and $\hat{\eta}$, introduced within this chapter underpin the nature of the full protein aggregation lubrication model and a parameter search to identify the values that give transient central film thickness results that best match the experiment by Myant and Cann [71] is needed to calibrate the model. This calibration is conducted in Chapter 5.

Chapter 5

Transient Protein Aggregation Lubrication Model

5.1 Introduction

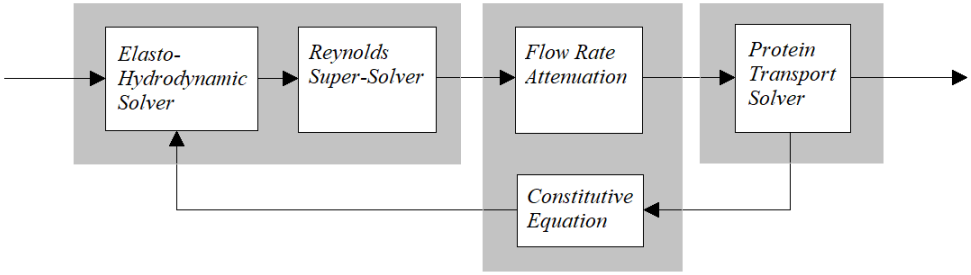


Figure 5.1: *Flow diagram showing overall PAL model schematic including all previous blocks. One full circuit around the diagram represents one time-step and this procedure is repeated for transient results.*

In this chapter, the previous flow diagram stages are combined to form the transient protein aggregation lubrication solver as shown in Figure 5.1. The parameters introduced in Chapter 4, namely the flow attenuation function gradient parameter, a, and the non-dimensionalised, protein-free viscosity, $\hat{\eta}$, are subject to a parameter search to identify values that result in simulations that best match the central film thickness of experiment. These values are found and thus the model is deemed to be calibrated for the operating conditions found in experiments by Myant and Cann [71].

The calibrated transient model is then analysed for time-step and mesh independence, and refined as necessary. Full details of this process can be found in Appendix C. Finally, the results of the simulation are explored, including the concentration build up, the shape of the lubricated surfaces and the development of the pressure profile, and compared to those of the experiment.

5.2 Parameter search

A series of simulations were run spanning a range of values for the two free parameters – a, the hyperbolic tangent gradient of Eq. 4.3.5 and $\hat{\eta}$, the ratio of protein free viscosity to initial viscosity that defines the concentration relation, Eq. 4.6.4. The Péclet number is assumed constant and fixed at $Pe = 10^4$ and the time-step is set to a value of $\Delta T = 0.1$. This choice of time-step is examined further in section § 5.3. The ranges are summarised below in Table 5.1 and give a total of 400 initial simulations.

Dimensionless Variable	**Range**	**Step**
$\hat{\eta}$	0.0133 – 0.266	0.0133 (20 steps)
a	0.02 – 0.4	0.02 (20 steps)

Table 5.1: *Parameter range and step size for simulations. The unusual step size for $\hat{\eta}$ stems from the choice of range for dimensional variable, η_{pf}, being 0.001 – 0.02 Pas.s with a step size of 0.001 Pa.s*

As was shown in Figure 4.5, for lower values of the gradient parameter, a, protein accumulation starts far upstream of the contact zone and a larger domain is needed to simulate the transport equations. Due to the increased computational cost, it is not desirable to increase the domain size of the EHL solver or protein transport solver while keeping the same grid density. Moreover, the EHL solver is known to be mesh independent and increasing the domain by using a coarser mesh is also not desirable in order to maintain accuracy.

To reach the requirements of a sufficiently dense EHL domain and a sufficiently large transport domain, the latter is enlarged to cover $-10 \leqslant X \leqslant 10, -10 \leqslant Y \leqslant 10$ while keeping the same grid number $N = 2^8$. Figure 5.2 shows an example of this two grid system for a grid number of $N = 2^4$. This results in a transport grid that is only half as dense as the computational EHL grid. The film height solutions from the EHL solver are therefore sampled in the domain $-5 \leqslant X \leqslant 5, -5 \leqslant Y \leqslant 5$ and outside of this region the film heights are assumed to be undeformed. The average difference between the deformed and undeformed film thickness at the boundary of the EHL solver is less than 0.51%. The Reynolds equation super-solver is run on the enlarged grid allowing for conservation of mass over the entire transport domain. The validity of this approach is further explored in § 5.3 for the calibrated parameters that result from the search.

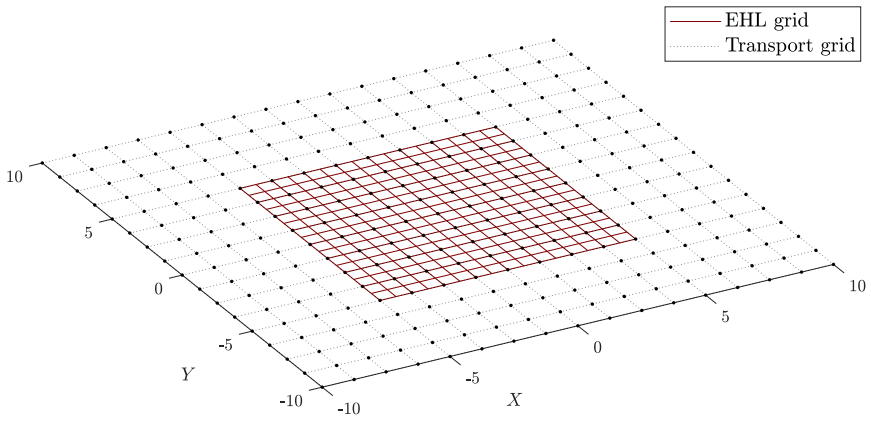


Figure 5.2: *Example of an enlarged transport grid for a mesh number, $N = 2^4$, showing location of grid-points for both the EHL grid and the transport grid.*

5.2.1 Initial parameter search results

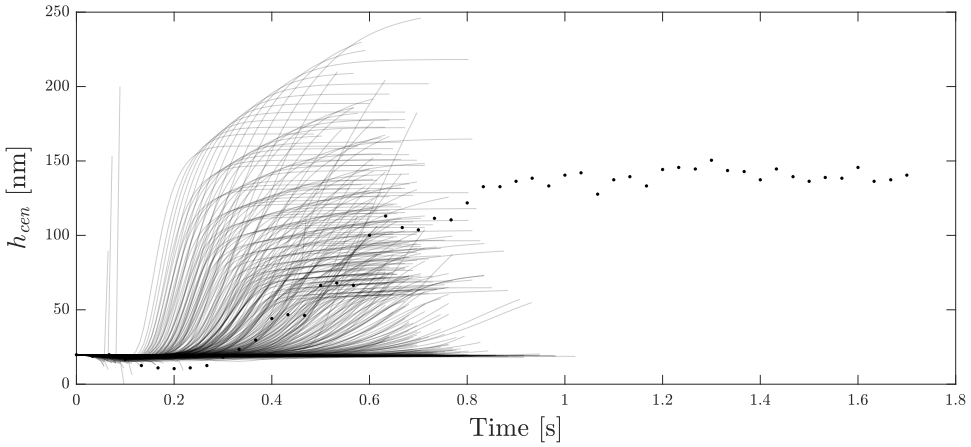


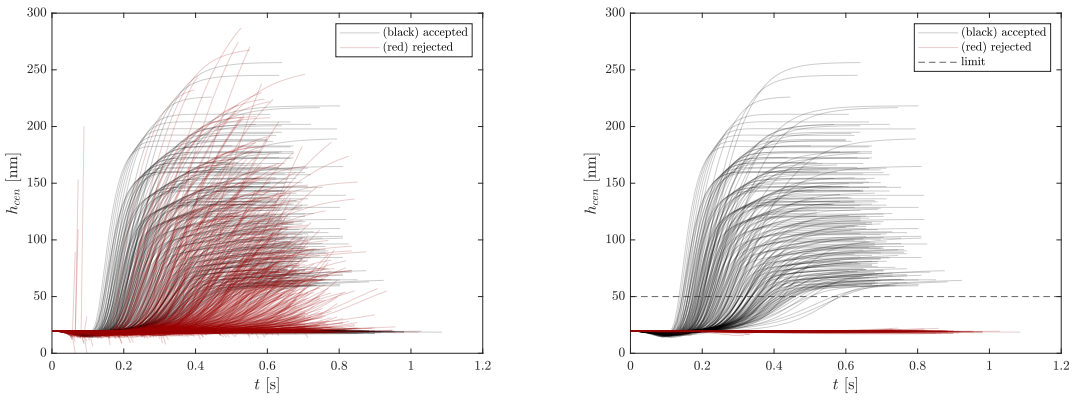
Figure 5.3: *Initial parameter search showing range of simulation solutions (solid grey) as compared to experimental results (black points).*

The initial parameter search simulations to establish optimal model parameters were run for 72 hours before being terminated. This period proved adequate for determining the behaviour of fluid film development with respect to the parameter space. The initial spread of film thickness curves in Figure 5.3 is wide and in order to evaluate which curves best approximate the experimental results two factors were used, the first being the stable film height that the simulations approach – this film height plateau can be seen in some but not all of the simulations in Figure 5.3. The second factor used is a measure of curve similarity, to examine which simulations best approximate the growth phase of the central film thickness. These

two evaluation methods were adequate to determine an optimal pair of parameters, $\hat{\eta}$ and a, whereby the simulation film thickness grows at a similar rate and plateaus at a similar point as experimental results.

5.2.2 Plateau height

The results of experiment show that the film thickness reaches a stable value of 140 nm – based on the average of the last 20 data points. Multiple simulations have similar growth rates but plateau to different stable film thicknesses. Simulations were deemed to have plateaued by checking that the gradient has reduced to an acceptable level of 0.1 nm per time-step (12 nm/s). To ensure that only simulations that had stabilised after a significant growth phase were included, only simulations with a final film thickness of greater that 50 nm were selected; below this point, film heights were either still increasing or remained constant. This selection procedure can be seen in Figure 5.4.



(a) (b)

Figure 5.4: *Selection procedure to determine simulations that have useful information about final steady film thickness. Plot (a) shows the selection of simulation results that have reached a stable height plateau and plot (b) shows which of these simulations were rejected on the basis of not having sufficient film thickness growth of at least 50 nm.*

After this selection procedure, an equation for how the parameters affect this stable height is found simply by plotting the end points of the simulations that appear to have reached a stable height. Figure 5.5 shows the final film thicknesses and a surface of the form

$$z = c_1 + c_2 e^{(c_3\hat{\eta} + c_4 a)} \tag{5.2.1}$$

has been fitted using non-linear least squares regression. The resulting coefficients

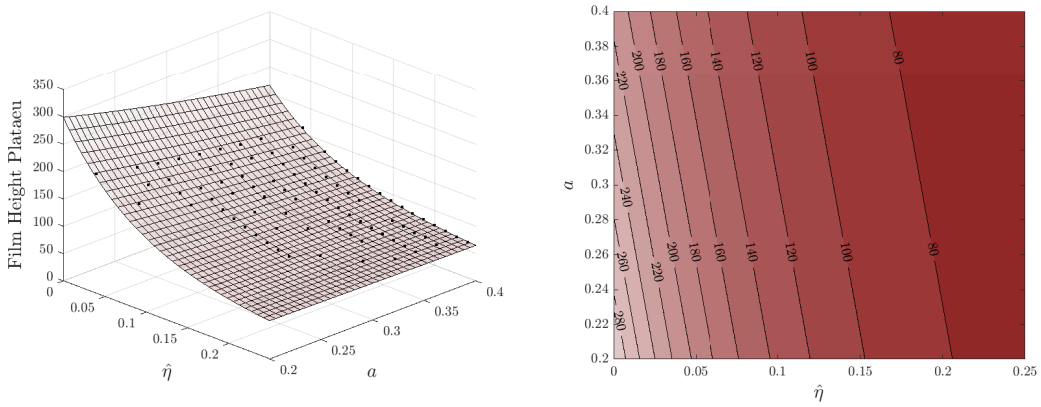


Figure 5.5: *(Left) Final film thickness of simulations that have reached a steady plateau and the best fit surface resulting from a non-linear least squares regression. (Right) Contours of constant film height for this surface.*

and fit parameters can be seen in Table 5.2

	$\mathbf{c_1}$	$\mathbf{c_2}$	$\mathbf{c_3}$	$\mathbf{c_4}$	$\mathbf{R^2}$	**Adjusted $\mathbf{R^2}$**
Value	54.88	372.5	-11.04	-2.114	0.9980	0.9979

Table 5.2: *Coefficients and goodness of fit parameters for final film height response surface*

Figure 5.5 also shows the fitted function contours of constant height, which form straight lines. For the desired stable film thickness of 140 nm this line has the form

$$\begin{aligned} a &= -\frac{c_3}{c_4}\hat{\eta} + \frac{1}{c_4}\ln\left(\frac{140 - c_1}{c_2}\right) \\ a &= -5.22\hat{\eta} + 0.698 \end{aligned} \tag{5.2.2}$$

5.2.3 Curve similarity

To quantify the similarity of the initial delay and subsequent growth rate of the lubricating film, the sum of squared residuals is calculated. The sum of squared residuals (SSR) is a measure of curve similarity most often used in least squares regression whereby the sum is minimised to obtain a good model fit to data.

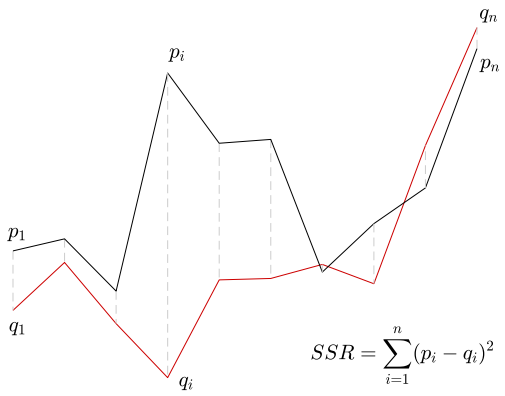


Figure 5.6: *Definition of the sum of squared residuals (SSR) between two curves, P (black) and Q (red) whereby values along the curves at location i are labelled p_i and q_i respectively.*

The SSR between two curves, P and Q is calculated as

$$SSR = \sum_{i=1}^{n}(p_i - q_i)^2 \tag{5.2.3}$$

whereby values along the curves at location i are labelled p_i and q_i respectively. A schematic representation of this algorithm can be seen in Figure 5.6 and measures intuitively the distance between the two curves at each location squaring the residual to account for negative values if the curves cross.

To calculate the SSR between the simulations and experiment, both must have the same sample rate. The simulations are run with a dimensionless time-step of 0.1 (which corresponds to 8.1064×10^{-4} s) for 2000 time-steps, however results are stored only every 10 steps such that the sample rate of the simulation results is once every 8.1064 ms with 200 data points excluding the initial solution. The experimental results are interpolated to this same sample rate, so that the SSR can be calculated.

To compare the individual simulations it is desirable to sum over the same number of samples, n. By comparing the simulation length of all 400 simulations in Figure 5.7 it can be seen that the majority of simulations terminated between 1/3 and 2/3

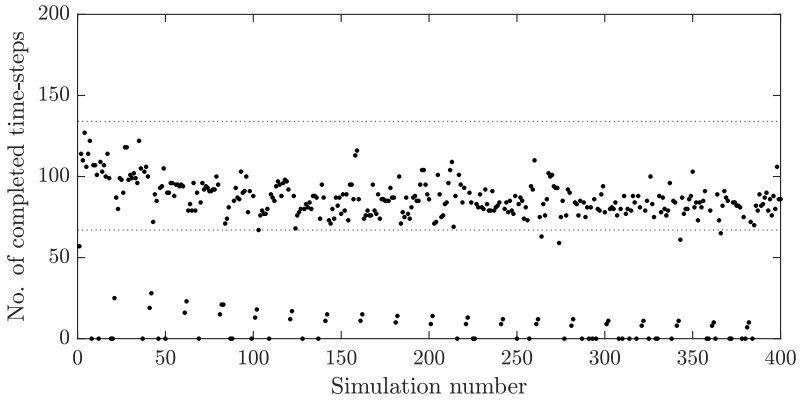


Figure 5.7: *Comparison of simulation length across all 400 simulations. The majority of simulations terminated between 1/3 and 2/3 of the total 200 recorded samples.*

of the total 200 recorded samples. There is a distinct group of simulations that do not reach this threshold and it is likely that these simulations became unstable and failed. The SSR is therefore calculated over the first 67 samples equating to the threshold at 1/3 of total simulation time (0.53 seconds of experiment time). This is an adequate length to analyse the initial growth behaviour of the central film thickness. Simulations that did not reach this threshold were rejected.

Figure 5.8 shows the resulting contour plots of the sum of squared residuals of each simulation in the parameter space as compared to experiment. For clarity of the contour plot, the square root of the SSR is plotted. The plot does not have an apparent minimal point but is minimal along a line – this would not be the case if simulations reached the full 2000 time-steps as the curve similarity test would therefore have included the full film thickness development and final film height plateau and would be the only test necessary. Figure 5.8 highlights the minimal values along the rows and columns of the parameter grid and for simulations with parameters below $\hat{\eta} \approx 0.13$ and $a \approx 0.2$ fit a line with the equation $a = 1.5\hat{\eta}$.

The two equations that give optimal SSR and stable height plateau are thus

$$\begin{aligned} a &= 1.5\hat{\eta} \\ a &= -5.22\hat{\eta} + 0.698 \end{aligned} \tag{5.2.4}$$

and can be used to define the optimal parameters for the model. Solving this system of equations gives $\hat{\eta} = 0.104$ and $a = 0.156$. Figure 5.9 shows the full length transient film thickness for a simulation with these calibrated parameters. The resulting parameters led to central film thickness results that match experiments well in both final film height plateau and growth rate. A brief dip in the film

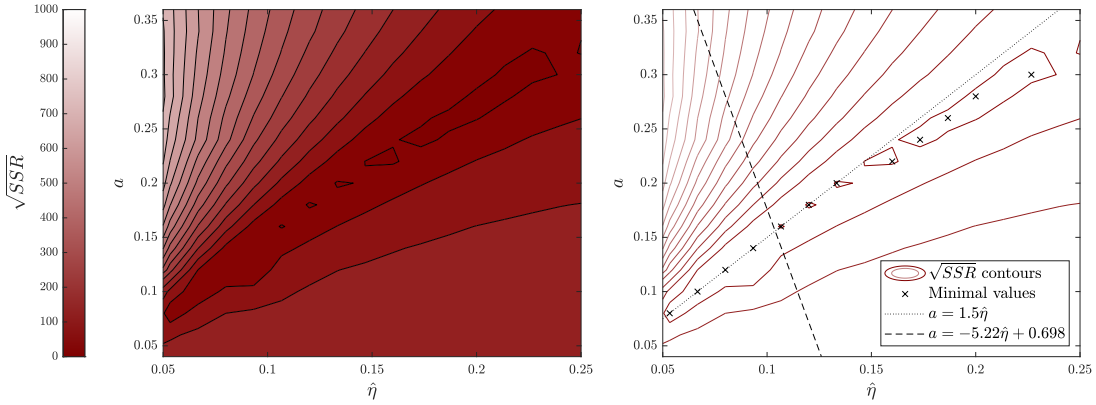


Figure 5.8: *(Left) Contour plot of the sum of squared residuals (SSR) over the parameter space. (Right) The same contours also showing the points which are minimal in both the x- and y-directions, the line that these points lie upon (dotted) and also the line upon which simulations lead to a plateau of 140 nm (dashed). The intersection of these two lines show the optimal parameters for matching experimental results.*

thickness within the first 0.2 s is replicated however it is not of the same magnitude. It can be seen in Figure 5.3 that none of the simulations within the parameter range considered express the extent of this initial thinning and it is most likely the case that this simplified model does not capture this phenomenon, which could potentially be because of the shear thinning behaviour or because of the disparity between the concentration in and out of the contact zone after the collapse of the stable film height.

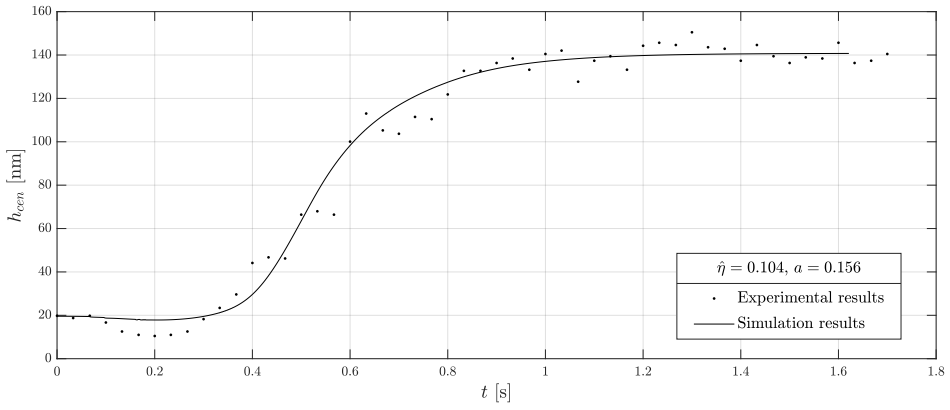


Figure 5.9: *Transient central film thickness plots for experiment and simulations showing increasing film thickness development over time. The calibrated parameters,* $\hat{\eta} = 0.104, a = 0.156$*, have been run for the design Péclet number,* $\mathrm{Pe} = 10^4$.

5.2.4 Péclet number

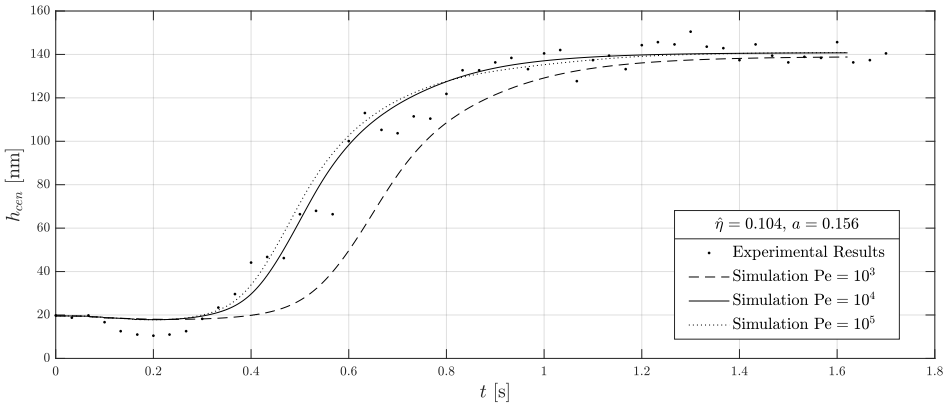


Figure 5.10: *Transient central film thickness plots for experiment and simulations showing increasing film thickness development over time. The calibrated parameters,* $\hat{\eta} = 0.104, a = 0.156$*, have been run for Péclet number,* $\mathrm{Pe} = 10^4$*, and also for Péclet numbers an order of magnitude higher and lower.*

The calibrated parameters were derived for $\mathrm{Pe} = 10^4$, however full simulations were also run at an order of magnitude above and below. Figure 5.10 shows that at lower Péclet numbers, these parameters no longer give a solution that agrees well with experiments, however, as the Péclet number increases, changes to the solution are minimal. It was discussed in § 4.5 that the known diffusion coefficients for albumin and globulin result in a concentration-dependent Péclet number in the range $\mathrm{Pe} = 10^4 - 10^5$. The results of Figure 5.10 indicate that the parameters give solutions that agree with experiment for the complete range of potential diffusion coefficients and the assumption that concentration dependency can be neglected is reasonable.

5.2.5 Flow attenuation function

It was assumed in § 4.2 that the sigmoid function that governs the flow attenuation of protein matter can start increasing at $H = 0$, where physically the function $\phi(H)$ should block the flow entirely below $H = H_p$, the size of an individual albumin or globulin macromolecule. Having determined that a gradient parameter value of $a = 0.156$ gives results close to those of experiments, further analysis was undertaken to confirm this assumption.

Figure 5.11 shows that the flow attenuation function approaches unity close to $H = 20$ which equates to a largest aggregate size of around 58 μm, in agreement with those values found by Richmond [115]. The lines of individual globulin and albumin

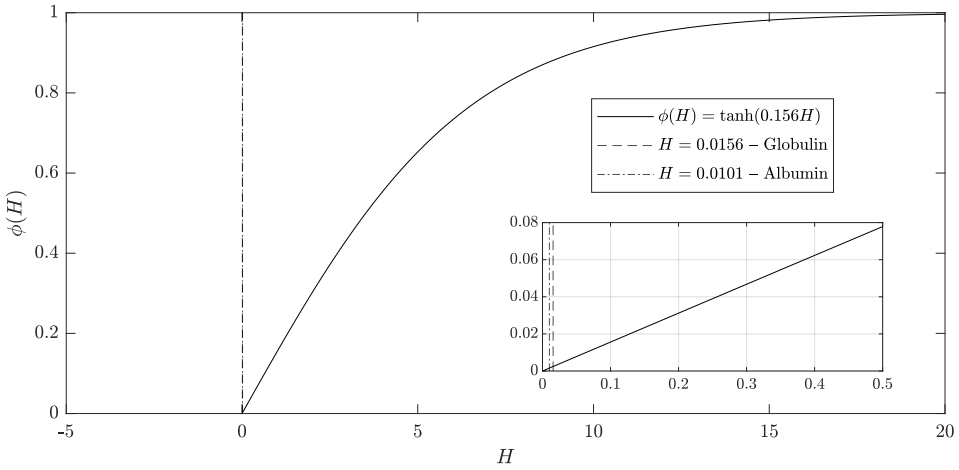


Figure 5.11: *Optimised flow attenuation function and scale of individual globulin and albumin molecules. Also shown (insert) is a magnified region close to zero, where the size of individual globulin and albumin become visibly distinct.*

molecules are plotted and shown to be close to zero at this scale. The assumption that $H_{p,Albumin}$ and $H_{p,Globulin}$ can be treated as zero is therefore considered valid for this value of gradient parameter, a.

5.3 Numerical accuracy and model refinement

There are several assumptions in the numerical method that have been made throughout the development of the full transient protein aggregation lubrication model, which can be more closely examined at the proposed calibrated parameter conditions. These include the assumption of sufficiently small time-step size, sufficient convergence criteria and sufficient mesh density. Full details of this examination can be found in Appendix C and the results suggest that for the calibrated PAL model, the solver has sufficiently small time-step size and sufficient convergence criteria.

It was also found, however, that for the chosen second order advection scheme, the mesh is not sufficiently dense to suppress the onset of spurious oscillations. It was found that either increasing the mesh density or employing a third order advection scheme were sufficient to suppress the spurious oscillations and did not affect the validity of the found optimal parameters, a and $\hat{\eta}$. Increasing the mesh density is achieved by increasing the grid number, N, or by decreasing the size of the domain. The former increases the computation time dramatically and the latter, although acceptable for this study, adds limitations to the model generally. Instead, it is chosen to increase the order of the advection scheme to a third order scheme as follows

$$\frac{Q_x}{H}\frac{\partial C}{\partial X} \approx \left(\frac{Q_x}{H}\right)_{i,j} \frac{2C_{i+1,j} + 3C_{i,j} - 6C_{i-1,j} + C_{i-2,j}}{6\Delta X} \tag{5.3.1}$$

which introduces only one extra diagonal in the solution matrix at the upstream location, $i-2$. The oscillations only occur in the x-direction and therefore the y-direction differencing can remain the same.

5.4 Results

Beyond the transient central film thickness, there are other results of interest that give insight into the nature of protein aggregation lubrication and the mechanisms that govern the increase in lubricating film thickness, namely the protein concentration build up at the inlet and the inlet length of the aggregate protein matter, the shape of the lubricated surfaces, and the development of the pressure profile in the contact zone.

5.4.1 Concentration and viscosity

Snapshots of the instantaneous concentration field are shown in Figure 5.12. Initially, protein matter aggregates at the inlet of the contact zone and the surface starts to deform noticeably in this region alone due to the increased viscosity and pressure. As the surfaces deform, the larger gap allows the protein aggregate to move slowly into the contact zone and deform the surfaces further downstream until the entire contact zone is flooded with high protein content fluid with a concentration over double that of the bovine calf serum that surrounds the contact region. The relative concentration reaches a maximum of $C = 2.58$, giving a relative viscosity peak of $\tilde{\eta} = 345$. This results in a dimensional peak protein concentration of around $c = 46.4$ g/l and peak viscosity of $\eta = 2.68$ Pa.s. The surface geometry itself shifts from an almost flat contact zone typical of elasto-hydrodynamic lubrication to a relatively steeper converging wedge.

This effect is due to the high viscosity moving the contact zone from the isoviscous-elastic regime towards the isoviscous-rigid regime. To quantify the change in regimes, work by Dowson and Hamrock [118], later revised by Esfahanian and Hamrock [119] mapped the approximate domains of lubrication regimes against a dimensionless elasticity parameter, g_E, and dimensionless viscosity parameter, g_V. The parameters are defined as

$$g_E = W^{3/8}/U^2, \qquad g_V = GW^3/U^2 \tag{5.4.1}$$

where W, U, and G, are the dimensionless load, speed and material parameters respectively as introduced by Dowson and Higginson. This non-dimensionalisation method is explored further in Appendix B, as is the relation between these parameters and other non-dimensionalisation methods covered previously.

Figure 5.13 shows the diagrammatic regime map of fluid lubrication regimes and an illustration of how increasing viscosity affects the behaviour of the lubricated

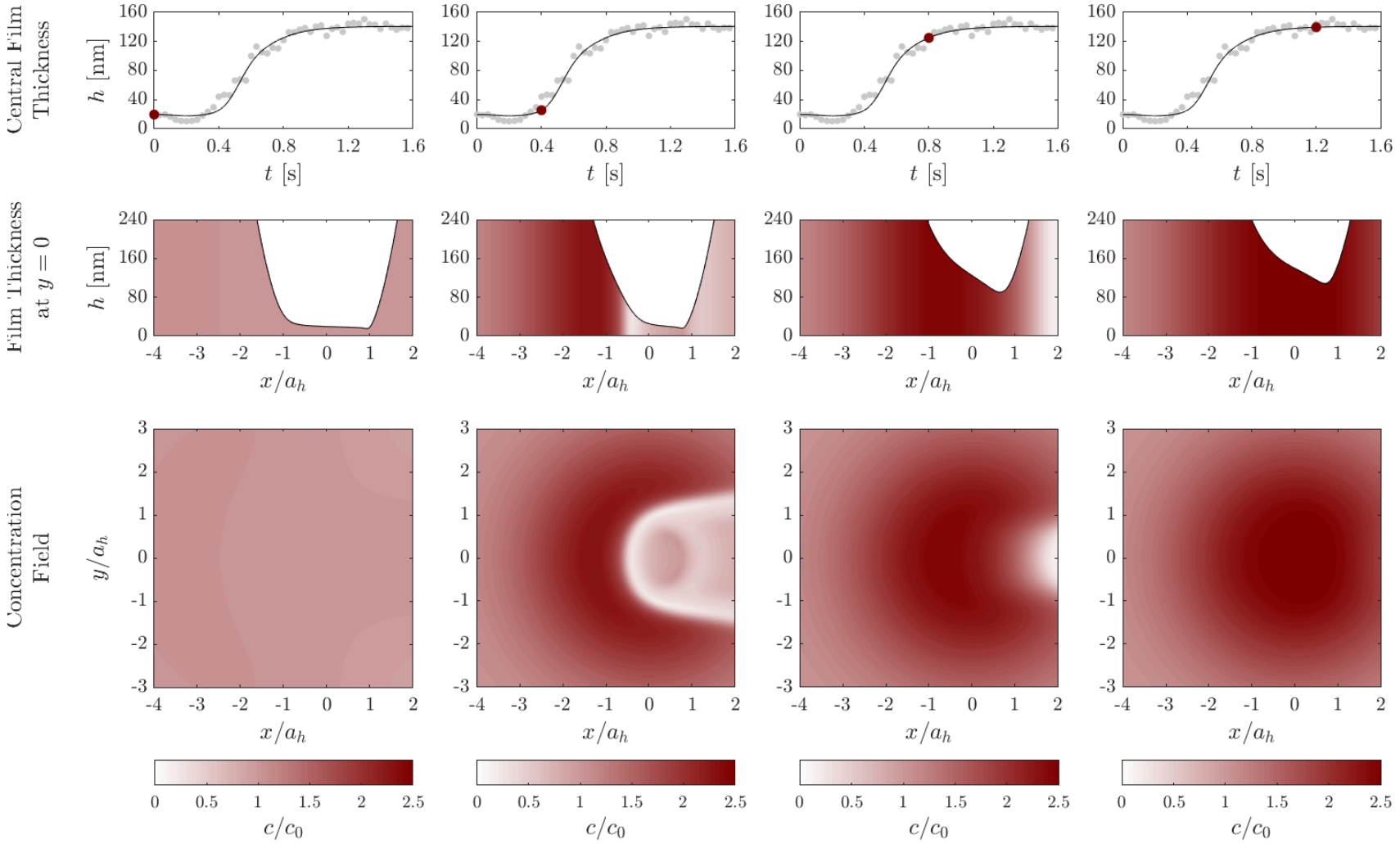


Figure 5.12: *Contour plots of protein concentration in the inlet and contact regions for the transient build up regime. The central film thickness plots (top) show the current point in time. The slices at $y = 0$ (middle) show film height development along with moving protein aggregate concentration and the top down view (bottom) shows the full concentration profile over the 2D computational domain.*

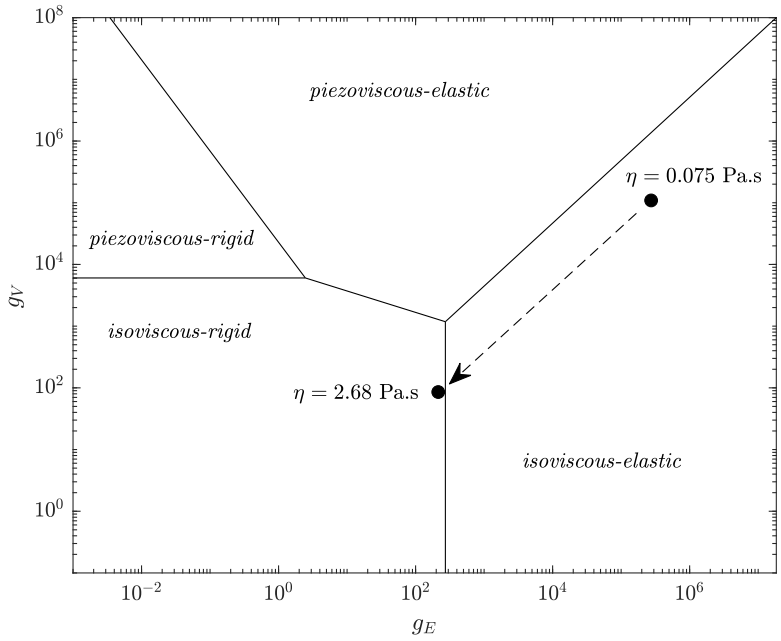


Figure 5.13: *Fluid film lubrication regime map indicating the effect of increasing viscosity on the behaviour of the contact zone of the protein aggregation lubrication simulation.*

contact. For the purposes of this figure, the pressure-viscosity coefficient of bovine calf serum is taken to be of the same order as water, being roughly $\alpha = 1$ GPa.s^{-1} [120]. Initially, the bulk viscosity throughout the contact zone is $\eta = 0.075$ Pa.s, which results in parameters g_E and g_V that are firmly in the isoviscous-elastic regime. The maximum viscosity reached in the PAL simulation was $\eta = 2.68$ Pa.s, and using this value the parameters g_E and g_V have moved into the isoviscous-rigid regime, whereby the contact behaves like a conventional hydrodynamic converging wedge.

5.4.2 Film height and inlet length

By using the interferometer images of the experiment by Myant and Cann [71], it is possible to compare the transient shape of the film height in the contact zone and also the size and shape of the inlet aggregate.

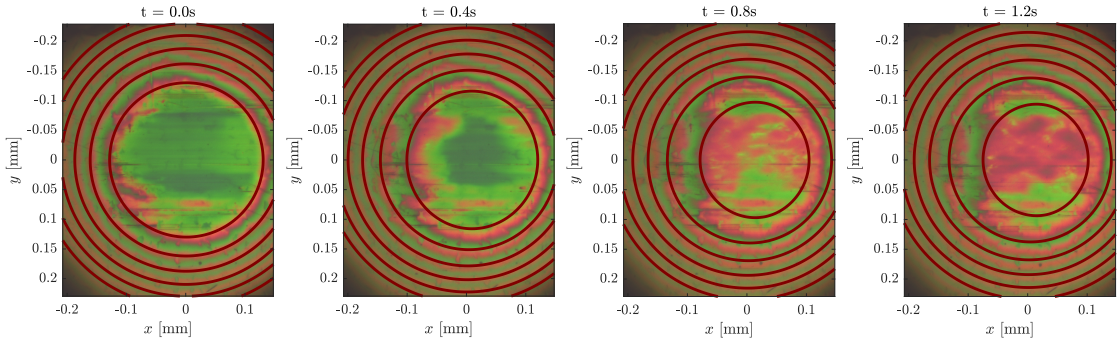


Figure 5.14: *Height contours of contact zone for simulation (solid red rings) shown overlaid on interferometer images of experiment by Myant and Cann [71]. The red rings show height contours of 225 nm matching the quarter wavelength of the interferometer image. Flow direction is from left to right.*

Comparison of height contours between simulation and experiment can be seen in Figure 5.14. The deformation of the contact zone shape follows similar behaviour whereby the deformation occurs initially only at the inlet side of the contact zone. Differences between simulation and experiment are visible from 0.8 s onwards as the inlet aggregate forms a channel through the contact zone in the experiment but not in the simulation. As seen in Figure 5.12 the protein concentration increases across the width of the contact in the modelled simulation.

The innermost ring, indicating 225 nm film thickness, continues to decrease throughout the simulation due to the continued separation of the two surfaces whereas the channel that can be observed in the experiment leads to an increased central film thickness without this continued global separation. As a result, the innermost ring of experimental images decreases in size less so than that of simulations, but there is a consistent agreement throughout between the location of the innermost contours at the inlet.

If the transient height is viewed along the line $y = 0$, the simulations agree well with

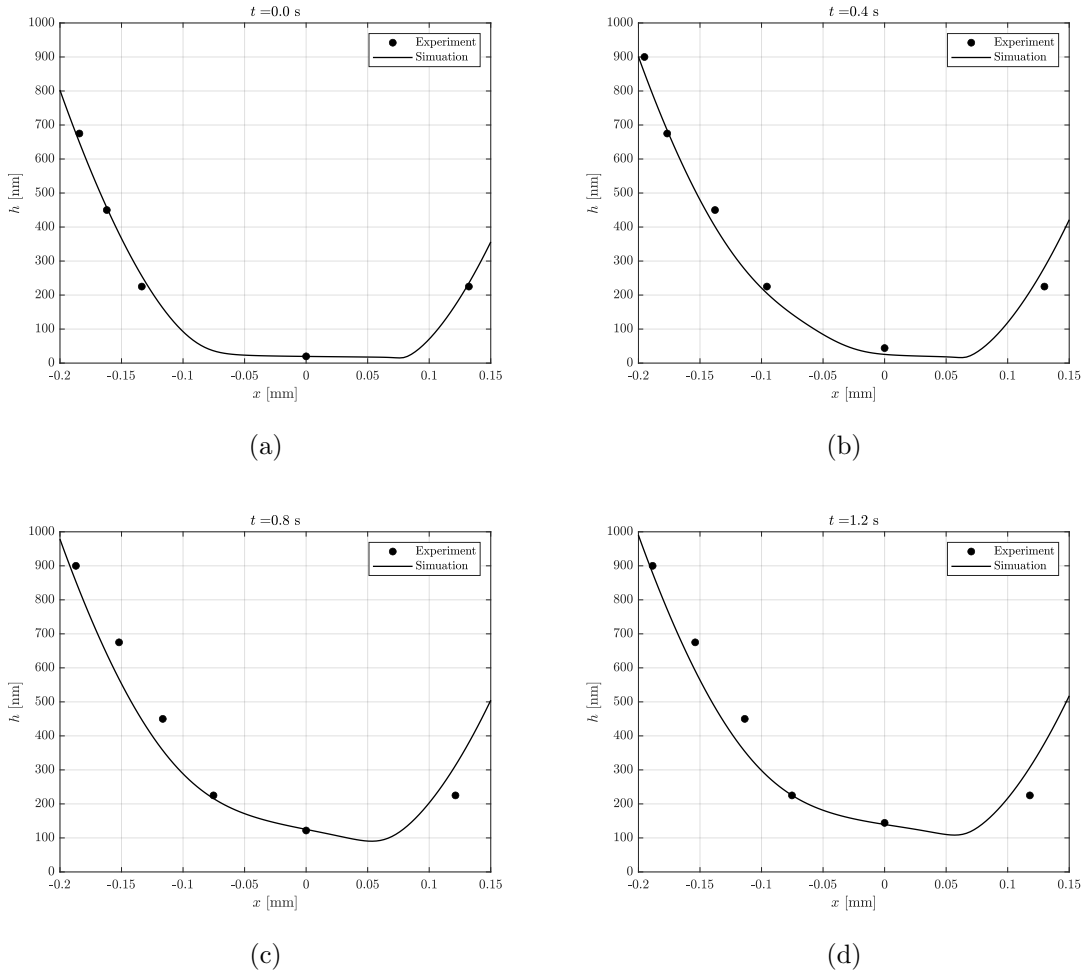


Figure 5.15: *Comparison of transient height profile along the line $y = 0$ between simulation and experimental interferogram. The experimental results consist of the height contour locations and the central film thickness measurements.*

experiment. Figure 5.15 shows the full simulation height profile plotted with the contour location from the experimental interferogram images. It can be seen that the behaviour whereby the contact zone deforms first at the inlet, while the central film thickness remains small, is well captured by the PAL model.

The formation of the high concentration channel can also be seen in Figure 5.16 whereby high concentration regions have been plotted overlaying interferometer images. The apparent regions of protein aggregate for experiments have been highlighted, and also shown are the regions for which protein concentration has doubled. The factor of two for concentration increase is arbitrary but shows comparable inlet lengths for visualisation. Unlike experiments, the simulation concentration shows a much broader accumulation across the y-direction, leading to a contact zone that is

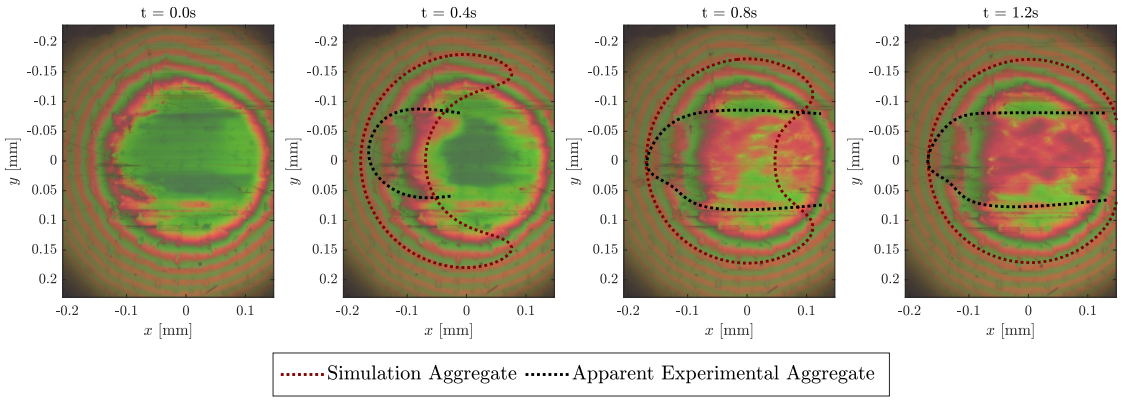
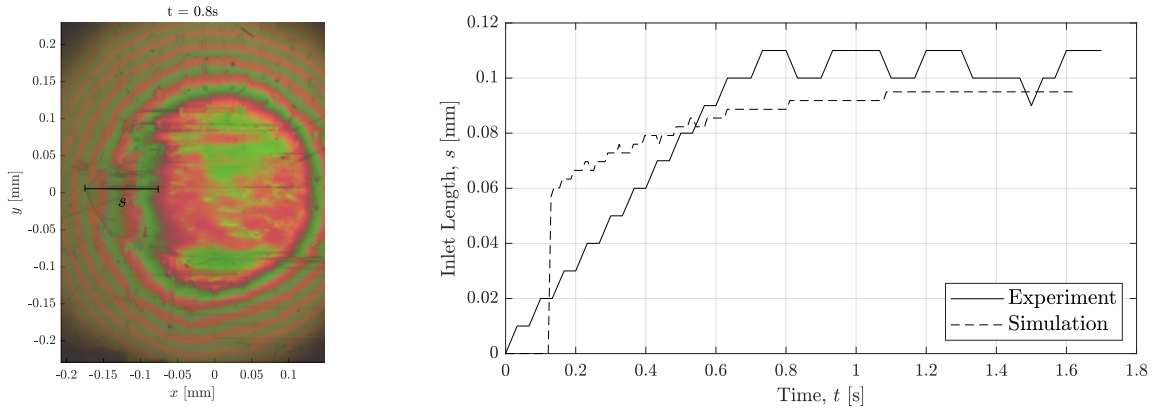


Figure 5.16: *Contours of $C = 2$ for simulation (dotted red) shown overlaid on interferometer images of experiment by Myant and Cann [71]. Also highlighted are the apparent protein aggregate regions of experimental images (black dotted). Flow direction is from left to right.*

eventually flooded with high protein fluid.

As well as the shape, it is possible to compare the transient development of the inlet length between the interferometer images and that of simulation. Figure 5.17a shows how the inlet length, s, is defined for interferometer images. For the simulation it is defined in a similar way as the distance between when the dimensionless protein concentration becomes $C = 2$ and the innermost height contour of $h = 225$ nm as seen in Figure 5.14. The selection of $C = 2$ is arbitrary, but offers good comparison when analysing the behaviour of the inlet length over time. It can be seen that the inlet develops linearly in experiments, reaching a steady value coinciding with the film height plateau. In simulation, however, the inlet length develops rapidly to begin with and grows only slowly thereafter. The initial jump is due to the time before a value of $C = 2$ is reached. This disparity in inlet length can also be seen in Figure 5.16 whereby the contours of simulation extend further upstream than that of experiments at time-step $t = 0.4$ s.

The behaviour that the simulations do not manage to capture is the localised nature of the aggregate build up. The flow rate attenuation function, ϕ, does not change over time, but physically the nature of the size distribution of protein matter particulates will indeed change as more macromolecules aggregate. This will lead to an increase of large particles at the inlet as more protein matter is accumulated here.



(a) (b)

Figure 5.17: *(a) Example of inlet length, s, as defined as the length between the apparent start of the aggregate matter to the inlet of the contact zone. (b) Comparison of measured inlet length in experiment to inlet length, s, of simulation using $C = 2$ as the starting point of inlet aggregate measurement.*

This effect could be modelled with a concentration-dependent function, $\phi(H, C)$, although the exact nature of aggregate size distribution is more complex than this and will likely also depend on the shearing behaviour of the fluid.

5.4.3 Pressure

Because the concentration initially aggregates exclusively in the inlet region, noticeable changes in viscosity and pressure occur in this region almost immediately. Figure 5.18 shows the transient nature of the pressure in the inlet and contact zone over the course of a second. Initially the pressure distribution is typical for a highly loaded elasto-hydrodynamically lubricated contact but soon develops a second peak that starts in the inlet region and moves through the contact zone as the aggregate does the same. The final pressure distribution again has a conventional EHL shape, albeit much broader with a lower peak, as is typical of a more viscous fluid. As the Hertzian pressure constant for this particular experiment is $p_h = 145$ MPa, the peak pressure drops from around 141 to 116 MPa over the course of the protein aggregation.

Also shown in Figure 5.18 are x-direction velocity profiles for the fluid in the inlet and contact regions, which show increased areas of backflow in inlet region once the viscosity increase takes place. The assumption of constant concentration across the thin film may need revisiting in future studies.

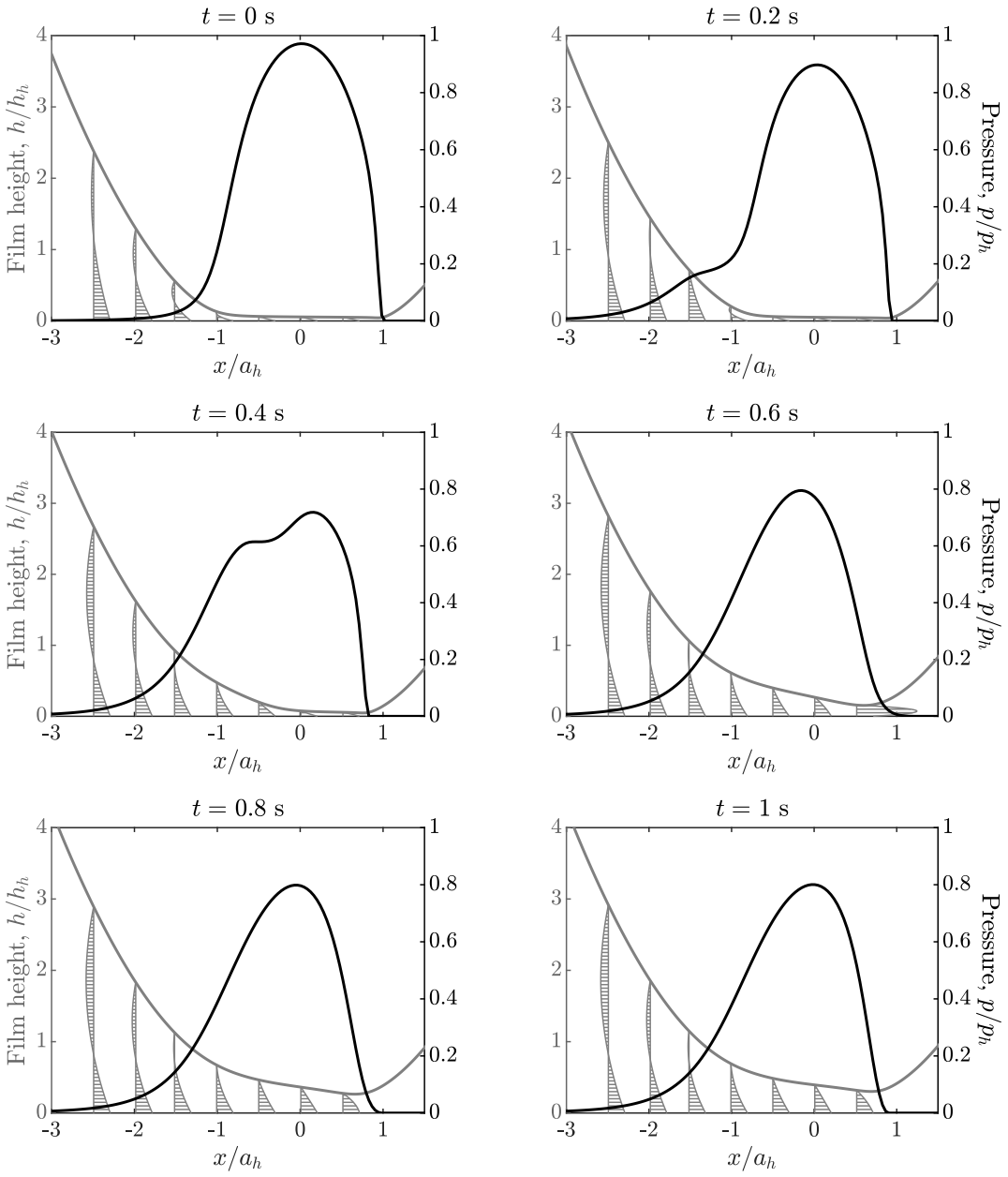
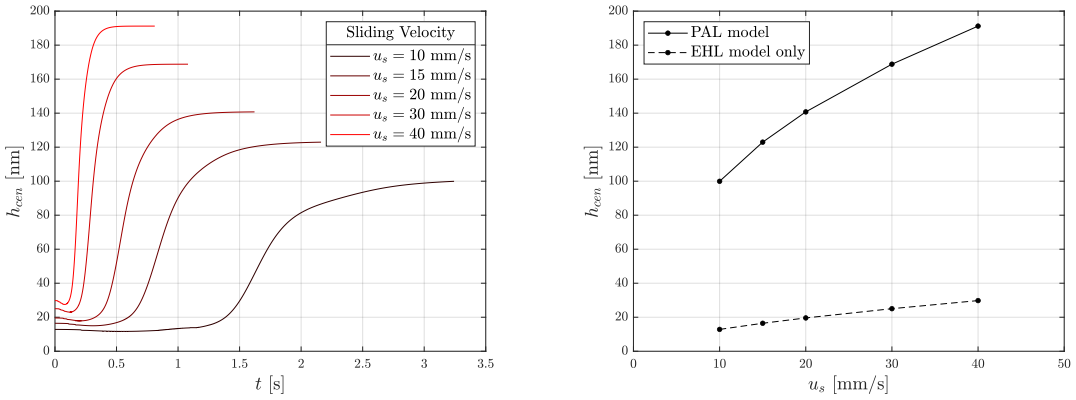


Figure 5.18: *Pressure results (right axis) along $y = 0$ over the first second of protein build up. Also shown in grey (left axis) is the transient film height profile at $y = 0$ and velocity profiles of the lubricating fluid.*

5.5 Varying velocity conditions

Using the parameters, a and $\hat{\eta}$, it is possible to run simulations of varying sliding velocity. Although there are no transient measurements for the range of sliding velocities, it is noted that one of the phenomena of protein aggregation lubrication is that, unlike EHL theory suggests, steady film thicknesses were observed to decrease as sliding velocity increased [69].



(a) (b)

Figure 5.19: *Effect of varying sliding velocity on (a) transient central film thickness development and (b) on final steady central film height. Also shown in plot (b) is the resulting steady film thickness of classical EHL solutions.*

Figure 5.19 shows that as sliding velocity increases, so too does the final steady central film thickness of the lubricating contact. This is consistent with EHL theory but not of the phenomenon observed in experiments. It is believed that the decrease in film thickness with increased sliding velocity occurs because the higher momentum fluid prevents protein aggregation to the same extent. Work by Pritchard, Wilson et al. [98, 99] uses a shear-dependent 'build-up' and 'break-down' term in a scalar transport equation to simulate aggregation behaviour in colloidal systems. This approach combined with a concentration-dependent attenuated flow rate would make for an interesting avenue for further research.

Chapter 6

Conclusions

6.1 Summary

Protein aggregation lubrication can be modelled by using classical elasto-hydrodynamic lubrication theory coupled with a protein concentration-dependent constitutive equation for fluid viscosity where the transport of protein matter in the thin film lubricated contact is subject to an advection-diffusion model using geometry-based attenuation of flow rates. This study has developed the first PAL model of this type with the aim that protein aggregation can be successfully modelled when studying the lubrication mechanisms that govern prosthetic joints. This in turn will allow for more accurate analysis of wear over the lifetime of implants and aid future designs.

An EHL solver has been developed using existing methods and verified against other studies. To maintain mass continuity when using the pressure profile within the contact zone to derive fluid flow rates, a strict convergence criterion for the residual of the Reynolds equation when calculating the elasto-hydrodynamic pressure and film thickness is required. This has been achieved with the use of a decoupled Reynolds equation solver.

Fluid flow rates are attenuated to give modelled protein flow rates by the use of a geometry-based flow rate scaling function dependant of the fluid film height alone with the shape of the approximated protein size distribution. Other factors such as concentration, film height gradient and shear rate dependency have been neglected for simplicity in this study but can be incorporated into the existing model in future with minimal additional work.

The model developed in this study requires the calibration of the parameters, a – the scaling function gradient which relates to the shape of an approximate protein particle size distribution – and, $\hat{\eta}$ – which relates to the nature of the exponential dependency of viscosity on protein concentration. Prior knowledge of the particle size distribution and rheological testing of experimental fluid would allow for these parameters to be fixed without calibration, however a parameter search method has been proposed for situations where these values are unknown.

It is shown that by using the chosen attenuation function to limit protein transport and an exponential, concentration-dependent, local viscosity, simulated transient central film thickness results agree well with previous experimentally-observed behaviour when a cobalt–chromium–molybdenum alloy femoral head implant is tested in a pin-on-flat tribometer using diluted bovine calf serum as a synovial fluid ana-

logue. The results show high concentration gradients in the lubricated contact zone and care must be taken to ensure that an appropriate advection scheme is used that can model this phenomenon.

The calibration of this model to existing experimental results has allowed for further exploration of the phenomena of protein aggregation lubrication. By comparing film height profiles with interferogram results of experiment, it can be seen that the geometry of the surfaces develop from an almost flat contact zone, typical of EHL solutions, to a steeper converging wedge. This effect is due to the rapid increase in fluid viscosity at the inlet as protein matter aggregates and represents a move from the isoviscous-elastic regime towards the isoviscous-rigid regime. Insight by these simulations into the pressure profile present in the contact zone has revealed interesting transient behaviour whereby a secondary pressure peak travels downstream. Although the phenomena of much larger gaps than classical EHL theory would suggest and transient development of film thickness are reproduced well by this computational PAL model, more work must be carried out to better capture the shape of the inlet aggregate and effects of sliding speed.

Modelling prosthesis lubrication in this way provides a simple method to incorporate the effect of protein aggregation into simulations that can be used to provide greater insight into the conditions in the contact zone of joint prostheses including pressure, film height, and protein concentration which can in turn be used to derive friction coefficients and aid the study of surface wear.

6.2 Recommendations for future work

The two model parameters, namely the attenuation function gradient, a, and the dimensionless viscosity parameter, $\hat{\eta}$, have been optimised exclusively for a single experiment. It is recommended that this PAL model be used to simulate various experimental conditions to examine the efficacy of the ability to predict film thicknesses across a range of loading, velocity and material conditions. The parameters of the model are intrinsically linked to these conditions and as such the specific values will likely vary.

Further refinement of the model could also be studied, including closer investigation of the flow attenuation function and protein aggregate size distribution. It may also be necessary to include concentration and time dependence in the attenuation function to capture the transient nature of the size of aggregated macromolecules. Other well-studied features such as the effect of surface roughness, surface adsorption and the shear-dependence of aggregation could also be introduced to better capture the behaviour of protein aggregation lubrication and the phenomenon of decreasing film thickness with increasing sliding velocity, which was not captured by the current model.

The computational efficiency of the PAL model can also be greatly improved. Using multi-level methods and parallelisation techniques could vastly reduce the run time. Using multi-level methods would also allow for Reynolds residuals to be sufficiently reduced without the need for the decoupled Reynolds equation solver, providing a more concise and accurate solution method. These improvements would be necessary to allow protein aggregation lubrication to be modelled in simulations involving full hip and knee geometry, where computational expense reduction is more important. The ability to model PAL is vital for creating simulations that more accurately capture the flow physics of synovial lubrication and can inform predictive wear modelling and aid the design of future joint prostheses.

Bibliography

[1] National Joint Registry (NJR) for England, Wales, Northern Ireland and the Isle of Man, "NJR 16th annual report 2019." Available online: `https://reports.njrcentre.org.uk/Portals/0/PDFdownloads/NJR%2016th%20Annual%20Report%202019.pdf`.

[2] J. T. Evans, J. P. Evans, R. W. Walker, A. W. Blom, M. R. Whitehouse, and A. Sayers, "How long does a hip replacement last? A systematic review and meta-analysis of case series and national registry reports with more than 15 years of follow-up," *Lancet (London, England)*, vol. 393, no. 10172, pp. 647–654, 2019.

[3] U. Cottino, F. Rosso, F. Dettoni, M. Bruzzone, D. E. Bonasia, and R. Rossi, "Treatment of Bone Losses in Revision Total Hip and Knee Arthroplasty Using Trabecular Metal: Current Literature," *Journal of Nanomaterials*, vol. 2016, 2016.

[4] L. Mattei, F. Di Puccio, B. Piccigallo, and E. Ciulli, "Lubrication and wear modelling of artificial hip joints: A review," *Tribology International*, vol. 44, no. 5, pp. 532–549, 2011.

[5] Y. Su, P. Yang, Z. Fu, Z. Jin, and C. Wang, "Time-dependent elastohydrodynamic lubrication analysis of total knee replacement under walking conditions," *Computer Methods in Biomechanics and Biomedical Engineering*, vol. 14, no. 6, pp. 539–548, 2011.

[6] S. L. Smith, D. Dowson, and A. A. J. Goldsmith, "The lubrication of metal-on-metal total hip joints: a slide down the Stribeck curve," *Proceedings of the Institution of Mechanical Engineers, Part J: Journal of Engineering Tribology*, vol. 215, no. 5, pp. 483–493, 2001.

[7] B. Tower, "First Report on Friction Experiments.," *Proceedings of the Institution of Mechanical Engineers*, vol. 34, no. 1, pp. 632–659, 1983.

[8] O. Reynolds, "On the Theory of Lubrication and Its Application to Mr . Beauchamp Tower's Experiments , Including an Experimental Determination of the Viscosity of Olive Oil," *Philosphical Transactions of the Royal Society of London*, vol. 177, no. May, pp. 157–234, 1886.

[9] A. G. Michell, "The lubrication of plane surfaces.," *TRANS. INST. ENGRS. AUST. MECH. ENGNG.*, vol. ME12, no. 3-4 , May. 1988, pp. 49–62, 1988.

[10] A. G. M. Michell, "Improvements in thrust and like bearings," *British Patent No. 875*, 1905.

[11] A. Kingsbury, "Thrust bearings," *U.S. Patent No. 947242*, 1910.

[12] D. Dowson, "Bio-tribology," *Faraday Discussions*, vol. 156, pp. 9–30, 2012.

[13] H. Martin, "Lubrication of gear teeth," *Engineering*, vol. 102, p. 119, 1916.

[14] L. Gümbel, "Über geschmierte arbeitsräder," *Zeitschrift für das gesamte Turbinenwesen*, vol. 24, pp. 245–248, 1916.

[15] A. Ertel, "Hydrodynamic lubrication based on new principles," *Akad. Nauk SSSR Prikadnaya Mathematica i Mekhanika*, vol. 3, no. 2, pp. 41–52, 1939.

[16] A. Grubin, "Fundamentals of the hydrodynamic theory of lubrication of heavily loaded cylindrical surfaces," *Investigation of the Contact Machine Componets*, vol. 2, 1949.

[17] A. Cameron, "Righting a 40-year-old wrong," *Tribology International*, vol. 18, no. 2, p. 92, 1985.

[18] H. Hertz, "Ueber die berührung fester elastischer körper.," *Journal für die reine und angewandte Mathematik*, vol. 92, pp. 156–171, 1882.

[19] D. Dowson and P. Ehret, "Past, present and future studies in elastohydrodynamics," *Proceedings of the Institution of Mechanical Engineers, Part J: Journal of Engineering Tribology*, vol. 213, no. 5, pp. 317–333, 1999.

[20] A. Petrusevich, "The basic conclusions from the elasto-hydrodynamic theory of lubrication," *Izv. Akad. Nauk SSSR, Odt. Tekhn. Nauk*, no. 2, p. 209, 1951.

[21] C. Barus, "Isothermals, isopiestics and isometrics relative to viscosity," *American Journal of Science*, 1893.

[22] D. Zhu and Q. J. Wang, *EHL History (Elastohydrodynamic Lubrication)*, pp. 832–847. Boston, MA: Springer US, 2013.

[23] D. Dowson and G. R. Higginson, "A Numerical Solution to the Elasto-Hydrodynamic Problem," *Journal of Mechanical Engineering Science*, vol. 1, no. 1, pp. 6–15, 1959.

[24] D. Dowson and G. R. Higginson, "The Effect of Material Properties on the Lubrication of Elastic Rollers," *Journal of Mechanical Engineering Science*, 1960.

[25] D. Dowson and G. Higginson, "New roller-bearing lubrication formula," *Engineering Lond.*, vol. 192, p. 158, 1961.

[26] D. Dowson and G. Higginson, *Elasto-hydrodynamic lubrication*. International series on materials science and technology, Pergamon Press, 1977.

[27] Ranger, A. P., C. . M. . M. Ettles, and A. Cameron, "The solution of the point contact elasto-hydrodynamic problem," *Proceedings of the Royal Society of London. A. Mathematical and Physical Sciences*, vol. 346, no. 1645, pp. 227–244, 1975.

[28] B. J. Hamrock and D. Dowson, "Isothermal Elastohydrodynamic Lubrication of Point Contacts: Part I—Theoretical Formulation," *Journal of Lubrication Technology*, vol. 98, pp. 223–228, apr 1976.

[29] B. J. Hamrock and D. Dowson, "Isothermal Elastohydrodynamic Lubrication of Point Contacts: Part II—Ellipticity Parameter Results," *Journal of Lubrication Technology*, vol. 98, pp. 375–381, jul 1976.

[30] B. J. Hamrock and D. Dowson, "Isothermal Elastohydrodynamic Lubrication of Point Contacts: Part III—Fully Flooded Results," *Journal of Lubrication Technology*, vol. 99, pp. 264–275, apr 1977.

[31] B. J. Hamrock and D. Dowson, "Isothermal Elastohydrodynamic Lubrication of Point Contacts: Part IV—Starvation Results," *Journal of Lubrication Technology*, vol. 99, pp. 15–23, jan 1977.

[32] H. S. Cheng and B. Sternlicht, "A numerical solution for the pressure, tem-

perature, and film thickness between two infinitely long, lubricated rolling and sliding cylinders, under heavy loads," *Journal of Fluids Engineering, Transactions of the ASME*, 1965.

[33] D. Dowson and A. V. Whitaker, "Paper 4: A Numerical Procedure for the Solution of the Elastohydrodynamic Problem of Rolling and Sliding Contacts Lubricated by a Newtonian Fluid," *Proceedings of the Institution of Mechanical Engineers, Conference Proceedings*, 1965.

[34] D. Zhu and S.-Z. Wen, "A full numerical solution for the thermoelastohydrodynamic problem in elliptical contacts," *Journal of Tribology*, 1984.

[35] L. D. Wedeven, D. Evans, and A. Cameron, "Optical analysis of ball bearing starvation," *Journal of Tribology*, 1971.

[36] W. B. Hardy and I. Doubleday, "Boundary lubrication.— The paraffin series," *Proceedings of the Royal Society of London. Series A, Containing Papers of a Mathematical and Physical Character*, 1922.

[37] R. Stribeck, "Die wesentlichen eigenshaften der gleit-und rollenlager," *VDI-Zeitschrift*, 1902.

[38] L. Gümbel, "Das problem der lagerreibung," *Mbl. Berlin. Bez. Ver. dtsch. Ing*, vol. 5, pp. 87–104, 1914.

[39] C. Myant and P. Cann, "On the matter of synovial fluid lubrication: Implications for Metal-on-Metal hip tribology," *Journal of the Mechanical Behavior of Biomedical Materials*, vol. 34, pp. 338–348, 2014.

[40] N. Patir and H. S. Cheng, "An Average Flow Model for Determining Effects of Three-Dimensional Roughness on Partial Hydrodynamic Lubrication," *Journal of Lubrication Technology*, vol. 100, no. 1, p. 12, 1978.

[41] N. Patir and M. S. Cheng, "Application of average flow model to lubrication between rough sliding surfaces," *Journal of Tribology*, vol. 101, no. 2, pp. 220–229, 1979.

[42] A. A. Lubrecht, W. E. ten Napel, and R. Bosma, "Closure to "Discussion of 'Multigrid, An Alternative Method for Calculating Film Thickness and Pressure Profiles in Elastohydrodynamically Lubricated Line Contacts'" (1986, ASME J. Tribol., 108, p. 556)," *Journal of Tribology*, vol. 108, no. 4, p. 556, 1986.

[43] C. H. Venner, *Multilevel solutions of the EHL line and point contact problems*. PhD thesis, University of Twente, 1991.

[44] C. H. Venner and A. A. Lubrecht, "Multilevel methods in lubrication," *Tribology Series*, vol. 37, 2000.

[45] N. Ren, D. Zhu, W. W. Chen, Y. Liu, and Q. J. Wang, "A three-dimensional deterministic model for rough surface line-contact EHL problems," *Journal of Tribology*, 2009.

[46] W. Hunter, "VI. Of the structure and diseases of articulating cartilages," *Philosophical Transactions of the Royal Society of London*, vol. 42, no. 470, pp. 514–521, 1743.

[47] R. L. Drake, A. W. Vogl, and A. W. Mitchell, *Gray's Anatomy for Students, 4th Edition*. Churchill Livingstone/Elsevier, 2019.

[48] C. W. McCutchen, "The frictional properties of animal joints," *Wear*, 1962.

[49] D. Dowson, "Paper 12: Modes of Lubrication in Human Joints," *Proceedings of the Institution of Mechanical Engineers, Conference Proceedings*, 1966.

[50] C. Parsons, R. Batson, S. Reighard, S. Tanner, B. Snider, and T. B. Pace, "Clinical outcomes assessment of three similar hip arthroplasty bearing surfaces," *Orthopedic Reviews*, vol. 6, no. 2, 2014.

[51] C. Varnum, A. B. Pedersen, P. Kjærsgaard-Andersen, and S. Overgaard, "Do different types of bearings and noise from total hip arthroplasty influence hip-related pain, function, and quality of life postoperatively?: A cross-sectional study from the Danish Hip Arthroplasty Registry," *Acta Orthopaedica*, vol. 87, no. 6, pp. 567–574, 2016.

[52] T. Kitano, G. A. Ateshian, V. C. Mow, Y. Kadoya, and Y. Yamano, "Constituents and pH changes in protein rich hyaluronan solution affect the biotribological properties of artificial articular joints," *Journal of Biomechanics*, vol. 34, no. 8, pp. 1031–1037, 2001.

[53] A. Wang, A. Essner, and G. Schmidig, "The Effects of Lubricant Composition on in Vitro Wear Testing of Polymeric Acetabular Components," *Journal of Biomedical Materials Research - Part B Applied Biomaterials*, vol. 68, no. 1, pp. 45–52, 2004.

[54] A. F. Cooke, D. Dowson, and V. Wright, "The rheology of synovial fluid and some potential synthetic lubricants for degenerate synovial joints," *Engineering in Medicine*, vol. 7, no. 2, pp. 66–72, 1978.

[55] Z. M. Jin, D. Dowson, and J. Fisher, "Analysis of fluid film lubrication in artificial hip joint replacements with surfaces of high elastic modulus," *Proceedings of the Institution of Mechanical Engineers, Part H: Journal of Engineering in Medicine*, vol. 211, no. 3, pp. 247–256, 1997.

[56] M. M. Castellanos, J. A. Pathak, and R. H. Colby, "Both protein adsorption and aggregation contribute to shear yielding and viscosity increase in protein solutions," *Soft Matter*, vol. 10, no. 1, pp. 122–131, 2014.

[57] P. J. Coleman, D. Scott, R. M. Mason, and J. R. Levick, "Characterization of the effect of high molecular weight hyaluronan on trans-synovial flow in rabbit knees," *Journal of Physiology*, vol. 514, no. 1, pp. 265–282, 1999.

[58] E. A. Balazs, "The Physical Properties of Synovial Fluid and the Special Role of Hyaluronic Acid," 1974.

[59] D. V. Davies, "Properties of Synovial Fluid," *Proc Instn Mech Engrs*, pp. 25–29, 1966.

[60] K. M. Oates, W. E. Krause, R. L. Jones, and R. H. Colby, "Rheopexy of synovial fluid and protein aggregation," *Journal of the Royal Society Interface*, vol. 3, no. 6, pp. 167–174, 2006.

[61] D. Jalali-Vahid and Z. M. Jin, "Transient elastohydrodynamic lubrication analysis of ultra-high molecular weight polyethylene hip joint replacements," *Proceedings of the Institution of Mechanical Engineers, Part C: Journal of Mechanical Engineering Science*, vol. 216, no. 4, pp. 409–420, 2002.

[62] I. J. Udofia and Z. M. Jin, "Elastohydrodynamic lubrication analysis of metal-on-metal hip-resurfacing prostheses," *Journal of Biomechanics*, vol. 36, no. 4, pp. 537–544, 2003.

[63] L. Gao, F. Wang, P. Yang, and Z. Jin, "Effect of 3D physiological loading and motion on elastohydrodynamic lubrication of metal-on-metal total hip replacements," *Medical Engineering and Physics*, vol. 31, no. 6, pp. 720–729, 2009.

[64] L. Gao, D. Dowson, and R. W. Hewson, "A numerical study of non-Newtonian

transient elastohydrodynamic lubrication of metal-on-metal hip prostheses," *Tribology International*, vol. 93, pp. 486–494, 2016.

[65] W. Z. Wang, Z. M. Jin, D. Dowson, and Y. Z. Hu, "A study of the effect of model geometry and lubricant rheology upon the elastohydrodynamic lubrication performance of metal-on-metal hip joints," *Proceedings of the Institution of Mechanical Engineers, Part J: Journal of Engineering Tribology*, vol. 222, no. 3, pp. 493–501, 2008.

[66] Z. M. Jin, "Theoretical studies of elastohydrodynamic lubrication of artificial hip joints," *Proceedings of the Institution of Mechanical Engineers, Part J: Journal of Engineering Tribology*, vol. 220, no. 8, pp. 719–727, 2006.

[67] H. A. Butt, L. Nissim, R. Hewson, L. Gao, and C. Myant, "Lubrication model of the human knee implant," in *15th International Symposium on Computer Methods in Biomechanics and Biomedical Engineering and 3rd Conference on Imaging and Visualization*, 2018.

[68] M. Mongkolwongrojn, K. Wongseedakaew, and F. E. Kennedy, "Transient elastohydrodynamic lubrication in artificial knee joint with non-Newtonian fluids," *Tribology International*, vol. 43, no. 5-6, pp. 1017–1026, 2010.

[69] C. Myant and P. Cann, "In contact observation of model synovial fluid lubricating mechanisms," *Tribology International*, vol. 63, pp. 97–104, 2013.

[70] C. Myant, R. Underwood, J. Fan, and P. M. Cann, "Lubrication of metal-on-metal hip joints: The effect of protein content and load on film formation and wear," *Journal of the Mechanical Behavior of Biomedical Materials*, vol. 6, pp. 30–40, 2012.

[71] C. W. Myant and P. Cann, "The effect of transient conditions on synovial fluid protein aggregation lubrication," *Journal of the Mechanical Behavior of Biomedical Materials*, vol. 34, pp. 349–357, 2014.

[72] C. Myant, M. Fowell, and P. Cann, "The effect of transient motion on Isoviscous-EHL films in compliant, point, contacts," *Tribology International*, vol. 72, pp. 98–107, 2014.

[73] J. Fan, C. W. Myant, R. Underwood, P. M. Cann, and A. Hart, "Inlet protein aggregation: A new mechanism for lubricating film formation with model

synovial fluids," *Proceedings of the Institution of Mechanical Engineers, Part H: Journal of Engineering in Medicine*, vol. 225, no. 7, pp. 696–709, 2011.

[74] J. Fan, C. Myant, R. Underwood, and P. Cann, "Synovial fluid lubrication of artificial joints: Protein film formation and composition," *Faraday Discussions*, vol. 156, pp. 69–85, 2012.

[75] D. Nečas, M. Vrbka, F. Urban, I. Křupka, and M. Hartl, "The effect of lubricant constituents on lubrication mechanisms in hip joint replacements," *Journal of the Mechanical Behavior of Biomedical Materials*, vol. 55, pp. 295–307, mar 2016.

[76] D. Nečas, M. Vrbka, F. Urban, J. Gallo, I. Křupka, and M. Hartl, "In situ observation of lubricant film formation in THR considering real conformity: The effect of diameter, clearance and material," *Journal of the Mechanical Behavior of Biomedical Materials*, vol. 69, no. December 2016, pp. 66–74, 2017.

[77] D. Nečas, M. Vrbka, I. Křupka, and M. Hartl, "The effect of kinematic conditions and synovial fluid composition on the frictional behaviour of materials for artificial joints," *Materials*, vol. 11, no. 5, pp. 1–12, 2018.

[78] D. Nečas, M. Vrbka, D. Rebenda, J. Gallo, A. Galandáková, L. Wolfová, I. Křupka, and M. Hartl, "In situ observation of lubricant film formation in THR considering real conformity: The effect of model synovial fluid composition," *Tribology International*, vol. 117, no. June 2017, pp. 206–216, 2018.

[79] D. Nečas, M. Vrbka, A. Galandáková, I. Křupka, and M. Hartl, "On the observation of lubrication mechanisms within hip joint replacements. Part I: Hard-on-soft bearing pairs," *Journal of the Mechanical Behavior of Biomedical Materials*, vol. 89, no. September 2018, pp. 237–248, 2019.

[80] D. Nečas, M. Vrbka, J. Gallo, I. Křupka, and M. Hartl, "On the observation of lubrication mechanisms within hip joint replacements. Part II: Hard-on-hard bearing pairs," *Journal of the Mechanical Behavior of Biomedical Materials*, vol. 89, no. September 2018, pp. 249–259, 2019.

[81] X. Lu, D. Nečas, Q. Meng, D. Rebenda, M. Vrbka, M. Hartl, and Z. Jin, "Towards the direct validation of computational lubrication modelling of hip replacements," *Tribology International*, vol. 146, no. December 2019, 2020.

[82] E. Ciulli, T. Draexl, and K. Stadler, "Film thickness analysis for EHL contacts under steady-state and transient conditions by automatic digital image processing," *Advances in Tribology*, vol. 2008, 2008.

[83] H. A. Spikes, "Thin films in elastohydrodynamic lubrication: The contribution of experiment," *Proceedings of the Institution of Mechanical Engineers, Part J: Journal of Engineering Tribology*, vol. 213, no. 5, pp. 335–352, 1999.

[84] N. Marx, J. Guegan, and H. A. Spikes, "Elastohydrodynamic film thickness of soft EHL contacts using optical interferometry," *Tribology International*, vol. 99, pp. 267–277, 2016.

[85] C. J. Hooke, "The Elastohydrodynamic Lubrication of Heavily Loaded Contacts," *Journal of Mechanical Engineering Science*, vol. 19, pp. 149–156, aug 1977.

[86] J. Brady, "Stokesian Dynamics," *Annual Review of Fluid Mechanics*, vol. 20, no. 1, pp. 111–157, 1988.

[87] G. C. Agbangla, É. Climent, and P. Bacchin, "Numerical investigation of channel blockage by flowing microparticles," *Computers and Fluids*, vol. 94, pp. 69–83, 2014.

[88] C. Bridges and K. R. Rajagopal, "Pulsatile Flow of a Chemically-Reacting Nonlinear Fluid," *Computers and Mathematics with Applications*, vol. 52, no. 6-7, pp. 1131–1144, 2006.

[89] P. Pustěovská, J. Hron, J. Málek, and K. R. Rajagopal, "On the modeling of the synovial fluid," *Advances in Tribology*, vol. 2010, 2010.

[90] H. W. Swift, "the Stability of Lubricating Films in Journal Bearings. (Includes Appendix).," *Minutes of the Proceedings of the Institution of Civil Engineers*, vol. 233, no. 1932, pp. 267–288, 1932.

[91] W. Stieber, *Das Schwimmlager: Hydrodynamische Theorie des Gleitlagers.* VDI-Verlag, 1933.

[92] A. Love, *A treatise on the mathematical theory of elasticity.* Cambridge University Press, 1892.

[93] H. Moes, "Optimum similarity analysis with applications to elastohydrodynamic lubrication," *Wear*, vol. 159, no. 1, pp. 57–66, 1992.

[94] B. J. Hamrock and D. Dowson, "Elastohydrodynamic Lubrication of Elliptical Contacts for Materials of Low Elastic Modulus.," *American Society of Mechanical Engineers (Paper)*, vol. 100, no. 78 -Lub-1, 1978.

[95] C. H. Venner, *venner.pdf*. Phd thesis, University of Twente, 1991.

[96] L. M. Gao, Q. E. Meng, F. C. Wang, P. R. Yang, and Z. M. Jin, "Comparison of numerical methods for elastohydrodynamic lubrication analysis of metal-on-metal hip implants: Multi-grid verses Newton-Raphson," *Proceedings of the Institution of Mechanical Engineers, Part J: Journal of Engineering Tribology*, vol. 221, no. 2, pp. 133–140, 2007.

[97] M. J. Braun and W. M. Hannon, "Cavitation formation and modelling for fluid film bearings: A review," *Proceedings of the Institution of Mechanical Engineers, Part J: Journal of Engineering Tribology*, vol. 224, no. 9, pp. 839–863, 2010.

[98] D. Pritchard, S. K. Wilson, and C. R. McArdle, "Flow of a thixotropic or antithixotropic fluid in a slowly varying channel: The weakly advective regime," *Journal of Non-Newtonian Fluid Mechanics*, vol. 238, pp. 140–157, 2016.

[99] A. I. Croudace, D. Pritchard, and S. K. Wilson, "Unsteady flow of a thixotropic fluid in a slowly varying pipe," *Physics of Fluids*, vol. 29, no. 8, 2017.

[100] R. Courant, K. Friedrichs, and H. Lewy, "Über die partiellen Differenzengleichungen der mathematischen Physik," *Mathematische Annalen*, 1928.

[101] L. Kong, P. Zhu, Y. Wang, and Z. Zeng, "Efficient and accurate numerical methods for the multidimensional convection–diffusion equations," *Mathematics and Computers in Simulation*, vol. 162, pp. 179–194, 2019.

[102] W. A. Wakeham, N. H. Salpadoru, and C. G. Caro, "Diffusion coefficients for protein molecules in blood serum," *Atherosclerosis*, vol. 25, pp. 225–235, nov 1976.

[103] S. J. McClellan and E. I. Franses, "Adsorption of bovine serum albumin at solid/aqueous interfaces," *Colloids and Surfaces A: Physicochemical and Engineering Aspects*, vol. 260, no. 1-3, pp. 265–275, 2005.

[104] K. Nakanishi, T. Sakiyama, and K. Imamura, "On the adsorption of proteins

on solid surfaces, a common but very complicated phenomenon," *Journal of Bioscience and Bioengineering*, vol. 91, no. 3, pp. 233–244, 2001.

[105] R. J. Hunter, *Foundations of Colloid Science (2nd Edition)*. Oxford University Press, 2001.

[106] R. Byron Bird Warren E. Stewart Edwin N. Lightfoo, R. B. Bird, W. E. Stewart, and E. N. Lightfoot, *Transport Phenomena, Revised 2nd Edition*. John Wiley & Sons, Inc., 2006.

[107] G. C. Agbangla, P. Bacchin, and E. Climent, "Collective dynamics of flowing colloids during pore clogging," *Soft Matter*, vol. 10, no. 33, pp. 6303–6315, 2014.

[108] E. Dressaire and A. Sauret, "Clogging of microfluidic systems," *Soft Matter*, vol. 13, no. 1, pp. 37–48, 2017.

[109] I. Axelsson, "Characterization of proteins and other macromolecules by agarose gel chromatography," *Journal of Chromatography*, vol. 152, pp. 21–32, 1978.

[110] P. Plietz, G. Damaschun, D. Zirwer, K. Gast, K. D. Schwenke, and V. Prakash, "Shape and quaternary structure of α-globulin from sesame (Sesamum indicum L.) seed as revealed by small angle x-ray scattering and quasi-elastic light scattering," *Journal of Biological Chemistry*, vol. 261, no. 27, pp. 12686–12691, 1986.

[111] P. Atkins and J. De Paula, *Physical Chemistry 8th Edition*. W.H. Freeman and Company New York, 2006.

[112] A. D. Randolph and M. A. Larson, "PARTICLE DISTRIBUTIONS," in *Theory of Particulate Processes*, 1988.

[113] T. Blickle, B. G. Lakatos, C. Mihálykó, and Z. Ulbert, "The hyperbolic tangent distribution family," *Powder Technology*, vol. 97, no. 2, pp. 100–108, 1998.

[114] B. Bodor, B. G. Lakatos, and T. Blickle, "Characterization of Crystal Populations of Vitamin C by Hyperbolic Tangent Distribution Functions," *Hungarian Journal of Industry and Chemistry*, vol. 21, pp. 233–238, sep 1993.

[115] D. R. Richmond, W. Newlon Tauxe, and J. B. Bassingthwaighte, "Albumin macroaggregates and measurements of regional blood flow: Validity and ap-

plication of particle sizing by Coulter counter," *The Journal of Laboratory and Clinical Medicine*, vol. 75, no. 2, pp. 336–346, 1970.

[116] M. Grimaldo, F. Roosen-Runge, F. Zhang, T. Seydel, and F. Schreiber, "Diffusion and dynamics of γ-globulin in crowded aqueous solutions," *Journal of Physical Chemistry B*, vol. 118, no. 25, pp. 7203–7209, 2014.

[117] F. Roosen-Runge, M. Hennig, F. Zhang, R. M. Jacobs, M. Sztucki, H. Schober, T. Seydel, and F. Schreiber, "Protein self-diffusion in crowded solutions," *Proceedings of the National Academy of Sciences of the United States of America*, vol. 108, no. 29, pp. 11815–11820, 2011.

[118] B. J. Hamrock and D. Dowson, *Ball bearing lubrication. The elastohydrodynamics of elliptical contacts.* John Wiley & Sons Inc., 1981.

[119] M. Esfahanian and B. J. Hamrock, "Fluid-film lubrication regimes revisited," *Tribology Transactions*, vol. 34, no. 4, pp. 628–632, 1991.

[120] P. C. Nalam, J. N. Clasohm, A. Mashaghi, and N. D. Spencer, "Macrotribological studies of poly(L-lysine)-graft-Poly(ethylene glycol) in aqueous glycerol mixtures," *Tribology Letters*, vol. 37, no. 3, pp. 541–552, 2010.

Appendix A

Derivations

A.1 Derivation of the Reynolds equation

We start with the steady, 3D, incompressible Navier-Stokes equations:

$$\begin{cases} \mathbf{u} \cdot \nabla \mathbf{u} & = -\frac{1}{\rho} \nabla p + \nu \nabla^2 \mathbf{u} \\ \nabla \cdot \mathbf{u} & = 0 \end{cases} \tag{A.1.1}$$

And apply this to the following problem geometry:

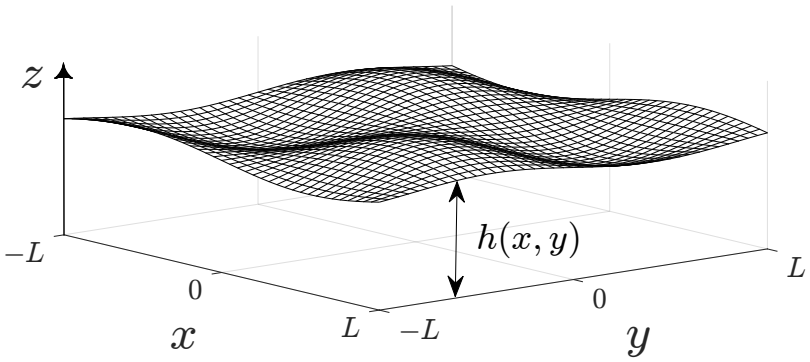


Figure A.1: *Geometry of a typical thin film problem in which x and y scale with some characteristic variable L and the film has height $h = h(x, y)$ in the z-direction.*

Here, the characteristic length scales in x and y are of the same order, L, while the characteristic length scale in the z-direction is the film height, h, which is variable but always results in $h << L$. Giving the velocities u, v and w the characteristic scales U, V and W, we can proceed to non-dimensionalise the problem using the following scalings, where starred variables are dimensionless and $\mathcal{O}(1)$:

$$\begin{aligned} u &= u^* U & x &= x^* L \\ v &= v^* V & y &= y^* L \\ w &= w^* W & z &= z^* h \end{aligned} \tag{A.1.2}$$

The continuity equation from Equation (A.1.1) can now be analysed to determine the relative scaling of the characteristic velocities.

$$\frac{U}{L}\frac{\partial u^*}{\partial x^*} + \frac{V}{L}\frac{\partial v^*}{\partial y^*} + \frac{W}{h}\frac{\partial w^*}{\partial z^*} = 0 \tag{A.1.3}$$

Given that the starred variables are $\mathcal{O}(1)$, it follows that the following scaling relations apply to the characteristic velocities:

$$V \sim U \qquad \text{and} \qquad W \sim U\frac{h}{L} \tag{A.1.4}$$

Using these results, it is possible to simplify the momentum equations of Equation (A.1.1).

$$\underbrace{\frac{U^2}{L}u^*\frac{\partial u^*}{\partial x^*} + \frac{UV}{L}v^*\frac{\partial u^*}{\partial y^*} + \frac{UW}{h}w^*\frac{\partial u^*}{\partial z^*}}_{\textcircled{1}} =$$

$$\underbrace{-\frac{1}{\rho}\frac{\partial p}{\partial x}}_{\textcircled{2}} + \nu\Bigg(\underbrace{\frac{U}{L^2}\frac{\partial^2 u^*}{\partial x^{*2}} + \frac{U}{L^2}\frac{\partial^2 u^*}{\partial y^{*2}}}_{\textcircled{3}} + \underbrace{\frac{U}{h^2}\frac{\partial^2 u^*}{\partial z^{*2}}}_{\textcircled{4}}\Bigg) \tag{A.1.5}$$

Starting with just the x-direction and using the scaling from Eq. (A.1.4), it can be seen that all of the inertial terms have the same order and are grouped together here as group 1. The pressure term (alone in group 2) is of unknown magnitude as yet and is therefore not scaled in the same manner as the other terms. The viscous terms are in two distinct groups of which it is clear to see that group 4 is much larger than group 3 and so these two smaller terms may be neglected. When comparing group 1 to group 4, the following ratio exists:

$$\frac{\textcircled{1}}{\textcircled{4}} \Rightarrow \frac{U^2/L}{\nu U/h^2} \Rightarrow \left(\frac{UL}{\nu}\right)\left(\frac{h}{L}\right)^2 \Rightarrow Re_L\left(\frac{h}{L}\right)^2 \tag{A.1.6}$$

In this case it is assumed that h/L is sufficiently smaller than the Reynolds number so that group 1 can also be neglected. Because h/L is squared and is generally very small in bearings, it is feasible for the Reynolds number, Re_L, to become quite large and this approximation to remain true.

After these terms are neglected, Eq. (A.1.5) becomes

$$\frac{\nu U}{h^2}\frac{\partial^2 u^*}{\partial z^{*2}} = \frac{1}{\rho}\frac{\partial p}{\partial x} \tag{A.1.7}$$

and it follows that the pressure term must scale such that

$$\frac{\partial p}{\partial x} \sim \frac{\eta U}{h^2}. \tag{A.1.8}$$

Repeating this analysis for the momentum equations in the other two directions results in the same terms being neglected and the resulting pressure gradient scalings:

$$\frac{\partial p}{\partial y} \sim \frac{\partial p}{\partial x} \sim \frac{\eta U}{h^2} \qquad \text{and} \qquad \frac{\partial p}{\partial z} \sim \frac{\eta U}{h^2}\left(\frac{h}{L}\right) \tag{A.1.9}$$

suggesting that the pressure gradients across the thin fluid film height are negligible compared to along the bearing, thereby reducing the pressure field to two dimensions, i.e. $p = p(x, y)$.

Using these scaling arguments, the x-direction momentum equation has been reduced to

$$\eta \frac{\partial^2 u}{\partial z^2} = \frac{\partial p}{\partial x}, \tag{A.1.10}$$

which can be integrated twice to obtain

$$u = \frac{1}{2\eta}\frac{\partial p}{\partial x} z^2 + C_1 z + C_2. \tag{A.1.11}$$

Using the boundary conditions

$$u = U_0 \quad \text{on} \quad z = 0 \qquad \text{and} \qquad u = U_h \quad \text{on} \quad z = h, \tag{A.1.12}$$

it is possible to find the constants

$$C_1 = \frac{\eta(U_h - U_0)}{h} - \frac{\partial p}{\partial x}\frac{h}{2} \qquad \text{and} \qquad C_2 = \eta U_0 \tag{A.1.13}$$

giving the velocity profile

$$u = \frac{1}{2\eta}\frac{\partial p}{\partial x}(z^2 - zh) + (U_h - U_0)\frac{z}{h} + U_0 \tag{A.1.14}$$

and similarly for the y-direction

$$v = \frac{1}{2\eta}\frac{\partial p}{\partial y}(z^2 - zh) + (V_h - V_0)\frac{z}{h} + V_0 \tag{A.1.15}$$

where V_0 and V_h are the velocities in the y-direction at $z = 0$ and $z = h$ respectively.

Returning to the continuity equation of Eq (A.1.1) it is possible to integrate over the z-direction to obtain

$$\int_0^h \frac{\partial u}{\partial x} dz + \int_0^h \frac{\partial v}{\partial y} dz + \big[w\big]_0^h = 0 \tag{A.1.16}$$

and use the general result

$$\int_a^b \frac{\partial}{\partial x} f(x, y, z) dz = \frac{\partial}{\partial x}\int_a^b f(x, y, z) dz - f(x, y, b)\frac{\partial b}{\partial x} + f(x, y, a)\frac{\partial a}{\partial x} \tag{A.1.17}$$

to give

$$\frac{\partial}{\partial x}\int_0^h u dz + \frac{\partial}{\partial y}\int_0^h v dz - U_h\frac{\partial h}{\partial x} - V_h\frac{\partial h}{\partial y} + (W_h - W_0) = 0. \tag{A.1.18}$$

Integrating the velocity u results in

$$\int_0^h u dz = -\frac{h^3}{12\eta}\frac{\partial p}{\partial x} + \frac{1}{2}(U_h + U_0)h, \tag{A.1.19}$$

and thus substituting this and the analogous integral of v into Eq. (A.1.18) generates

$$\frac{\partial}{\partial x}\left(\frac{h^3}{\eta}\frac{\partial p}{\partial x}\right) + \frac{\partial}{\partial y}\left(\frac{h^3}{\eta}\frac{\partial p}{\partial y}\right) =$$

$$12\left\{\frac{\partial}{\partial x}\left(\frac{(U_h + U_0)}{2}h\right) + \frac{\partial}{\partial y}\left(\frac{(V_h + V_0)}{2}h\right)\right\} + 12\big(W_h - W_0\big) \tag{A.1.20}$$

which is the full Reynolds equation. Several simplifications can be made to this equation to make it more usable, the first being just a change of notation without loss of generality. The sum entrainment velocity, u_s, can be defined as $u_s = U_0 + U_h$ and similarly in the y-direction for velocity, v_s. In most cases, the sum velocity will not be a function of x or y and so for the purposes of this report u_s and v_s can be taken outside the differentiation. Velocities in the z-direction can be re-scripted as derivatives of the film thickness and so the last term can be rewritten as $\partial h/\partial t$. These assumptions reform the Reynolds equation to the following:

$$\frac{\partial}{\partial x}\left(\frac{h^3}{\eta}\frac{\partial p}{\partial x}\right) + \frac{\partial}{\partial y}\left(\frac{h^3}{\eta}\frac{\partial p}{\partial y}\right) = 6\left\{u_s\frac{\partial h}{\partial x} + v_s\frac{\partial h}{\partial y}\right\} + 12\frac{\partial h}{\partial t} \tag{A.1.21}$$

Appendix B

Non-Dimensionalisation

B.1 Hertzian method

The method of non-dimensionalisation used in this thesis is based on the parameters obtained by the Hertzian theory of dry point contact mechanics [18]. As covered in the main body of this text, the dimensional variables are scaled in the following manner

$$\begin{aligned} X &= x/a_h & Y &= y/a_h \\ P &= p/p_h & H &= h/h_h \\ \tilde{\rho} &= \rho/\rho_0 & \tilde{\eta} &= \eta/\eta_0 \end{aligned} \tag{B.1.1}$$

where a_h, p_h and h_h are the Hertzian contact radius, maximum pressure and maximum deformation respectively, given by

$$a_h = \left(\frac{3wR}{2E'}\right)^{1/3} \quad p_h = \frac{3w}{2\pi {a_h}^2} \quad h_h = \frac{{a_h}^2}{R} \tag{B.1.2}$$

This method results in the dimensionless parameters,

$$\lambda = \frac{6u_s\eta_0 R^2}{{a_h}^3 p_h} \qquad \bar{\alpha} = \alpha p_h \tag{B.1.3}$$

where α is the pressure-viscosity coefficient. In this study however, the contact is assumed to operate in the isoviscous regime and therefore $\bar{\alpha}$ is assumed to be zero.

B.2 Dowson and Higginson method

The non-dimensionalisation method proposed by Dowson and Higginson for 1D line contact problems [26] and extended by Hamrock and Dowson for 2D point contact problems [28–31] uses the following scaling relations

$$\begin{aligned} X &= x/a_h & Y &= y/a_h \\ P &= p/E' & H &= h/R \\ \tilde{\rho} &= \rho/\rho_0 & \tilde{\eta} &= \eta/\eta_0 \end{aligned} \tag{B.2.1}$$

where a_h is the Hertzian contact radius, and includes the following dimensionless parameters,

$$U = \frac{\eta_0 u_s}{E'R} \qquad W = \frac{w}{E'R^2} \qquad G = \alpha E' \tag{B.2.2}$$

The parameters, U, W and G hold very intuitive and independent meaning as the speed, load and material parameters respectively. The speed parameter is sometimes stated as half of the value expressed here.

B.3 Moes method

Moes used an alternate non-dimensionalisation method to approach the point contact EHL problem [93] using the following scaling relations

$$\begin{aligned} X &= \frac{x}{R}\left(\frac{E'R}{\eta_0 u_s}\right)^{1/4} & Y &= \frac{y}{R}\left(\frac{E'R}{\eta_0 u_s}\right)^{1/4} \\ P &= \frac{p}{E'}\left(\frac{E'R}{\eta_0 u_s}\right)^{1/4} & H &= \frac{h}{R}\left(\frac{E'R}{\eta_0 u_s}\right)^{1/2} \\ \tilde{\rho} &= \rho/\rho_0 & \tilde{\eta} &= \eta/\eta_0 \end{aligned} \tag{B.3.1}$$

This method results in the dimensionless parameters

$$M = \frac{w}{E'R^2}\left(\frac{E'R}{\eta_0 u_s}\right)^{3/4} \qquad L = \alpha E'\left(\frac{E'R}{\eta_0 u_s}\right)^{-1/4} \tag{B.3.2}$$

These parameters are often used to compare studies as film height can be plotted against the two parameters M and L as opposed to the three parameters U, W, and G given by Dowson and Higginson.

B.4 Relation between schemes

As the Moes parameters are often used for comparison between studies, the key dimensionless parameters of the Hertzian method can be expressed in terms of M and L in the following way as shown by Venner [43]

$$\bar{\alpha} = \frac{L}{\pi}\left(\frac{3M}{2}\right)^{1/3} \qquad \lambda = \left(\frac{128\pi^3}{3M^4}\right)^{1/3} \tag{B.4.1}$$

and the Moes parameters can be expressed as

$$M = WU^{-3/4} \qquad L = GU^{1/4} \tag{B.4.2}$$

using the Dowson and Higginson parameters. Note should be taken that these expressions rely on the Dowson and Higginson speed parameter not having a factor of 1/2.

Appendix C

Numerical accuracy and model refinement details

C.1 Time-step size

The parameter search used a time-step size of $\Delta T = 0.1$ and simulations with time-step size equal to half of this value and double this value have also been run.

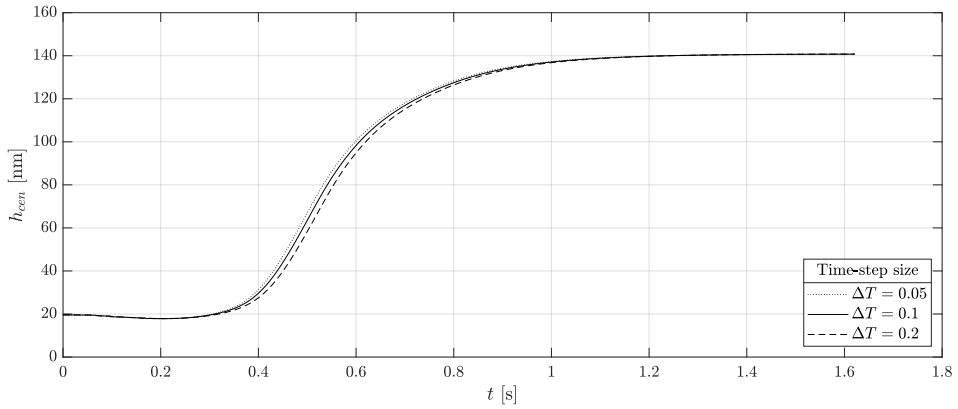


Figure C.1: *Transient central film thickness plots for simulations with varying time-step size, ΔT.*

Figure C.1 shows the effect of varying the time-step size, ΔT, on simulations using the parameters $a = 0.156, \hat{\eta} = 0.104$. It can be seen that increasing the time-step results in a shallower central film thickness increase but results in the same final film thickness of 140 nm. The difference in film height development is minimal, having a mean difference of 1.39% at each time-step location. Halving the time-step size results in even smaller changes in the central film thickness over time – with a mean difference of 0.99% – and the time-step $\Delta T = 0.1$ is confirmed to be adequately small.

C.2 Tolerance values

The height convergence and force balance criteria of Equations 2.6.2 and 2.7.2 were set such that a convergence tolerance of $\epsilon_{\text{tol,EHL}} = 10^{-3}$ was reached during the parameter search. To ensure that this is indeed sufficient, another simulation with $\epsilon_{\text{tol,EHL}} = 10^{-6}$ was also run. Figure C.2 shows that this increase in convergence stringency leads to only minimal differences in central film thickness over time.

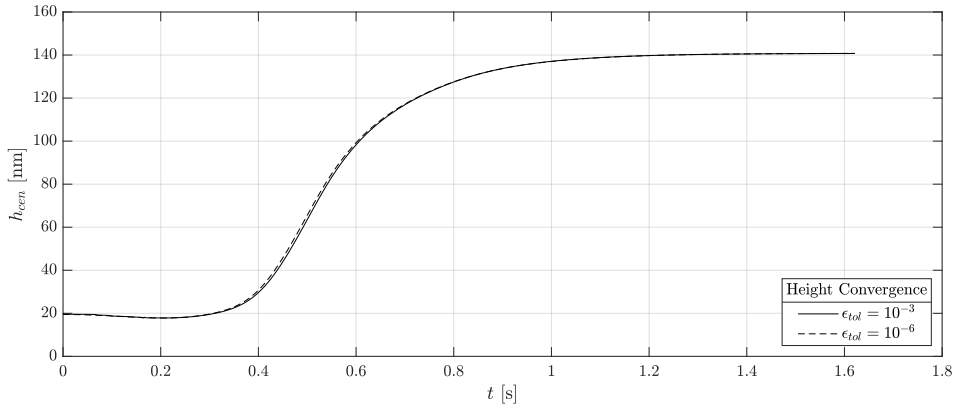


Figure C.2: *Transient central film thickness plots for simulations with varying height convergence tolerance,* ϵ_{tol}.

The convergence tolerance of the Reynolds equation super-solver can also be examined in the same manner. For the parameter search, a value of $\epsilon_{\text{tol,RESS}} = 10^{-4}$ was used and Figure C.3 shows that using a less stringent value of $\epsilon_{\text{tol,RESS}} = 10^{-3}$ led to no discernable difference in central film height over time.

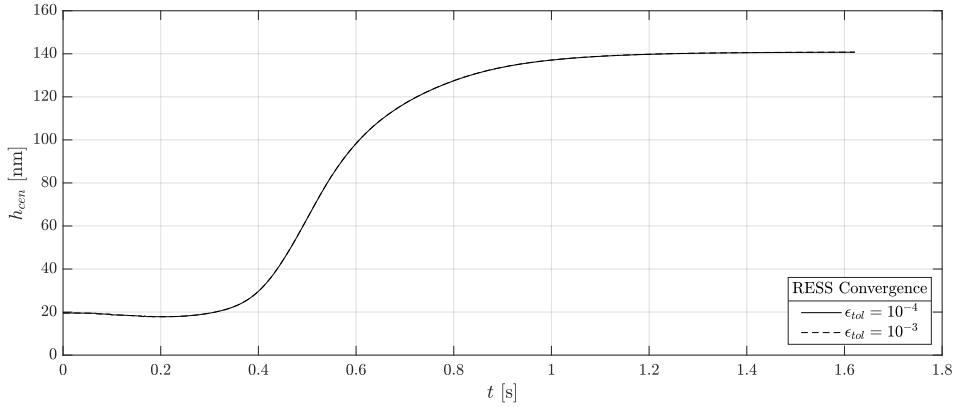


Figure C.3: *Transient central film thickness plots for simulations with varying Reynolds equation super-solver convergence tolerance,* ϵ_{tol}.

C.3 Mesh density

To allow the simulation to manage low values of the gradient parameter, a, in the parameter search, that cause protein matter to accumulate far upstream, the domain of the scalar transport equation was increased while retaining the same grid number, hence resulting in a coarser grid with larger ΔX and ΔY values. Once parameters were found that match the transient increase in film thickness over time of experiment, another simulation with the same increased transport domain of $-10 \leqslant X \leqslant 10, -10 \leqslant Y \leqslant 10$ but retaining the same grid density by increasing the grid number was run. A grid number of $N = 2^9$ results in the same ΔX and ΔY values as the EHL solver. The increase in mesh density incurred an extensive increase in computational cost and the simulation was terminated after one month, reaching 906 time-steps (0.73 s). The resulting comparison of central film height development can be seen in Figure C.4

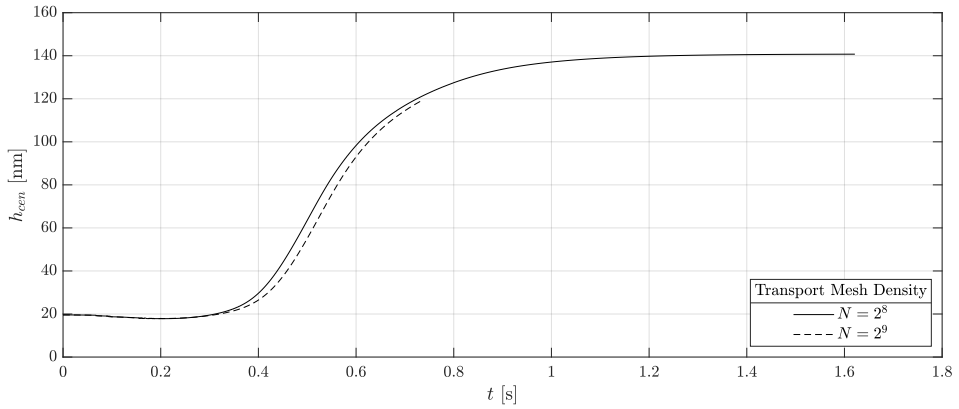


Figure C.4: *Transient central film thickness plots for simulations with varying mesh density number, N.*

Figure C.4 shows the central film height of the coarser and denser transport grids and it can be seen that small but non-negligible differences in central film height development are present. Figure C.5 shows a comparison of protein concentration development along the centre-line $Y = 0$ and it can be seen that the coarser grid simulation exhibits spurious oscillations in regions of high concentration gradient as was covered in § 3.5.2

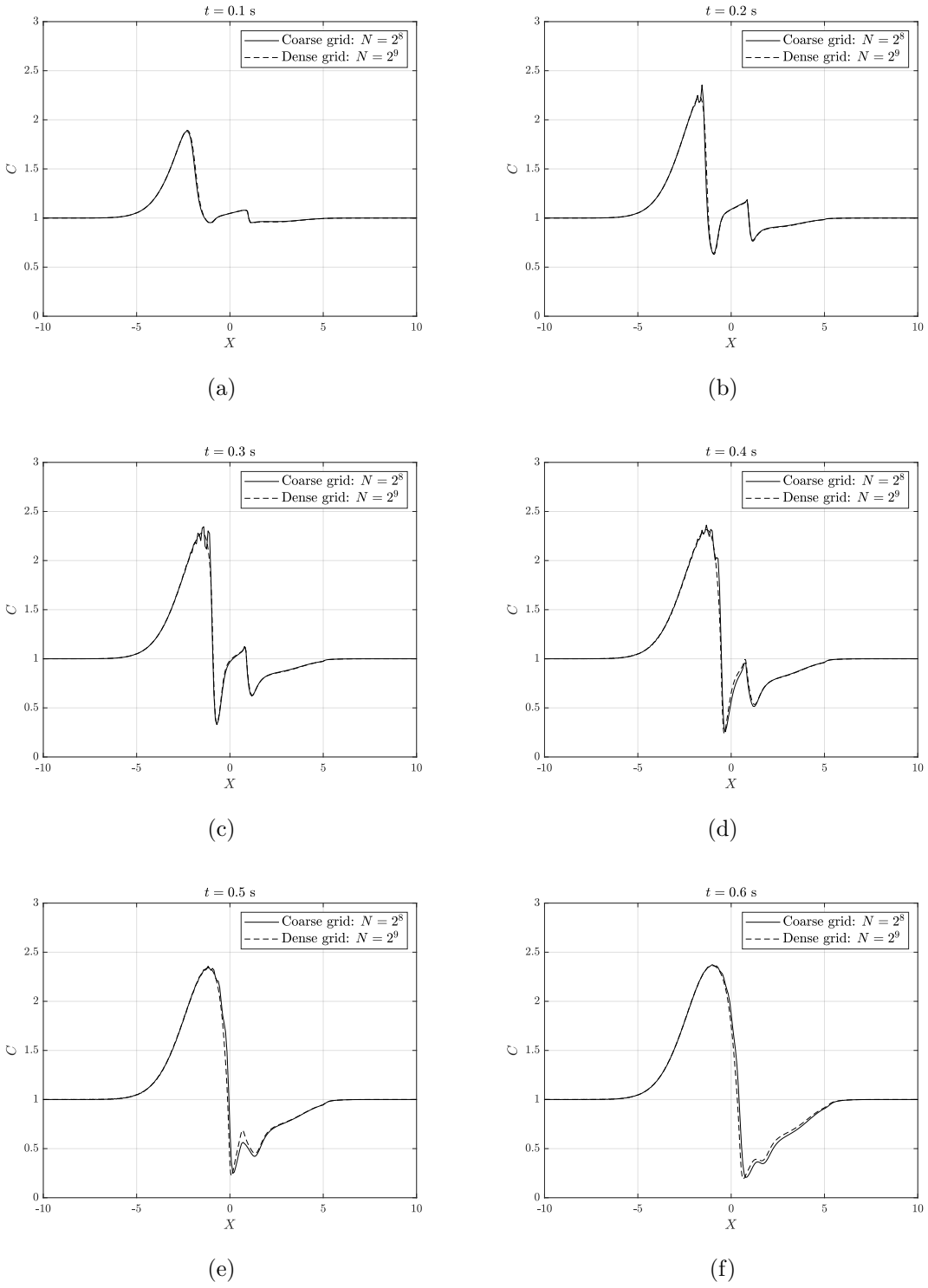


Figure C.5: *Comparison of protein concentration profile along* $Y = 0$ *for mesh number* $N = 2^8$ *and* 2^9*. The coarser mesh shows an onset of spurious oscillations in areas of high concentration gradient as is expected of central differencing schemes of insufficient grid density.*

To mitigate the development of spurious oscillations, a change in the mesh density and a change in the transport scheme were explored. It is possible to use a third order differencing scheme of the form

$$\frac{Q_x}{H}\frac{\partial C}{\partial X} \approx \left(\frac{Q_x}{H}\right)_{i,j} \frac{2C_{i+1,j} + 3C_{i,j} - 6C_{i-1,j} + C_{i-2,j}}{6\Delta X} \tag{C.3.1}$$

which introduces only one extra diagonal in the solution matrix at the upstream location, $i - 2$. The oscillations only occur in the x-direction and therefore the y-direction differencing can remain the same.

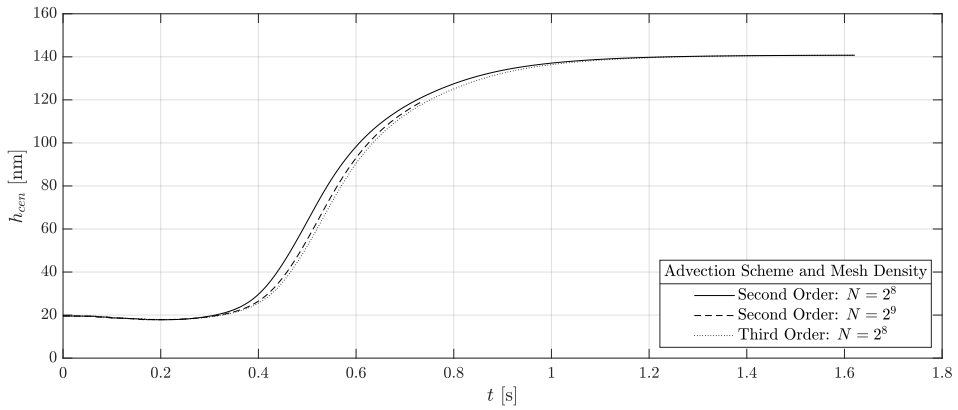


Figure C.6: *Transient central film thickness plots for simulations with varying mesh density number, N, and varying central differencing schemes for the x-direction advection term.*

Implementing this third order scheme does indeed bring the central film thickness development in line with the higher density grid for which the second order scheme had been used. The central film thickness plots can be found in Figure C.6, showing that a change in scheme can be used instead of an increase in grid density to achieve greater accuracy. Figure C.7 shows the protein concentration along $Y = 0$ for both the higher density grid of second order advection scheme alongside the lower density grid of third order advection scheme. These schemes are in agreement and the spurious oscillations do not occur.

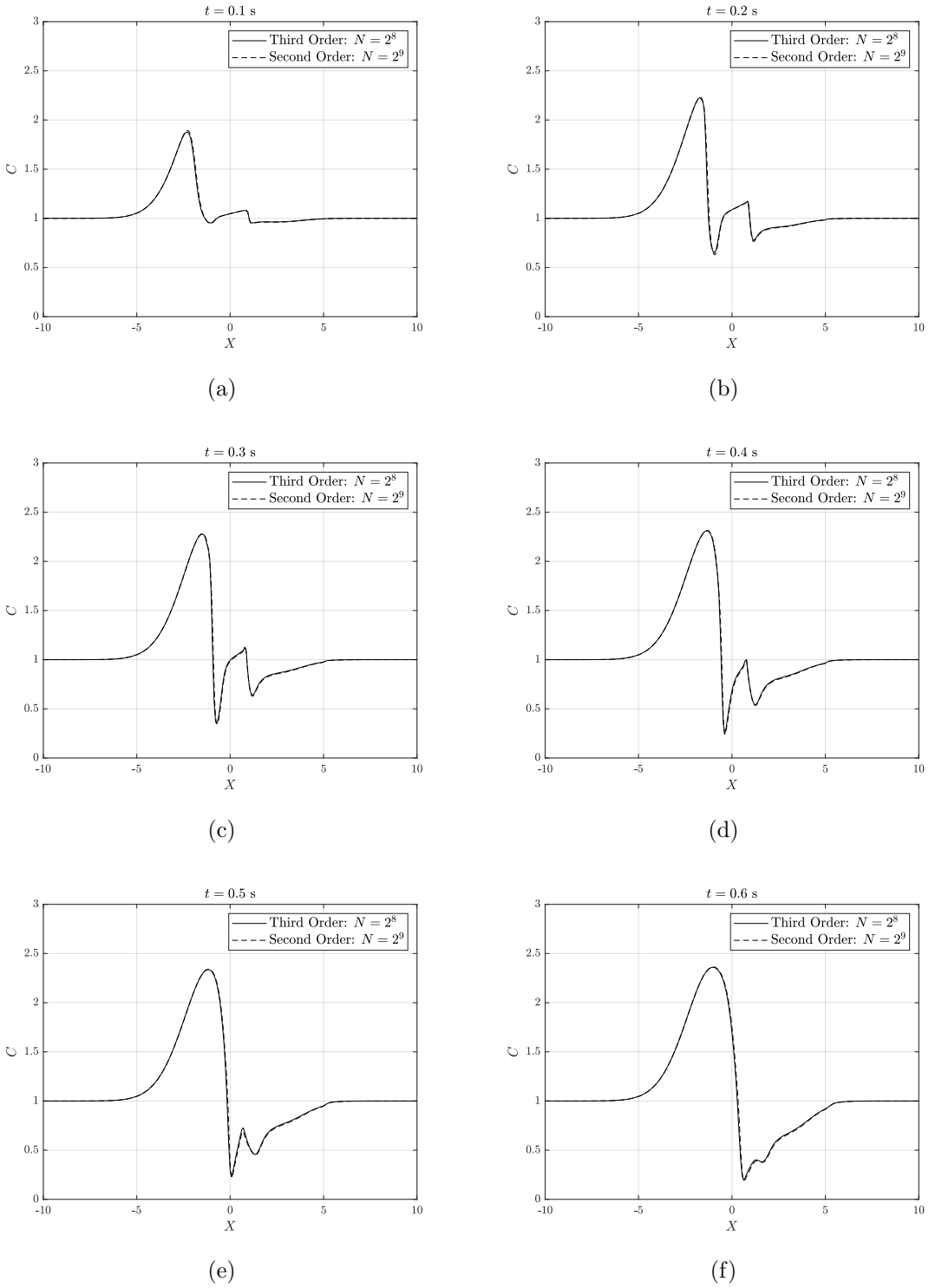


Figure C.7: *Comparison of protein concentration profile along* $Y = 0$ *for the third order advection scheme with a grid number* $N = 2^8$ *and the second order central scheme for a grid number* $N = 2^9$

It is also noted that the protein accumulation for those simulations in Figure C.7 occurs far enough downstream of the boundary at $X = -10$ that the need for a domain of this size may not be necessary for the operating parameters, $a = 0.156, \hat{\eta} = 0.104$. It is also noted that the protein concentration downstream of the cavitation line, which occurs no further downstream than $X = 2$, does not affect the results of the simulation with regards to pressure profile or height profile. It is therefore possible to maintain a dense scalar transport grid of a smaller size, but shifted upstream as in the examples of Chapter 4, using a domain such that $-8 \leqslant X \leqslant 2, -5 \leqslant Y \leqslant 5$. It has been shown that the EHL solver maintains accuracy on this shifted grid and this approach leads to the result that the grids for the EHL, RESS, and scalar transport solver are all the same, with no interpolation or extrapolation of grid-points necessary.

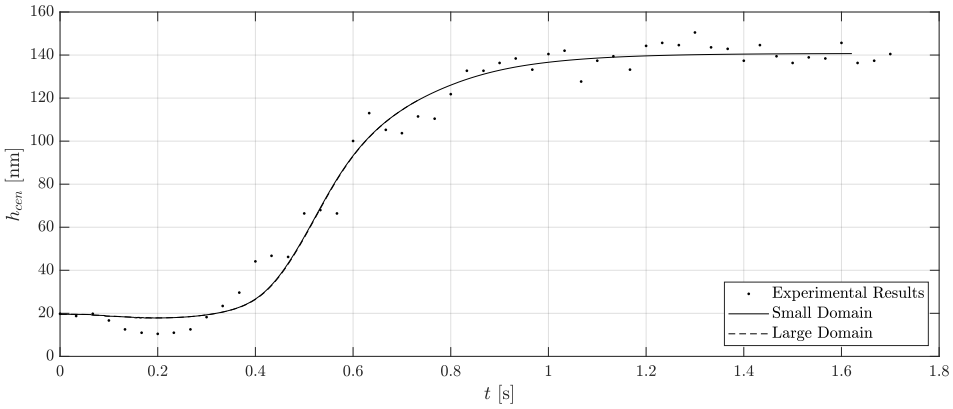


Figure C.8: *Transient central film thickness plots for simulations with varying domain size, the smaller domain is defined as* $-8 \leqslant X \leqslant 2, -5 \leqslant Y \leqslant 5$ *grid number* $N = 2^8$ *and the enlarged domain is defined as* $-10 \leqslant X \leqslant 10, -10 \leqslant Y \leqslant 10$ *for a grid number* $N = 2^9$*. The differing domain size results in the same mesh density with* $\Delta X = 0.0391$

Figures C.8 and C.9 show that the results of the small domain simulation are indistinguishable from those of the larger domain with the same mesh density indicating that for the values $a = 0.156, \hat{\eta} = 0.104$ the smaller domain is sufficient to capture the accumulation of protein content. There is no change in final film height with the transport grids of higher density, and the central film height development over time still matches experiments well.

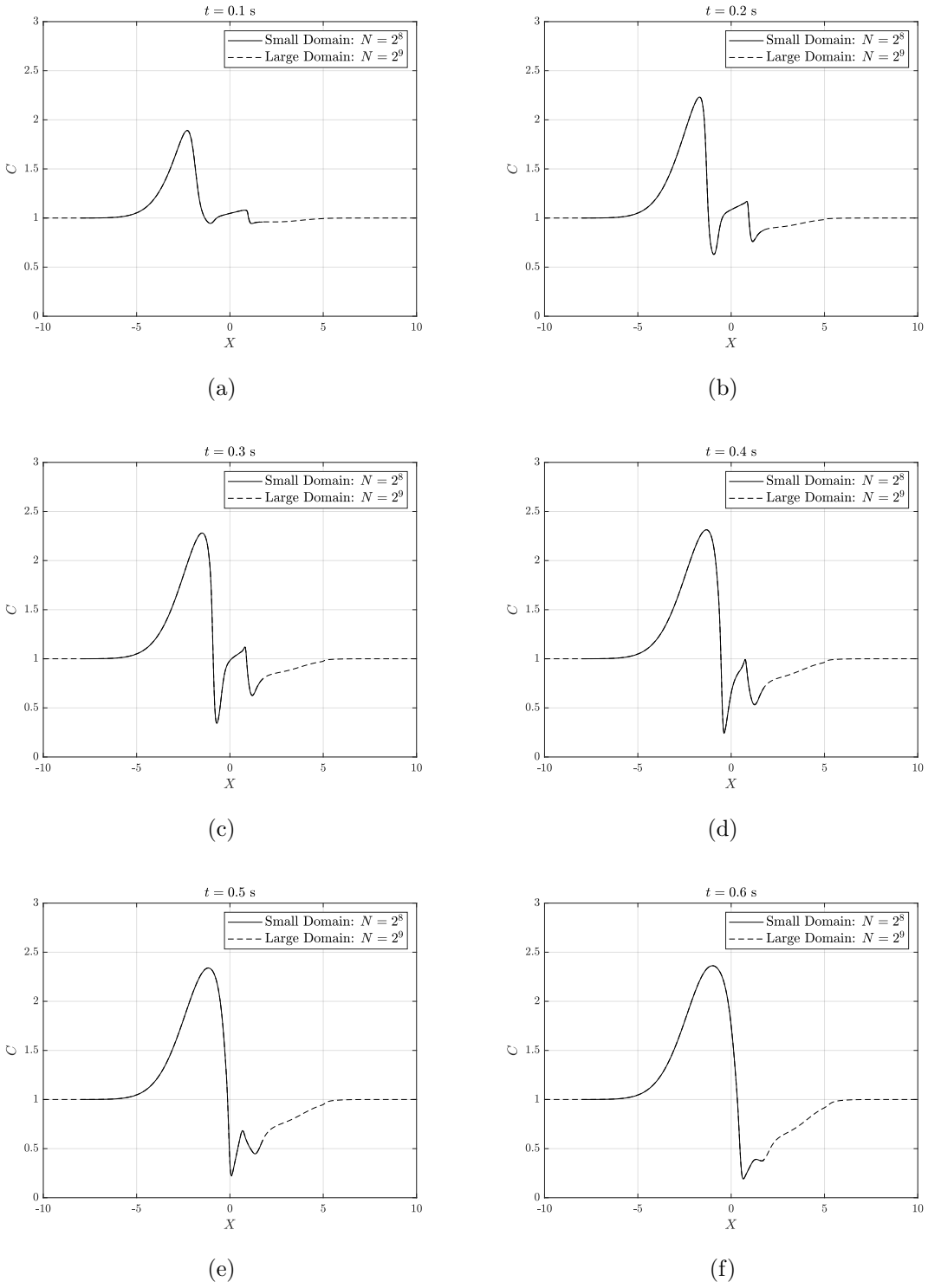


Figure C.9: *Comparison of protein concentration profile along* $Y = 0$ *for the small domain simulation whereby* $-8 \leqslant X \leqslant 2, -5 \leqslant Y \leqslant 5$ *grid number* $N = 2^8$ *and the enlarged domain whereby* $-10 \leqslant X \leqslant 10, -10 \leqslant Y \leqslant 10$ *for a grid number* $N = 2^9$.